

# **CARBON IN DEEP EARTH FROM HIGH-PRESSURE AND HIGH-TEMPERATURE STUDIES OF THE FE-C SYSTEM**

A DISSERTATION SUBMITTED TO THE GRADUATE DIVISION OF THE  
UNIVERSITY OF HAWAI'I AT MĀNOA IN PARTIAL FULFILLMENT OF  
THE REQUIREMENTS FOR THE DEGREE OF

**DOCTOR OF PHILOSOPHY**  
**IN**  
**GEOLOGY AND GEOPHYSICS**

May 2019

By  
**Xiaoqing Lai**

Dissertation Committee:

Bin Chen, Chairperson

Przemyslaw Dera

Julia E. Hammer

Jasper Konter

Michael J. Mottl

Copyright © 2019, Xiaojing Lai

*This dissertation is dedicated to my loving and supporting  
husband, Feng Zhu  
and parents, Xiaoli Tang, Xulong Lai*

# Acknowledgments

My thanks to my supervisor Dr. Bin Chen are endless. He supported and encouraged me through the past five years of my Ph.D. studies. He taught me that doing experiment is a painstaking task and every small step matters. He showed me how to be an independent researcher and how to write and publish my research by providing valuable insights and feedback.

I am also grateful to my committee members Dr. Przemyslaw Dera, Julia Hammer, Jasper Konter and Michael Mottl. Przemek also taught me a lot and helped me with the collection and analysis of the single-crystal X-ray diffraction data. Julia was the teacher of my mineralogy and theoretical petrology classes, I always enjoyed and learned a lot from her class. Jasper and Mike are also very helpful, their insights, comments and the questions raised in the every-semester dissertation committee meetings improve my dissertation a lot.

I am also thankful for my comprehensive committee members: Drs. Eric Hellebrand, Jeff Taylor, and Shiv Sharma; teachers: Drs. Clint Conrad, Gary Huss, Mike Garcia, Patricia Fryer and Scott Rowland etc.; collaborators: Drs. Jianwei Wang, Yoshio Kono, Feng Zhu, Murli H. Manghnani, Dongzhou Zhang, Eran Greenberg, Vitali Prakapenka, Jiachao Liu, Greg Finkelstein, Jing Gao, Yingxin Liu etc.; scientists I worked with in Advanced Phonon Source: Drs. Jiyong Zhao, Wenli Bi, E. Ercan Alp, Michael Y. Hu, Jing Yang, Jin Zhang, Jin Liu, Feng Shi, Sergey Tkachev etc.; labmates: John Balogh, Yihang Fang, Qingxia Wang, Siheng Wang, Zhiyuan Ren etc.; last but not the least, dear friends: Qian Zhang, Jiyoung Heo and Dr. Yi Hu, etc. Without their help, I cannot have this fulfilled Ph.D. journey.

I would also like to thank my family for their generous help and encouragement. My husband, Feng and I are not only fantastic partners in the journey of lives but also good cooperators in our researches. He helped me a lot even we were 4000 miles away from each other for a long time.

Thank you all for enriching my Ph.D. studies and my life!

# Abstract

Carbon in deep Earth, as well as the nature and extent of deep carbon cycles, is essential for understanding the physical and chemical evolution of habitable planets. This dissertation includes three projects to address carbon in the Earth's deep interior from the perspectives of high-pressure mineral physics.

The first project (Chapter 3) comprises experimental and computational results on the structural evolution of iron-nickel liquids alloyed with carbon at high pressures. Our X-ray diffraction experiments up to 7.3 gigapascals (GPa) demonstrate that  $\text{Fe}_{90}\text{Ni}_{10}$  liquids alloyed with 3 and 5 wt.% carbon undergo a polyamorphic liquid structure transition at approximately 5 GPa. Corroborating the experimental observations, our first-principles molecular dynamic calculations reveal that the structural transitions result from the marked prevalence of three-atom face-sharing polyhedral connections in the liquids at  $>5$  GPa. The structure and polyamorphic transitions of liquid iron-nickel-carbon alloys govern their physical and chemical properties and may thus cast fresh light on the chemical evolution of terrestrial planets and moons.

The second project (Chapter 4) concerns the high-pressure thermoelastic properties of one of the Earth's inner core candidates, iron carbide,  $\text{Fe}_7\text{C}_3$ . In this study, we performed synchrotron-based single-crystal X-ray diffraction experiments using an externally-heated diamond anvil cell to determine the crystal structure and thermoelastic properties of  $\text{Fe}_7\text{C}_3$  up to 80 GPa and 800K. Our diffraction data indicate that  $\text{Fe}_7\text{C}_3$  adopts an orthorhombic structure under the experimentally investigated conditions. The pressure-volume-temperature relations of  $\text{Fe}_7\text{C}_3$  were obtained by fitting the high-temperature Birch-Murnaghan equation of state. We also observed an anisotropic elastic response to changes in pressure and temperature along the different crystallographic directions.  $\text{Fe}_7\text{C}_3$  has strong anisotropic compressibilities with the linear moduli  $M_a > M_c > M_b$  from zero pressure to core pressures at 300K, revealing the  $b$  axis to be the most compressible. The thermal expansion of  $c^3$  is approximately four times larger than that of  $a^3$  and  $b^3$  at 600K and 700K, implying that high temperature may significantly influence the elastic anisotropy of  $\text{Fe}_7\text{C}_3$ . Therefore, the effect of high temperature needs to be considered when using  $\text{Fe}_7\text{C}_3$  to explain the anisotropy of the Earth's inner core.

The third project (Chapter 5) examines the high-pressure phase stability and melting behavior of the Fe-C-(H) system by both multi-anvil press and diamond anvil cell experiments. Metallic iron reacted with an organic C-H compound, which served as carbon and hydrogen

source, under conditions of high pressure and temperature. With excess C-H compound, Fe carbide and molecular hydrogen formed first from the reaction at high pressures and relatively low temperature. With increasing temperature, Fe hydride and diamond were found to form. With excess Fe, by contrast, the presence of hydrogen depressed the melting temperature of the Fe-C system, such that the eutectic melting temperatures for both the Fe-C and Fe-C-H systems are below the mantle geotherm. Those Fe-rich melts may facilitate the cycling of subducted carbon and hydrogen in the deep mantle. These melts may provide a necessary melt environment for the growth of macro diamonds in deep mantle; they could also serve as a potential reservoir for both carbon and hydrogen in the mantle.

# Table of Contents

Acknowledgments.....	iv
Abstract.....	v
Table of Contents.....	vii
List of Tables.....	ix
List of Figures.....	x
Chapter 1 Introduction.....	1
1.1 Carbon in deep Earth.....	1
1.2 Earth’s core.....	2
1.3 Carbon and other light elements in the Earth’s core.....	6
1.4 Subducted and mantle carbon.....	7
1.5 Scope of this dissertation.....	8
Chapter 2 Methodology.....	9
2.1 High-pressure devices.....	9
2.1.1 Diamond anvil cell.....	10
2.1.2 Large volume press.....	13
2.2 X-ray diffraction.....	18
2.3 Theoretical calculations.....	20
Chapter 3 Liquid Structure of Fe-Ni-C System: Implications for Planetary Chemical Evolutions.....	22
3.1 Abstract.....	22
3.2 Introduction.....	23
3.3 Materials and methods.....	25
3.3.1 High-pressure experiments.....	25
3.3.2 Theoretical calculations.....	29
3.4 Results.....	29
3.4.1 Structure measurements for Fe-Ni-C liquids.....	29
3.4.2 Molecular dynamics calculations for Fe-Ni-C liquids.....	35
3.5 Discussion and geophysical implications.....	43
3.6 Conclusions.....	44
3.7 Acknowledgments.....	45

Chapter 4 Thermoelastic Properties of Fe <sub>7</sub> C <sub>3</sub> at High Pressures by Single-Crystal X-Ray Diffraction.....	47
4.1 Abstract .....	47
4.2 Introduction .....	48
4.3 Methods.....	50
4.4 Results and discussion.....	52
4.4.1 The crystal structure of Fe <sub>7</sub> C <sub>3</sub> at room pressure and temperature .....	52
4.4.2 Thermal equation of state of Fe <sub>7</sub> C <sub>3</sub> .....	54
4.4.3 Compressibilities and thermal expansions of the <i>a</i> , <i>b</i> and <i>c</i> axes.....	62
4.5 Geophysical implications for the Earth's inner core.....	69
4.6 Acknowledgments.....	69
Chapter 5 High-pressure Melting in the Fe-C-(H) System with Implications for the Fate of Subducted Carbon.....	71
5.1 Abstract .....	71
5.2 Introduction .....	72
5.3 Methods.....	73
5.3.1 Multi-anvil press experiment.....	73
5.3.2 Laser-heated DAC experiment.....	74
5.4 Results and discussion.....	75
5.4.1 Multi-anvil press experiment.....	75
5.4.2 Laser heating experiment.....	80
5.4.3 Melting temperature of the Fe-C-(H) system by LVP and DAC .....	90
5.5 Implications.....	93
5.6 Acknowledgments.....	95
Chapter 6 Conclusions and Future Work.....	97
References.....	99

# List of Tables

Table 3.1. Peak positions for the integrated 1st and 2nd atomic shells. ....	28
Table 4.1. Lattice parameters of $\text{Fe}_7\text{C}_3$ obtained by high-pressure and high-temperature single crystal X-ray Diffraction. ....	57
Table 4.2. Thermoelastic properties of $\text{Fe}_7\text{C}_3$ compared with previous studies. ....	60
Table 5.1. Experimental conditions and run products in multi-anvil press melting experiments for the Fe-C system. ....	75
Table 5.2. Experimental conditions and run products in multi-anvil press melting experiments for the Fe-C-H system .....	76
Table 5.3. Melting points of $\text{Fe}_3\text{C}$ and the eutectic melting points in the Fe-C-H system .....	89

# List of Figures

Figure 1.1. Cartoon illustrating deep carbon cycles through Earth's history. Figure modified after (Dasgupta, 2013; Rubie et al., 2007) .....	2
Figure 1.2. Compressional velocity ( $v_p$ ), shear velocity ( $v_s$ ) and density of AK135 model and Fe. ....	3
Figure 1.3. Layered structure of Earth .....	4
Figure 2.1. Schematics of the core components of a diamond anvil cell.....	10
Figure 2.2. BX90 diamond anvil cell.....	11
Figure 2.3. Externally-heated BX90 diamond anvil cell with its components .....	12
Figure 2.4. Symmetric diamond anvil cell and the sample chamber during the laser heating .....	13
Figure 2.5. Experimental set-up of the Paris-Edinburgh Press at 16 BMB, Advanced Photon Source. ....	15
Figure 2.6. Illustration of the cell assembly for liquid structure measurements.....	15
Figure 2.7. Multi-anvil press and multi-anvil assembly. ....	17
Figure 2.8. Schematics of 14/8 and 10/5 standard COMPRES assembly .....	17
Figure 2.9. Illustration of Bragg's law.....	18
Figure 2.10. Set-up of high-pressure and high-temperature single-crystal X-ray diffraction at beamline 13-BMC, Advanced Photon Source. ....	19
Figure 3.1. Cross-section of the cell assembly for liquid structure measurements in a Paris-Edinburgh press, modified after (Kono et al., 2014). ....	26
Figure 3.2. EDXD patterns before and after melting the sample ( $\text{Fe}_{90}\text{Ni}_{10}$ )-5wt.%C collected at $15^\circ$ . ....	27
Figure 3.3. Representative experimental data and total structure factor $S(q)$ of $\text{Fe}_{90}\text{Ni}_{10}$ -5wt.% C liquid at 1.5 GPa and 1523 K.....	30
Figure 3.4. Total structure factor $S(q)$ and reduced pair distribution function $G(r)$ of $\text{Fe}_{90}\text{Ni}_{10}$ -5wt.%C liquids at high pressure and temperature. ....	31
Figure 3.5. Representative total structure factor $S(q)$ and reduced pair distribution function $G(r)$ of $\text{Fe}_{90}\text{Ni}_{10}$ -5wt.% C and $\text{Fe}_{90}\text{Ni}_{10}$ -3wt.% C liquids at high pressure and temperature. ....	32
Figure 3.6. Pressure dependence of the main $S(q)$ peak of Fe-Ni-C liquids.....	33
Figure 3.7. Pressure dependence of peak positions for the 1st and 2nd nearest-neighbor shells (NNs) from reduced pair distribution functions $G(r)$ of $\text{Fe}_{90}\text{Ni}_{10}$ -5wt.% C and $\text{Fe}_{90}\text{Ni}_{10}$ -3wt.% C liquids in this study compared with iron/iron alloy liquids in previous work.....	34
Figure 3.8. Computational total and partial RDFs of $\text{Fe}_{91}\text{Ni}_9$ -5wt.% C liquid and experimental results of $\text{Fe}_{90}\text{Ni}_{10}$ -5wt.% C at similar $P$ - $T$ conditions were also appended for comparison.....	36
Figure 3.9. Total RDFs and decomposed RDF for the second coordination connection schemes at (a) 1.3 GPa, 1673 K and (b) at 8.4 GPa, 1673 K. (c) Inset: snapshot of MD simulations with the computational super cell highlighted in dashed lines. ....	38
Figure 3.10. Representative experimentally-determined $G(r)$ for $\text{FeNi}_3\text{C}$ liquid at 3.4 GPa and 7.3 GPa and fitting results of the first and second NNs peaks.....	39

Figure 3.11. Peak positions $r_{2s}$ and $r_{2m}$ as a function of $r_1$ . Dashed lines represent the ideal positions for 1-atom, 2-atom, 3-atom and 4-atom motif connections.....	41
Figure 3.12. Structure information of Fe <sub>91</sub> Ni <sub>9</sub> -5wt.% C liquid and Fe <sub>3</sub> C from first-principle molecular dynamics simulations. (a) Snapshot of MD simulations with the computational super cell highlighted in dashed lines. (b) Carbon coordination environment of crystalline Fe <sub>3</sub> C. (c) Carbon coordination environment of Fe <sub>91</sub> Ni <sub>9</sub> -5wt.% C liquid at 5.1 GPa, 1673 K.....	42
Figure 4.1. $P$ - $T$ coverage of the XRD experiments of Fe <sub>7</sub> C <sub>3</sub> in the diamond anvil cell. ....	51
Figure 4.2. All the peaks harvested from single-crystal XRD measurements of Fe <sub>7</sub> C <sub>3</sub> at the University of Hawai‘i at Mānoa .....	53
Figure 4.3. Crystal structure of Fe <sub>7</sub> C <sub>3</sub> projected along the $b$ axis (left), the $a$ axis (upper right) and the $c$ axis (lower right) at ambient conditions (space group $Pbca$ , $Z = 8$ ) .....	53
Figure 4.4. Representative single-crystal XRD image at 28.8 GPa and 700 K(left) and projections of the Fe <sub>7</sub> C <sub>3</sub> crystal structure in reciprocal space along different crystallographic directions (right). ....	55
Figure 4.5. Density of the orthorhombic Fe <sub>7</sub> C <sub>3</sub> at 300K in this study compared with other studies. Inset is the $F$ - $f$ plot of data in this study.....	56
Figure 4.6. $P$ - $V$ - $T$ data of Fe <sub>7</sub> C <sub>3</sub> fitted by the high-temperature Birch-Murnaghan Equation of State.....	62
Figure 4.7. Compressibilities of the $a$ , $b$ and $c$ axes of Fe <sub>7</sub> C <sub>3</sub> as a function of pressure. ....	63
Figure 4.8. High-temperature normalized axial lengths of Fe <sub>7</sub> C <sub>3</sub> versus pressure .....	65
Figure 4.9. Thermal expansion of $a^3$ , $b^3$ and $c^3$ axes of Fe <sub>7</sub> C <sub>3</sub> at 600K and 700K. ....	66
Figure 4.10. Axial ratios of Fe <sub>7</sub> C <sub>3</sub> up to 800K as a function of pressure.....	67
Figure 5.1. Representative backscattered electron images of quenched texture of the run products. ....	77
Figure 5.2. Summary of the experimental runs of (a) the Fe-C system and (b) the Fe-C-H system. ....	78
Figure 5.3. Melting temperatures of Fe-C and Fe-C-H determined by large volume press experiments compared with melting temperatures of Fe-C, Fe-H in previous large volume press studies. ....	79
Figure 5.4. Reactions of Fe and C <sub>14</sub> H <sub>12</sub> (a) up to 1300 K at 10.7 GPa in run-1 and (b) up to 1672 K at 21.4 GPa in run-2 .....	82
Figure 5.5. Reaction between iron hydride and C <sub>14</sub> H <sub>12</sub> in run-1 .....	83
Figure 5.6. Reaction of Fe and C <sub>14</sub> H <sub>12</sub> up to 1880 K at 42.6 GPa in run-2 .....	83
Figure 5.7. Third sample loading configuration used for the Fe-C-H melting experiment .....	85
Figure 5.8. XRD patterns of hcp Fe-C before and after diffusion of hydrogen in run-4 at 13-IDD. Inset shows the volume expansion of Fe-C after gradual diffusion of hydrogen. Fe-C-H <sub>x</sub> were formed after adding hydrogen to the crystal structure. ....	85
Figure 5.9. Series of representative integrated X-ray diffraction patterns at HPHT showing the evolution of melting.....	86
Figure 5.10 Representative XRD patterns of the quenched product after the melting of a) Fe-C-H system in run-3. b) Fe <sub>3</sub> C in run-3. c) Fe-C-H in run-4.....	87

Figure 5.11 Original data for melting temperatures of Fe-C, Fe-C-H and Fe<sub>3</sub>C in this study compared with the melting temperature of Fe-C, Fe-H and Fe<sub>3</sub>C in previous studies. Mantle geotherm and cold slab surface temperature are also plotted for comparison ..... 91

Figure 5.12. Corrected data for melting temperatures of Fe-C, Fe-C-H and Fe<sub>3</sub>C in this study compared with the melting temperature of Fe-C, Fe-H and Fe<sub>3</sub>C in previous studies. Mantle geotherm and cold slab surface temperature are also plotted for comparison..... 92

Figure 5.13. Melting curves of Fe-C, Fe-C-H and Fe<sub>3</sub>C in this study compared with mantle geotherm and cold slab surface temperature. The upper mantle, transition zone and lower mantle are separated by the grey dashed lines..... 93

Figure 5.14. Cartoon illustrating the proposed reaction and melting under mantle conditions... 95

# Chapter 1

## Introduction

### 1.1 Carbon in deep Earth

Carbon (C), the fourth most abundant element in the Universe, plays an essential role in the sustainability of life on Earth. Carbon is not only one of the primary building blocks of all organic matter on Earth, it also exists in the atmosphere, hydrosphere and in many rocks such as limestone. Because the near-surface carbon cycle profoundly affects Earth's climate and ecosystems, it has been the subject of numerous studies from various disciplines. By contrast, relatively little is known about deep carbon in the Earth's mantle and core, including its abundance, reservoirs and occurrences. The mechanism of deep carbon cycling between Earth's surface and interior remain controversial. Fundamental research to understand carbon in deep Earth focuses on the physical and chemical behavior of carbon-bearing phases at relevant high-pressure and high-temperature conditions.

Figure 1.1 shows a model of deep carbon cycles through Earth's history, from proto-Earth to modern Earth. Earth is considered to possess a magma ocean during the earliest stage when the temperature was high and iron (Fe) and part of silicates were molten (Rubie et al., 2007). There would have been an exchange of C between the magma ocean and the atmosphere (Dasgupta, 2013). At the same time, when the high-density Fe melt was segregated from the silicate melt and sank to the center of Earth, carbon as an iron-loving element could have been dissolved into Fe and sequestered into the core by liquid Fe (Dasgupta, 2013). The mechanism of metal and silicate segregation will be discussed in section 1.2 (Rubie et al., 2007). The segregated Fe with dissolved carbon and other Fe-loving elements formed Earth's primordial core. Due to the secular cooling of Earth, the solid silicate mantle formed, and the solid inner core crystallized from the liquid outer core. The concentration of carbon in the outer core and inner core highly depend on the amount of C dissolved into the core during the core formation process. Between the surface and mantle, subduction slab brought carbon down into the mantle, whereas volcanism brought carbon back to the surface (Figure 1.1).

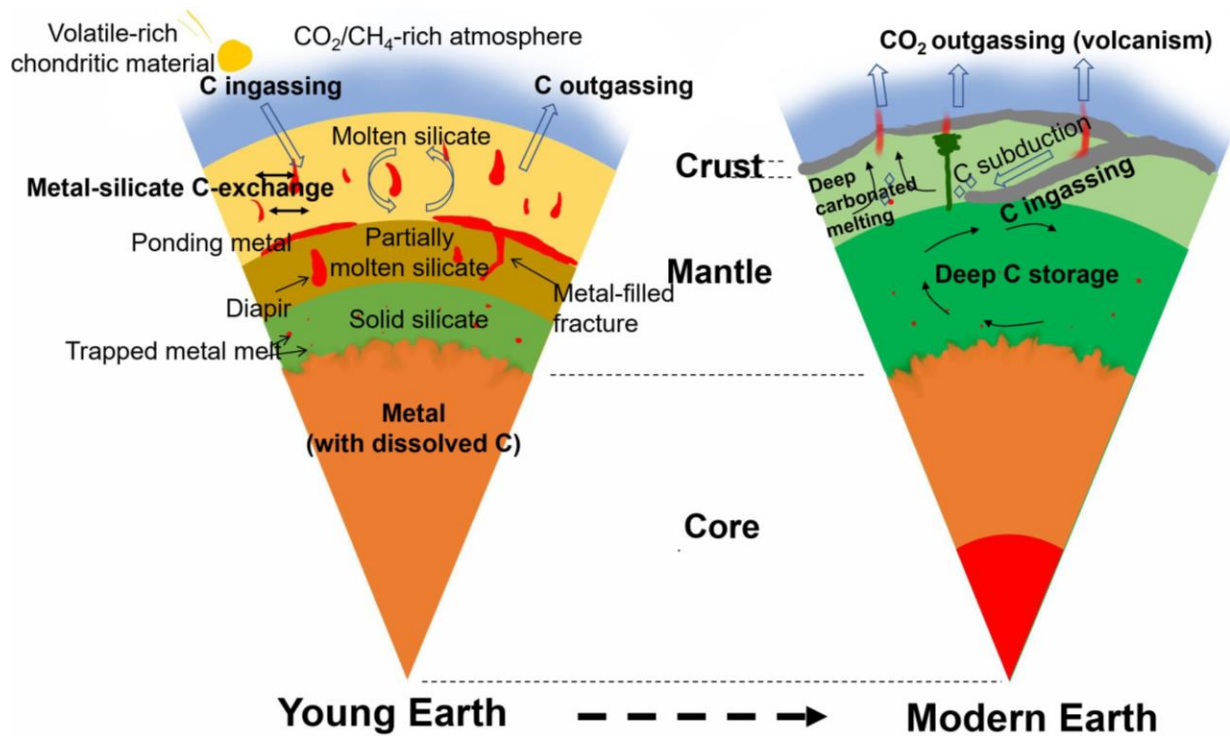


Figure 1.1. Cartoon illustrating deep carbon cycles through Earth's history. Figure modified after (Dasgupta, 2013; Rubie et al., 2007).

## 1.2 Earth's core

Earth's core and the cores of other planets and moons can be investigated directly by geophysical observations (such as seismology and geomagnetism) and in most cases indirectly by geochemistry, cosmochemistry and mineral physics. The Earth's core occupies approximately 1/6 of the whole Earth by volume and 1/3 by mass. At the core mantle boundary (CMB) (2891 km), where the pressure reaches 136 GPa, the density has a large jump from silicate mantle to metallic core. The compressional wave velocity decreases at this boundary and the shear waves virtually disappear, only to reappear at inner core boundary (ICB) at 5150 km and 329 GPa (Figure 1.2). These observations indicate that Earth has an outer core (OC) that is a liquid and an inner core (IC) that is solid (Figure 1.2 and Figure 1.3). The pressure in the Earth's outer core is 136-329 GPa and the pressure in the inner core is 329-364 GPa, based on geophysical observations. The schematic layered structure is presented in Figure 1.3. The temperature of the core is less well constrained; it is estimated to be in the range of 3850 K- 4600 K at the CMB and 5150 K-6200 K at the ICB (Fischer, 2016).

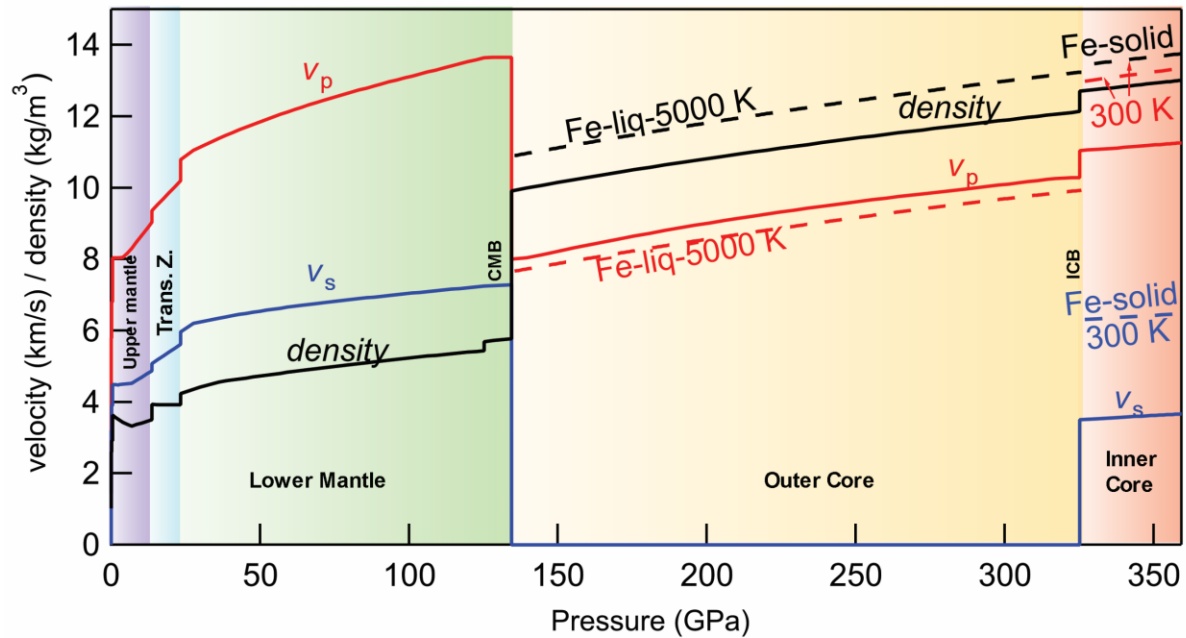


Figure 1.2. Compressional velocity ( $v_p$ ), shear velocity ( $v_s$ ) and density of AK135 model (solid lines) (Kennett et al., 1995) and  $v_p$ ,  $v_s$  and density of Fe (dashed lines) as a function of pressure.  $v_p$  is presented in red,  $v_s$  is presented in blue and density is presented in black. The sound velocities of liquid Fe at 5000 K are plotted (Anderson and Ahrens, 1994). The density (Mao et al., 1990) and sound velocities of solid Fe at 300 K are plotted without temperature effect (Mao et al., 2001).

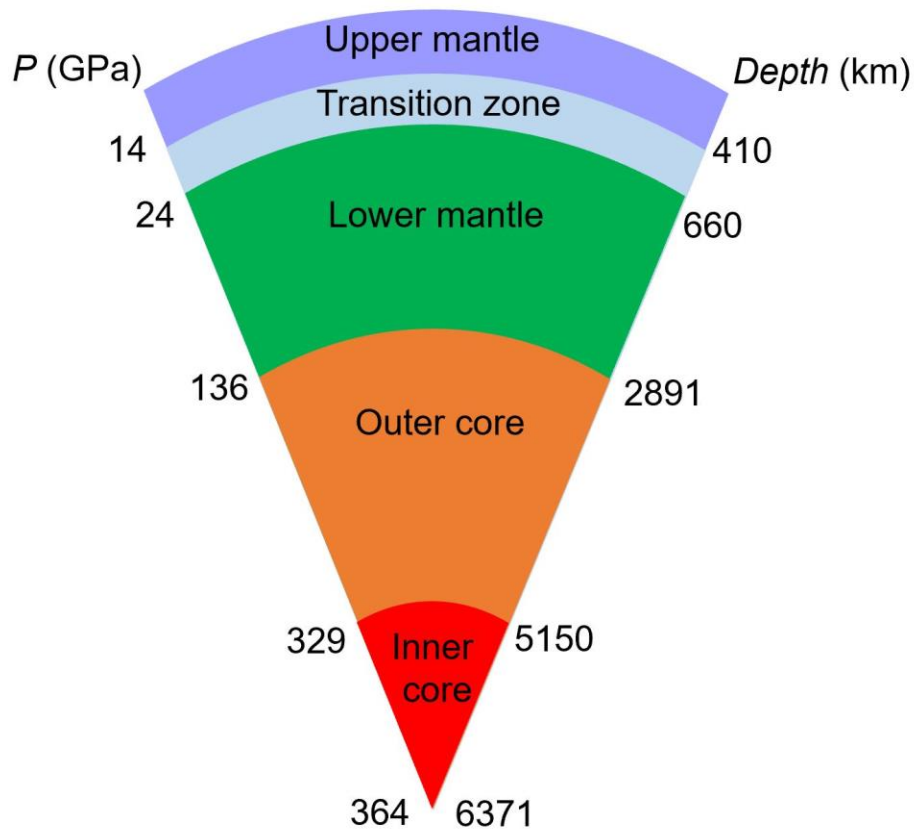


Figure 1.3. Layered structure of Earth. The pressures and depths of the boundaries are according to the PREM model (Dziewonski and Anderson, 1981).

Core formation by metal-silicate segregation is thought to have occurred within 30Myr of the initiation of the solar system formation, as implied by the hafnium-tungsten (Hf-W) isotopic geochronometer (reviewed by Rubie et al. (2007)). Three possible segregation mechanisms have been proposed: 1) Rapid and efficient metal-silicate separation in a global magma ocean, 2) dyking or diapirism, and 3) percolation of liquid metal through a matrix of polycrystalline silicates (Figure 1.1) (reviewed by Rubie et al. (2007)).

As Earth cooled down, iron alloy solidified from the Earth's liquid core, separating the core into two parts: the liquid outer core and the solid inner core. The liquid outer core may be compositionally uniform with a ~5-10% density deficit with regard to iron (Hirose et al., 2013; Litasov and Shatskiy, 2016). Shear waves cannot be transmitted through the liquid outer core. It is generally accepted that the Earth's magnetic field is generated by convection of liquid metal within the outer core. The generation of the magnetic field requires this metal to be a good

conductor; this and evidence from meteorites and galactic elemental abundances strongly suggest that Fe should be the predominant element in the core (Stevenson, 2003).

The solid inner core has a ~5% density deficit compared with Fe (Litasov and Shatskiy, 2016). It may repulse some light elements to the outer core, which contributes to convection of the outer core. The inner core is found to be elastically anisotropic. Seismic waves travel faster along the polar axis than through the equatorial directions (Deuss, 2014 and papers within). This anisotropy is believed to be due to preferred orientation of crystalline Fe or Fe alloys. A review paper by Deuss (2014) summarizes the mechanisms hypothesized for preferred orientation of crystals in the inner core, which involve solidification and deformation, but no consensus has yet emerged on the general causes.

The Earth's core is widely accepted to consist primarily of iron alloyed with ~5-8 % Nickel (Ni). Iron is a cosmochemically abundant element in the universe and the sound velocity and density of Fe at core conditions is close to those inferred from seismic data (Mao et al., 1990; Mao et al., 2001). Additionally, iron meteorites are considered to be fragments of planetary cores. The presence of Ni is inferred from its similarity and high affinity to Fe and the prevalence of Fe-Ni alloys in iron meteorites.

The presence of light elements in the core is considered to account for the density deficit and sound velocity discrepancies between Fe-Ni alloy and seismic models of Earth such as the Preliminary Reference Earth Model (PREM) and AK135 model (Birch, 1952, 1964; Dziewonski and Anderson, 1981; Kennett et al., 1995; Li and Fei, 2014; Poirier, 1994) (Figure 1.2). A considerable concentration of light elements such as S, Si, O, C, H is required in the Earth's core to account for these discrepancies (reviewed by Li and Fei (2014)). The identity and abundance of these light elements, however, remain controversial. Similar to Earth, a number of terrestrial planets and moons likely possess partially or fully molten cores that are composed of Fe-rich alloys, i.e., Mercury, Venus, Mars, Moon, Ganymede, Io and Europa. Lacking of geophysical measurements, the core compositions of these planets and moons are even less constrained (Chen et al., 2008; Dasgupta et al., 2009; Hauck et al., 2013; Weber et al., 2011).

Our understanding of the structure, dynamics, and chemical evolution of the cores of Earth, and other planets and moons hinges on the physical properties of liquid and crystalline Fe alloyed with light elements. The incorporation of light elements into Fe alloys can explain the density deficit of the Earth's core and the sound velocity differences from seismic observation.

The melting temperature of core materials (Fe-Ni alloyed with light elements) at the inner core boundary at 329 GPa serves as an anchor point for the thermal profile of the Earth's core. The exsolution of light elements to the outer core during solidification of inner core is considered as a driving force of the geodynamo which generates Earth's magnetic field. With the development of state-of-art techniques in seismology and mineral physics, we can achieve a better understanding of the Earth's core.

### **1.3 Carbon and other light elements in the Earth's core**

Carbon has a high solubility in both solid and liquid Fe as well as a high cosmic abundance, which makes it one of the leading candidates of light elements in Earth's core (Wood, 1993). In addition, iron carbides such as cohenite are commonly found in Fe meteorites (Wasson, 2012). Based on a comparison between carbon abundance in the Earth's mantle with chondritic meteorites, the core may host ~90% of Earth's carbon budget (McDonough, 2003). The concentration of carbon in the Earth's core is still under debate. By analogy with chondrites it would be about 0.2 wt.% (McDonough, 2003), whereas it is estimated to be 2-4 wt.% from the perspective of mineral physics, which shows that carbon is highly soluble in Fe liquid at high pressures and temperatures of the planetary accretion and differentiation (Wood, 1993). In the outer core, carbon can occupy the interstitial sites in Fe liquid at carbon concentrations less than 3 wt.% C. At higher concentrations there are regions of Fe<sub>3</sub>C-like structure (a deformed hcp-Fe lattice) in the liquid (Sobolev and Mirzoev, 2013). For the inner core, Fe<sub>3</sub>C was considered to be a inner core candidate (Gao et al., 2008; Wood, 1993). Recent studies, however, suggest that Fe<sub>7</sub>C<sub>3</sub> instead of Fe<sub>3</sub>C would be preferred since it is the first phase solidified from Fe-C melts at core conditions according to the phase diagram of Fe-C at core conditions (Fei and Brosh, 2014).

There are also some other light element candidates. Hydrogen is one because of its extremely high cosmic abundance, high solubility in Fe at pressures higher than 3.5 GPa (Badding et al., 1991) and high partition coefficient between Fe and silicate melts (Okuchi, 1997). It is however challenging to investigate the Fe-H system (FeH<sub>x</sub>) as H is an invisible element to most probing methods and Fe hydrides cannot be preserved at ambient conditions for analysis. Sulfur is another candidate for light element in the core because Fe sulfide is common in meteorite (Wasson, 2012). Sulfur can be barely soluble in Fe at atmospheric pressure but can form Fe sulfides under atmospheric pressure (Kubaschewski, 2013). Its solubility reaches 8 at%

or 4.8 wt.% at 120 GPa, 2600K (Kamada et al., 2012), probably because the atomic radius of S is similar to that of Fe at high pressures, so that S can substitute Fe in the crystal structure (Alfè et al., 2002). Phosphorus is probably present in the core because Fe-P alloy is found in meteorites and the abundance of P in Earth's mantle rocks deviates greatly from the planetary volatility trend (McDonough, 2003; Wasson, 2012). Oxygen and Silicon are also considered as light element candidates because of their high cosmic abundance and high solubility in Fe at high pressure and temperature (Hirose et al., 2013). Previous studies of the melting behavior and phase relations in the binary systems of Fe alloyed with one of the candidate light elements have been reviewed (Hirose et al., 2013; Litasov and Shatskiy, 2016).

## 1.4 Subducted and mantle carbon

A substantial amount of carbon can be transported into the mantle through plate tectonic subduction processes. All the layers in the subducted slab, i.e., sediment, oceanic crust and mantle lithosphere, can carry carbon in various forms, including C-O-H fluid and carbonate (Dasgupta and Hirschmann, 2010; Peacock, 1990). The carbon concentration in sediment varies between different subduction zones and the estimated amount varies in different studies. The average bound CO<sub>2</sub> in sediment is estimated to be 12 wt.% and the carbon flux is estimated to be  $1.6 \times 10^{11}$  kg/year from a 200-m-thick column of sediment by Peacock (1990), but only  $1.3$ - $1.7 \times 10^{10}$  kg/year by Dasgupta and Hirschmann (2010). The estimated CO<sub>2</sub> concentration in carbonate-bearing oceanic crust is 0.1-0.3 wt.%, corresponding to a carbon flux of  $6$ - $6.1 \times 10^{10}$  kg/year (Dasgupta and Hirschmann, 2010; Peacock, 1990). The carbon concentration in the mantle lithosphere is relatively unknown; one estimate of the carbon flux is  $3.6 \times 10^{10}$  kg/year (Dasgupta and Hirschmann, 2010).

In the mantle, carbon-bearing phases change with depth. In the shallow upper mantle (<200-250 km), oxidized phases such as CO<sub>2</sub>-rich fluid, carbonatite, and carbonated silicate melt are dominant (Dasgupta, 2013). At depths greater than 250 km, Fe<sup>2+</sup> disproportionates into Fe<sup>0</sup> and Fe<sup>3+</sup>; Fe<sup>3+</sup> is incorporated into silicate phases, making the mantle Fe-saturated (Frost et al., 2004; Rohrbach et al., 2007). Oxidized carbon, such as carbonate, can be reduced to diamond or Fe carbide, as demonstrated by many experimental studies (Palyanov et al., 2013; Rohrbach and Schmidt, 2011; Zhu et al., 2018).

## **1.5 Scope of this dissertation**

The theme of this dissertation is carbon in Earth's deep interior. Chapter 2 summarizes high-pressure experimental techniques and diagnostic methods used in this dissertation. Chapter 3 focuses on the effect of carbon on the physical properties of Fe-Ni liquids with implications for the chemical evolution of terrestrial planets and moons. In Chapter 4, the thermoelastic properties of a potential inner core carbon-bearing phase,  $\text{Fe}_7\text{C}_3$ , are explored to understand the Earth's inner core and its seismic anisotropy. Chapter 5 concerns the phase relations and melting behavior of the Fe-C-(H) system to investigate the occurrence of subducted carbon in the mantle. Finally, Chapter 6 summarizes the conclusions of the three chapters mentioned above and discusses further research on those topics.

# Chapter 2

## Methodology

This chapter introduces high-pressure generation devices and probing methods utilized in my research projects. Firstly, the high-pressure devices, Diamond Anvil Cell (DAC) and Large Volume Press (LVP), will be introduced. High-pressure and high-temperature conditions can be generated by those devices in order to simulate the conditions found in the deep interior of Earth, as well as other planets and moons. Secondly, the following analytical and probe methods will be introduced: The high-pressure techniques have been combined with various *in-situ* or *ex-situ* measurements to understand the physical properties of the samples. Particularly, synchrotron-based X-ray diffraction (XRD) was utilized to study the liquid structure of Fe-Ni-C system (Chapter 3), density and compressibility of Fe<sub>7</sub>C<sub>3</sub> (Chapter 4), as well as the reaction and melting in the Fe-C and Fe-C-H systems (Chapter 5). Finally, a theoretical method for the Density Functional Theory (DFT)-based molecular dynamics calculation (Chapter 3) will be introduced.

### 2.1 High-pressure devices

Pressure can be generated by dynamic shock-wave compression and static compression using DAC and LVP devices. Since only static techniques were employed in this dissertation, only the static compression devices will be introduced in this chapter. The advantage of DAC is that it can reach relatively high pressure and temperature which may cover the entire pressure and temperature range of the Earth's interior (770 GPa (Dubrovinsky et al., 2015) and 407 GPa and 5960 K (Tateno et al., 2015)) compared with LVP (tungsten carbide cubes: 25 GPa and sintered diamond anvils cubes: 110 GPa (Yamazaki et al., 2014) ). The major advantage of LVP is that the sample sizes (in millimeters) are orders of magnitude larger than those in DAC experiments (in microns). The large quenched sample recovered from an LVP experiment is more convenient for further analyses such as composition and texture.

### 2.1.1 Diamond anvil cell

The working principle of the diamond anvil cell is to compress a sample between two opposing diamonds with small polished culets. Diamond is used as the anvil because it is the hardest material in the world, and it is optically and X-ray transparent. A metal gasket, e.g. Rhenium (Re), Steel, or Beryllium (Be) is placed between culets of two well-aligned diamonds, and a hole is drilled on the gasket as the sample chamber (Figure 2.1). Pressure transmitting media such as Neon or KCl can be loaded into the sample chamber to produce a hydrostatic or quasi-hydrostatic environment surrounding the sample. Pressure generated by a force acting on the diamonds can be measured using the fluorescence of a ruby sphere (Mao et al., 1986), or using the equation of state of a pressure marker such as KCl, Pt or Au (Fei et al., 2007), or using the diamond edge method (Akahama and Kawamura, 2006) (Figure 2.1).

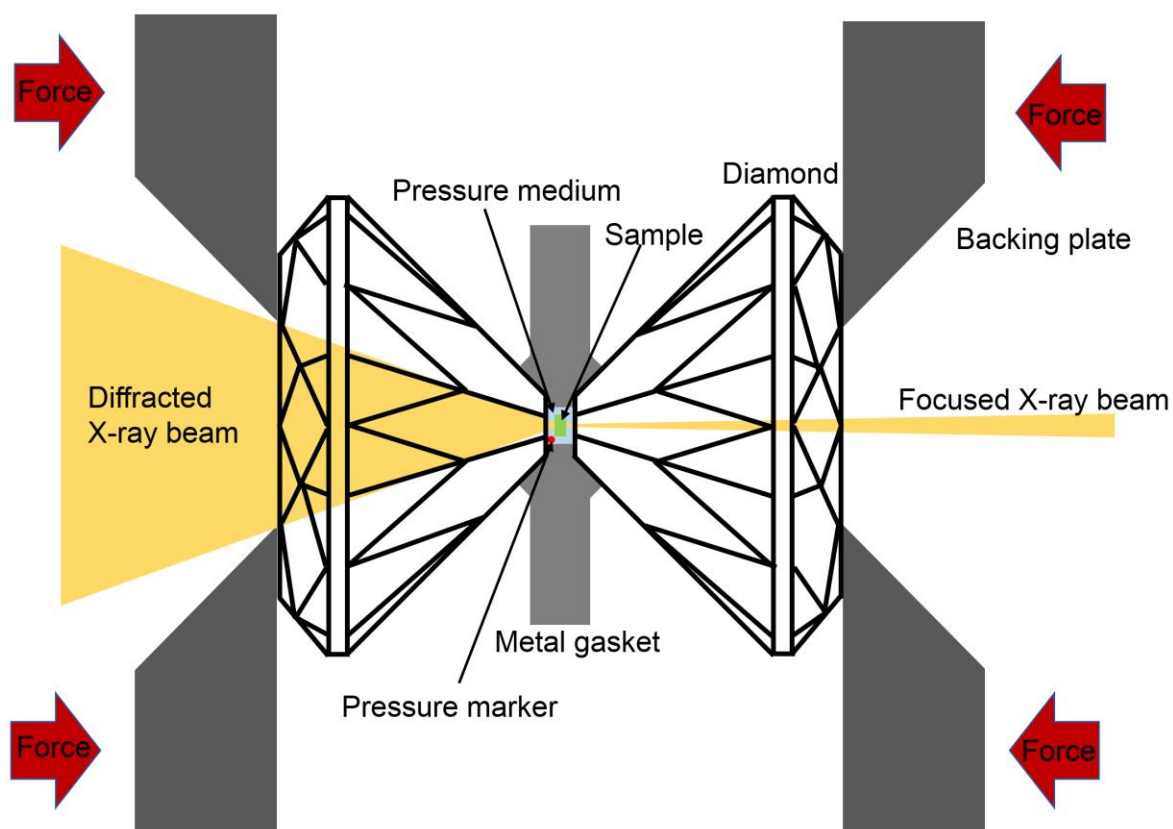


Figure 2.1. Schematics of the core components of a diamond anvil cell.

The equation  $P = F/A$ , where  $P$  is pressure,  $F$  is force and  $A$  is area, indicates that increasing force or reducing the area of the culet achieves higher pressure. In the DAC

experiment, there are two way to apply force to the culets - by turning screws of the DAC or by using a gas-driven membrane to control pressure remotely. The typical culet size of diamond can be 1000-100  $\mu\text{m}$ , which can be used to reach a pressure from several GPa up to 200 GPa. By introducing double-stage anvils with a contacting area less than 10  $\mu\text{m}$ , the diamond anvil cell can reach a pressure above 770 GPa (Dubrovinsky et al., 2015), far exceeding the pressure at the center of the Earth.

There are typically two ways to apply high temperature in DAC: resistance heating and laser heating. Externally resistance heating uses resistive wire or foils around the gasket/seat to heat the whole sample chamber. It provides the capability to heat the sample to  $\sim 800$  K without protective gases and to  $\sim 1300$  K with a protective atmosphere. The advantage of resistance heating is its small temperature gradient and accurate temperature measurement by thermocouples. However, the oxidation and fast graphitization of diamond at higher temperature limit the available temperature range ( $< 1300$  K). BX90 DAC is commonly used in the externally heated diamond anvil cell and is used in our study in Chapter 4 (Figure 2.2).

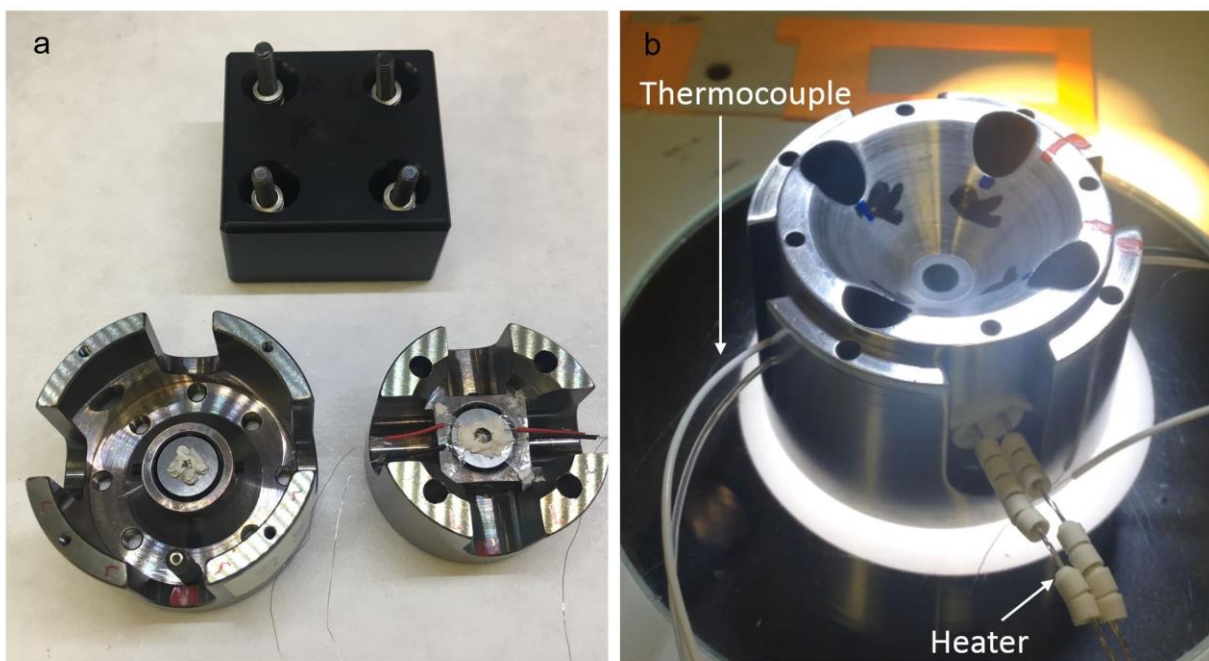


Figure 2.2. (a) Components of a BX90 DAC. (b) BX90 DAC with ring heater and thermocouple installed.

Pyrophyllite is typically used as the material of the ring heater base at the University of Hawai'i at Mānoa. A Roland MDX-40A CNC machine in Chen's laboratory is used to mill a ring with proper size (e.g. 22.30 mm OD, 7.94 mm ID and 2.25 mm thickness, for common BX90 DAC), with grooves and holes on both side surface for the resistive wires (Figure 2.3a). The machined base is then sintered in a furnace at 1523 K for more than 20 hours. The Pt 10 wt.% Rh wires (0.25 mm diameter) are typically used as the resistive heating wires. After wiring all the grooves and leaving two electrodes outside two or three times (Figure 2.3b), the wires are covered by laser-milled mica sheets for thermal and electrical insulation. The heaters have been tested and utilized in externally-heated DAC experiments numerous times and are found to be reliable and reproducible. To date, the maximum temperature reached was 900 K in open air and the maximum pressure reached was 80 GPa (Lai et al., 2018). After placing the thermocouple near the diamond culet, the heater can be placed in the piston side of the DAC fixed by Ultra-Temp 2300 °F ceramic tape strips (Figure 2.3c, d and e).

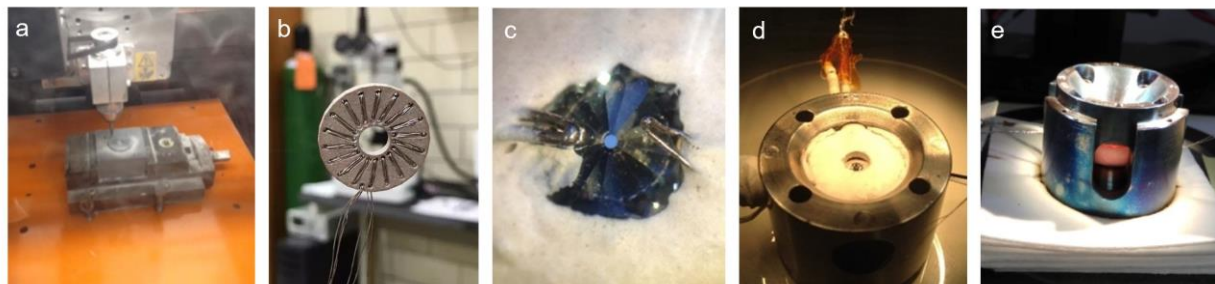


Figure 2.3. (a) Machining the ring heater base by the CNC machine. (b) The ring heater. (c) Two thermocouples placed near diamond culet. (d) Ring heater placed on cylinder side, fixed by Ultra-Temp Ceramic Tape strips. (e) Externally-heated BX90 DAC during the heating test.

Another way to achieve high temperature is laser heating. Depending on the sample, a Nd-YAG laser or a CO<sub>2</sub> laser can be employed. A Nd-YAG laser couples with colored materials like metals and dark minerals very well, while the CO<sub>2</sub> laser can be strongly absorbed by transparent samples. If only Nd-YAG lasers are available, in order to heat a transparent sample, a heat absorber such as Pt or Au should be mixed with the sample. In preparing the laser heating DAC, a thermal insulator such as KCl or Ne between the sample and diamond is crucial to effectively prevent heat loss through the diamond, which is a good conductor of heat. Temperatures of several thousand K can be obtained at high pressures. Temperature can be

measured by the grey body approximation (Shen et al., 2001). Compared with an externally-heated DAC, laser heating can reach higher temperature (as high as 7000 K), but the temperature fluctuates greatly and it has a large uncertainty. The temperature gradient in the heated sample area sometimes may further introduce chemical heterogeneity (Platten, 2006). In addition, temperatures <1200 K are usually not measurable. The symmetrical DAC is the most common DAC type and it is widely used in laser heating experiments, because it is very stable at high pressures and temperatures (Figure 2.4).

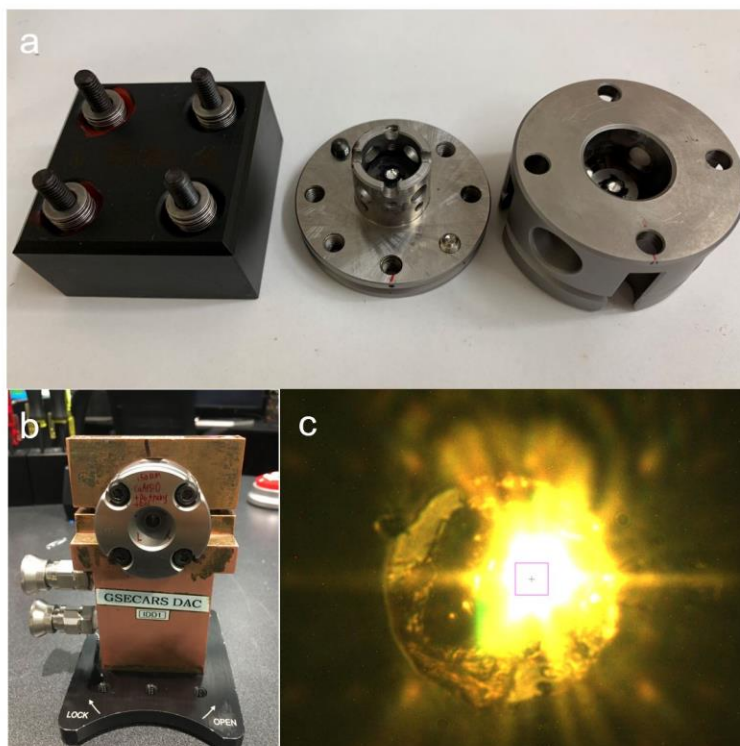


Figure 2.4. (a) Components of a symmetric DAC. (b) Symmetric DAC on a water-cooling holder for the laser heating experiment. (c) Sample chamber during laser heating.

### 2.1.2 Large volume press

Two types of LVP were used in this work: a Paris-Edinburg (P-E) press at beamline 16-BMB, Advanced Photon Source (APS), Argonne National Lab (ANL) and a 2000-ton Walker-type Multi-anvil Press (MAP) at the University of Hawai'i at Mānoa (UHM).

### *Paris-Edinburg press*

The P-E Press at 16-BMB, APS can normally reach up to 9 GPa and 2273 K. The set-up of the P-E Press is shown in Figure 2.5. The P-E press uses a resistive graphite heater to heat the sample to high temperature with small temperature gradients. Combined with synchrotron energy dispersive X-ray diffraction, it is an ideal device to study the physical properties of liquids such as liquid structure under high pressure and high temperature (Kono et al., 2014). In addition, the double-stage set-up of this P-E Press was recently developed to compress large samples to Mbar pressures (Kono et al., 2016).

For P-E press experiments in Chapter 3, high pressures were generated by a pair of cup-shaped tungsten carbide anvils with a 12 mm-diameter cup and 3 mm-diameter bottom. The cell assembly for liquid structure EDXD measurements in the P-E press is shown in Figure 2.6. A capsule for a sample of 0.2-2 mm in diameter and 1-2 mm in length was used. A graphite furnace was used to achieve high temperatures. A ring-shaped boron epoxy composite was used as the supporting gasket, which was surrounded by an outer polycarbonate plastic (Lexan) ring. The Boron epoxy (BE) gasket and  $ZrO_2$  caps in the assembly are good thermal insulators for high-temperature experiments. A MgO ring was placed between the BE gasket and graphite furnace to serve as a thermal insulating layer (Figure 2.6). Temperature was estimated from the power curve at each load and pressure of the sample in the BN capsule was estimated based on the thermal equation of state of MgO as well as the calibrated pressure gradient in the cell assembly at each temperature (Kono et al., 2014).

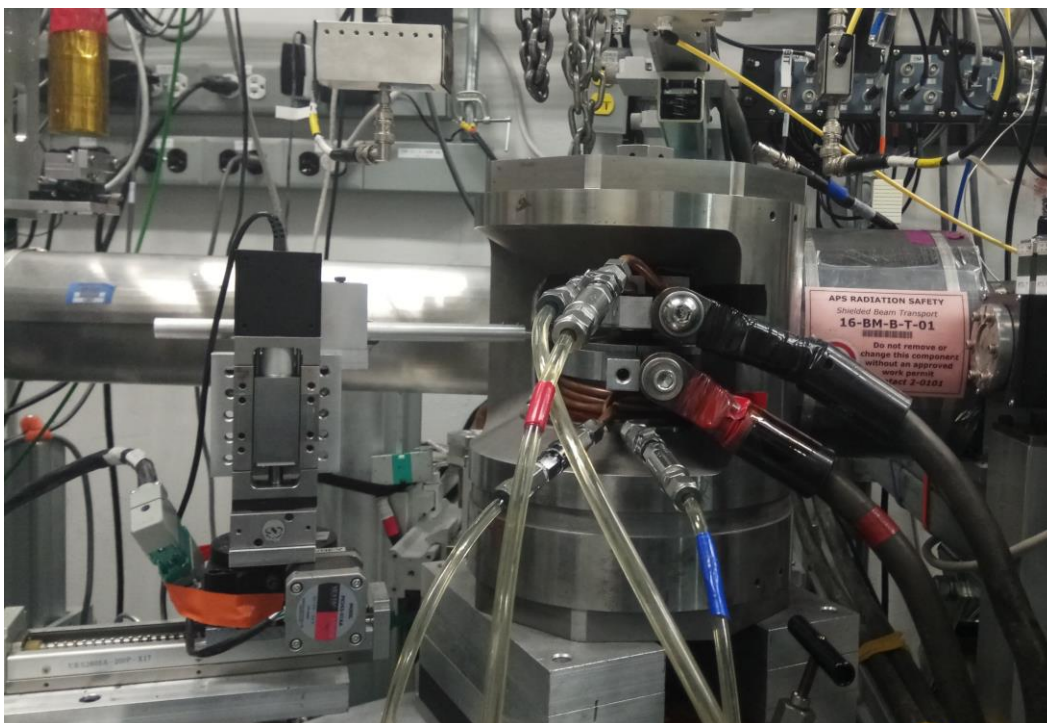


Figure 2.5. Experimental set-up of the Paris-Edinburgh press at 16-BMB, APS.

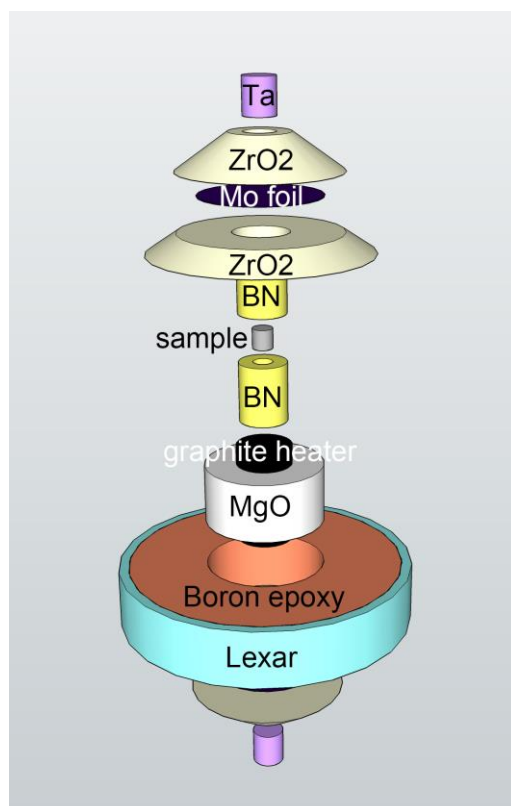


Figure 2.6. Illustration of the cell assembly for liquid structure measurements.

### *Multi-Anvil Press*

For LVP experiments in Chapter 5, a 2000-ton Walker-type multi-anvil press at University of Hawai'i at Mānoa was employed (Walker, 1991) (Figure 2.7a). A maximum of 2000 ton force can be inserted through the oil pump system. It is a 6-8 two-stage multi-anvil apparatus, which means a stage of six steel wedges and a stage of eight truncated tungsten carbide (WC) cubes are used to generate pressure (Figure 2.7b). The six steel wedges form a cubic cavity, into which the assembled eight WC cubes are placed. The eight cubes are provided with a [111] truncation forming an octahedral space, where a ceramic octahedron containing the sample is placed (Figure 2.7c). A hole is drilled through the center of the face of the octahedron, where a cylinder containing the sample can be loaded. Ceramic octahedra of 14, 10 or 8 mm edge-length can be compressed using tungsten carbide cubes with a truncated edge of 8 mm, 5mm or 3mm, respectively. The standard COMPRES 14/8 and 10/5 assemblies are shown in Figure 2.8. High temperature is generated by resistive heating of a graphite or rhenium furnace. Temperature is measured using thermocouples or is estimated by the power curve (Figure 2.8). Pressure was calibrated using phase transitions of pressure markers such as Bi (2.55 GPa and 7.7 GPa), ZnTe (9.6 and 12 GPa) at ambient temperature (Decker et al., 1972; Kusaba et al., 1993) and SiO<sub>2</sub>, Mg<sub>2</sub>SiO<sub>4</sub> or (Mg,Fe)<sub>2</sub>SiO<sub>4</sub> ( $\alpha$  to  $\beta$ ,  $\beta$  to  $\gamma$  and the decomposition of  $\gamma$  phase to bridgemanite & MgO or (Mg,Fe)O) at high temperature (Agee, 1998; Knibbe et al., 2018). The maximum pressure that can be reached using the 2000 ton multi-anvil press is 25 GPa using the 8/3 multi-anvil assembly. High temperatures up to ~ 2000 K can be achieved under high pressures and maintained for long duration (typically several days or even longer).

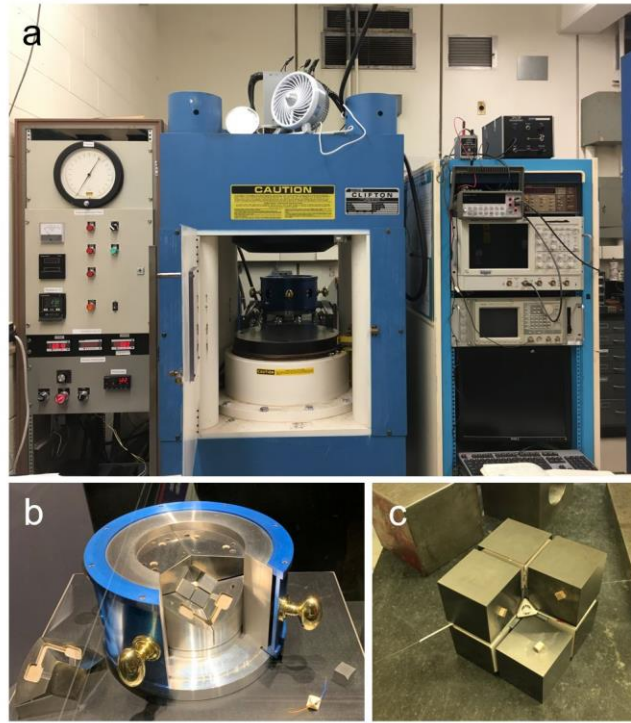


Figure 2.7. (a) 2000-ton multi-anvil press in HIG 116, University of Hawai'i at Mānoa. (b) Cross section of the walker-type module of the multi-anvil press exhibited in Smithsonian National Museum of Natural History. (c) Multi-anvil assembly with one WC cube removed to show the sample parts inside.

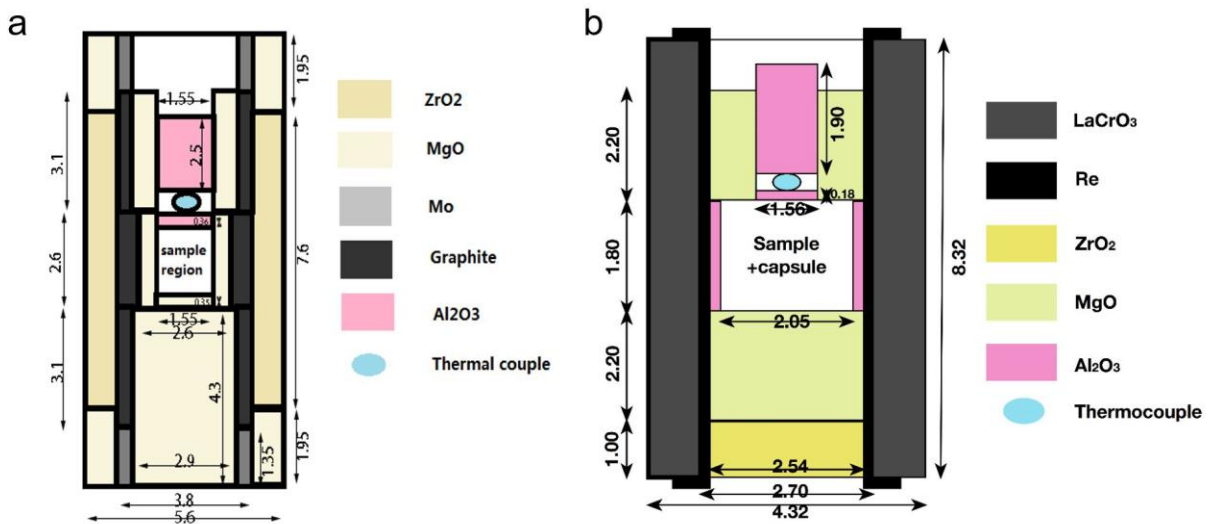


Figure 2.8. Schematics showing the standard COMPRES assembly of (a) 14/8 and (b) 10/5 without the ceramic octahedron.

## 2.2 X-ray diffraction

X-ray diffraction is an elastic X-ray scattering technique to obtain the structural information of materials from single crystals, powders and melts. Atoms scatter X-ray radiation, primarily through the electrons, producing secondary spherical waves spreading out from the electron. The scattered waves can be added constructively in a few specific directions, as determined by Bragg's law (Figure 2.9):

$$n\lambda = 2d_{hkl}\sin\theta$$

where  $\lambda$  is the wavelength of the incident beam (e.g. X-ray, neutron, electron),  $d_{hkl}$  is the spacing of the lattice planes with the Miller indices  $h$ ,  $k$  and  $l$  and  $\theta$  is the diffraction angle with respect to these planes.

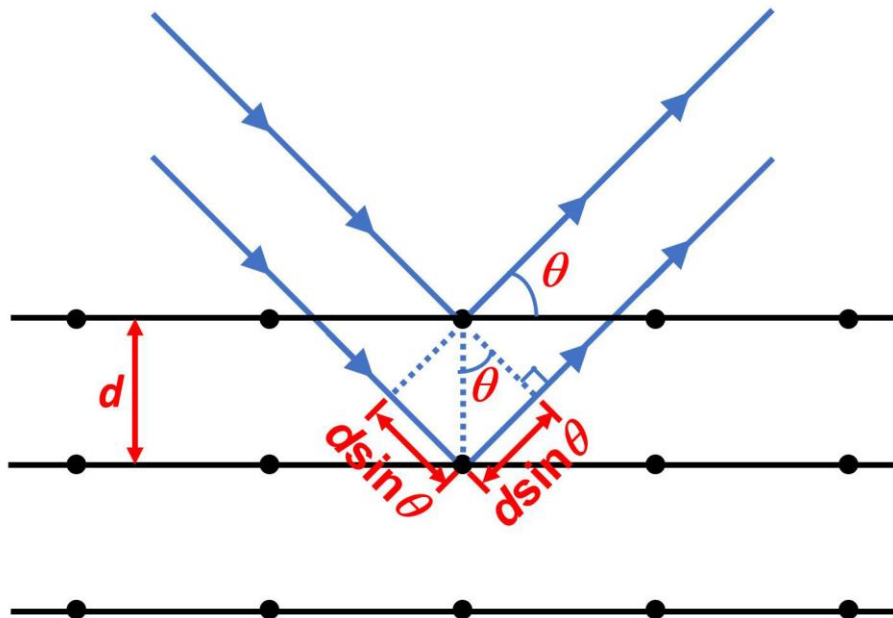


Figure 2.9. Illustration of Bragg's law.

There are two kinds of X-ray diffraction techniques-Angle dispersive X-ray diffraction (ADX) and Energy dispersive X-ray diffraction (EDXD). In ADXD, a monochromatic beam with a fixed wavelength is used. By measuring an angular spectrum using area detectors, the  $d_{hkl}$  values of a sample can be determined by Bragg's law. ADXD measurements combined with

externally-heated and laser-heated DACs were carried out in Chapters 4 and 5, respectively. In EDXD, a white beam and point detector are used to measure an energy spectrum at fixed angle. The  $d$  spacing values of crystals are also determined by Bragg's law. Liquid structure can be measured using multiangle EDXD method which will be described in detail in Chapter 3.

X-ray diffraction experiments can be carried out in synchrotron facilities or in in-house laboratories. In synchrotron facilities, X-rays are produced by high energy electrons as they circulate around storage rings. Because synchrotron X-ray has the advantages such as high brilliance, short wavelength, small focus, and good polarization, synchrotron X-ray diffraction is widely used in the field of mineral physics combined with DACs and LVPs (Figure 2.10). For in-house laboratory X-ray systems, copper (Cu), molybdenum (Mo) and silver (Ag) are commonly used as X-ray sources.

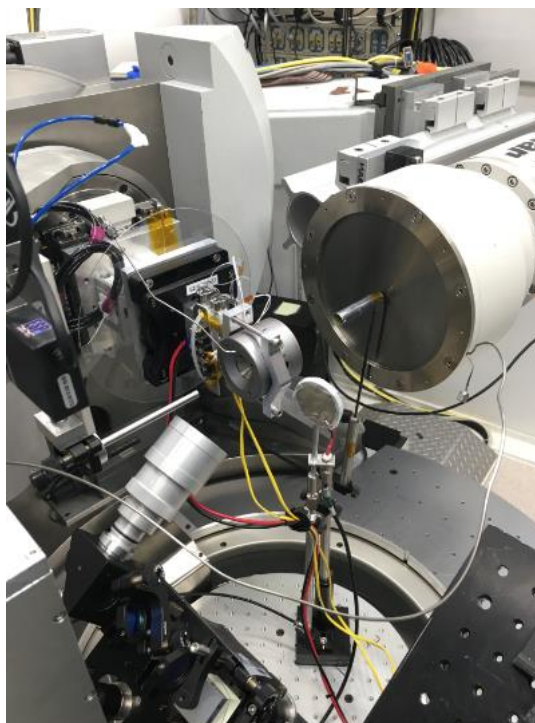


Figure 2.10. Set-up of high-pressure and high-temperature single-crystal XRD at beamline 13-BMC, APS.

Powder XRD is a rapid analytical technique primarily used for phase identification of a crystalline material and to determine unit cell parameters. Structure refinement of powder diffraction can also give information of the atomic positions, but with a limited accuracy because

only a small number of reflections can be used in the refinement, and because of uncontrolled textural effects under high pressure (Holzapfel and Isaacs, 1997). The sample should be finely ground and homogenous.

Single-crystal XRD can provide more detailed information on the crystal structure such as the atomic positions. From the atomic positions, information of bond-lengths, bond-angles, and details of site-ordering, can be obtained. Compared with powder XRD experiments, single-crystal XRD experiments require high-quality single crystals as samples. For a high-pressure DAC experiment, the crystal needs to be less than 20  $\mu\text{m}$  to prevent it from bridging two diamonds and thus being crushed into polycrystals. Single-crystal XRD usually takes longer than powder XRD. In a high-pressure single-crystal experiment, large openings of the DAC and short diamonds are required to obtain a wider  $2\theta$  range to reconstruct the crystal's reciprocal lattice.

## 2.3 Theoretical calculations

In high pressure research, theoretical calculations are an important complement to experiments. As described above, high-pressure experimental tools have their own limitations in pressure, temperature and fit to detection methods. Theoretical calculations, usually *ab initio* method based on density function theory, provide the capability of predicting the physics and chemistry of materials under extreme conditions, and to examine and understand experimental data.

The *ab initio* method, also known as first-principle calculation is a computational method using only basic physical constants and the principle of quantum physics to calculate the physical properties of atom, molecular, and condensed matter (Friesner, 2005). It requires no additional input of empirical parameters. The DFT is one of the most popular approaches employed in mineral physics research. As its name implies, the basis of DFT is that the ground-state energy of a many-body system is the unique functional of its electron density. It thus simplifies solving the complex many-body problem with  $3N$  spatial coordinates to solving the electron density with only 3 spatial coordinates.

The DFT calculation has achieved great success in studying the structures, electronic and elastic properties of crystals at ground state (0 K), although currently approximation treatments such as local-density approximation (LDA), generalized gradient approximation (GGA) or hybrid functionals to describe the exchange and correlation interactions still have difficulty in

describing the intermolecular force, the band gap of the semi-conductor, and the strongly correlated systems (Cohen et al., 2011). By introducing additional treatments like a quasi-harmonic approximation, it can also predict properties at high temperature. The DFT method can also be incorporated into Molecular dynamics (MD) calculations. MD calculation is one of the theoretical simulations used to study physical movements of atoms and molecules (Alder and Wainwright, 1959). MD calculations simulate the interaction of atoms and molecules at a fixed period of time. MD can be performed with selected fixed parameters like number of particles (N), volume (V) and energy (E), temperature (T), and pressure (P) to simulate the dynamics of a system under different statistical ensembles such as NVE, NVT and NPT. MD calculation using the DFT method to treat electronic interactions can be employed to study the structure and physical properties of liquid and amorphous materials at high pressure and high temperature (HPHT).

The great advantage of theoretical calculations in mineral physics is that the computational costs to calculate a system at ambient pressure vs at extreme high pressure are almost the same. By comparison, experimentally measuring a physical property at high pressure may be much more challenging, much higher in uncertainty and sometimes even technically impossible currently compared with measuring it at ambient pressure. The DFT calculations can provide crucial mineral physics data, including the structural phase transition, spin transition, equation of states, and elastic constants of Earth materials. These data can guide experimental designs and address controversial experimental results. More importantly, we can use reasonable experimental data at low pressure as a benchmark to check the robustness of the calculation setup, and then use the successful calculation setup to extend the results to high pressure, or we can use some measured properties to verify the calculation and use the calculation to extract much more relevant unmeasured information. For example, the liquid structure measurements in Chapter 3 can give us only the pair distribution function (PDF) which is a statistical result for the atomic coordination environment. If a DFT MD calculation can successfully reproduce the PDF, it is reasonable to investigate further the details of the liquid structure by calculation and to extend the pressure range. The calculations thus provide us with the critical structural information of the liquids which is unavailable from the experiments.

## Chapter 3

# Liquid Structure of Fe-Ni-C System: Implications for Planetary Chemical Evolutions

*This chapter has been published as **Xiaoqing Lai**, Bin Chen, Jianwei Wang, Yoshio Kono, and Feng Zhu (2017). "Polyamorphic Transformations in Fe-Ni-C Liquids: Implications for Chemical Evolution of Terrestrial Planets." *Journal of Geophysical Research: Solid Earth*, 122(12), 9745-9754.*

### 3.1 Abstract

During the formation of the Earth's core, the segregation of metallic liquids from silicate mantle should have left behind evident geochemical imprints on both the mantle and the core. Some distinctive geochemical signatures of the mantle-derived rocks likely own their origin to the metal-silicate differentiation of the primitive Earth, setting our planet apart from undifferentiated meteorites as well as terrestrial planets or moons isotopically and compositionally. Understanding the chemical evolution of terrestrial planetary bodies requires knowledge on properties of both liquid iron alloys and silicates equilibrating under physicochemical conditions pertinent to the deep magma ocean. Here we report experimental and computational results on the pressure-induced structural evolution of iron-nickel liquids alloyed with carbon. Our X-ray diffraction experiments up to 7.3 GPa demonstrate that Fe-Ni (Fe<sub>90</sub>Ni<sub>10</sub>) liquids alloyed with 3 and 5 wt. % carbon undergo a polyamorphic liquid structure transition at approximately 5 GPa. Corroborating the experimental observations, our first-principles molecular dynamic calculations reveal that the structural transitions result from the marked prevalence of three-atom face-sharing polyhedral connections in the liquids at >5 GPa. The structure and polyamorphic transitions of liquid iron-nickel-carbon alloys govern their physical and chemical properties and may thus cast fresh light on the chemical evolution of terrestrial planets and moons.

## 3.2 Introduction

The large majority of the Earth's core is liquid, with an outer liquid shell of ~96% by volume surrounding a central solid inner core (Poirier, 1994). The core is generally considered to consist primarily of Fe alloyed with ~5-8% Ni and a considerable amount of lighter elements (Anders, 1977; Birch, 1964; Li and Fei, 2014; McDonough and Sun, 1995). The leading candidates for the light elements are sulfur (S), silicon (Si), oxygen (O), hydrogen (H) and carbon (C) (Birch, 1952, 1964; Li and Fei, 2014; Poirier, 1994). A number of terrestrial planets and moons in our Solar System also likely possess partially or fully molten iron-rich cores as the Earth (e.g., Chen et al., 2008; Dasgupta et al., 2009; Hauck et al., 2013; Weber et al., 2011). The knowledge on the structure, dynamics and chemical evolution of the planetary cores thus hinges on the physical properties of liquid Fe alloyed with light elements under high pressures and temperatures.

The actual identity and abundance of light elements in planetary cores remain as a chief unsolved question in Earth and planetary sciences, although it is crucial for our understanding of the chemical evolution of the planets. The Fe-S system is commonly assumed as the composition of planetary cores and its liquid properties are often used to construct models for the cores of terrestrial planets and moons, such as Mercury (Chen et al., 2008; Hauck et al., 2013), Mars (Fei and Bertka, 2005; Stewart et al., 2007), Ganymede (Hauck et al., 2006), and the Moon (Jing et al., 2014). Other systems involving Fe with one or more light elements such as O, C, and Si, however, are likely as important based on our current understanding of planetary evolution. In the present study, the Fe-Ni-C system is considered, because of the high cosmochemical abundance of carbon, frequent occurrence of Fe carbide phases in meteorites, and high affinity and solubility of carbon in Fe-Ni liquids under the core-mantle differentiation conditions (Chen and Li, 2016; Dasgupta and Walker, 2008; Wood, 1993; Wood et al., 2013). Limited experimental data on the thermo- and visco-elastic properties of the Fe-Ni-C liquids however have restricted our discussion of carbon-bearing planetary core compositional models (Kuwabara et al., 2016; Sanloup et al., 2011; Shimoyama et al., 2013; Shimoyama et al., 2016; Terasaki et al., 2010).

The structure, physical and chemical properties of molten Fe and its alloys with Ni and light elements would advance our understanding of the chemical and physical processes during the core-mantle differentiation in the early history of the Earth and other terrestrial planetary bodies (Stevenson, 1981). One of the striking but controversial phenomena of Fe and Fe-light-element liquids is the possible existence of a pressure-induced polyamorphic transition, primarily based on characteristic features such as changes in bond distance and density. By X-ray diffraction measurements, Sanloup et al. (2000) reported a structural change in liquid Fe from *bcc*-like to *bcc-fcc*-like local order structure in the vicinity of the  $\delta$ - $\gamma$ -liquid triple point at  $\sim 5$  GPa, based on the appearance of two distinct peaks of the second peak in the PDF. In contrast, the splitting of the second peak of PDF was not obvious in the other two measurements of liquid Fe up to 6.4 GPa (Kono et al., 2015) and 58 GPa (Shen et al., 2004), respectively. Further, the incorporation of certain light elements such as C in liquid Fe may significantly alter the liquid structures and properties. Notably for the Fe-C system, Shibazaki et al. (2015) inferred a liquid structure transition in Fe-3.5wt.% C liquid at  $\sim 5$  GPa from peak distance changes in their experimentally determined PDFs, but detailed structural information of the liquid was lacking. Liquid structural transitions may also be inferred from some observed changes in physical and chemical behaviors of liquid Fe alloys at high pressures. The densities of Fe-5.7 wt.% C (Sanloup et al., 2011) and Fe-3.5wt.% C (Shimoyama et al., 2013) both showed marked changes at  $\sim 5$  GPa. The non-linear systematics in the metal-silicate partitioning behavior for trace elements (i.e., Ni, Co, and W) were also assumed to result from the polyamorphic transition, inferred from a liquid compressibility change in the Fe-C liquid (Sanloup et al., 2011).

Despite numerous attempts, the polyamorphic transitions of iron-rich liquids, however, remain elusive, largely due to subtle changes of the liquid structure and the ambiguities of liquid structural data such as the observed PDFs reported in most previous studies for understanding liquid structure transitions. The intrinsic nature of the structural evolution of the liquids with pressure, crucial for our understanding of the liquid properties, has been hardly investigated thoroughly. In the present study, we report the structure evolution of liquid Fe<sub>90</sub>Ni<sub>10</sub>-5wt.% C and Fe<sub>90</sub>Ni<sub>10</sub>-3wt.% C (hereafter referred to as FeNi5C and FeNi3C, respectively) alloys up to 7.3 GPa and 1773 K, using a synergistic approach by combining energy-dispersive X-ray diffraction experiments with first-principles molecular dynamics simulations. The cooperation between experiments and calculations provides critical structural information of the liquids for

our understanding of the intrinsic nature of the pressure-induced structural rearrangements of the liquids and the resultant effects on the liquid properties.

### **3.3 Materials and methods**

#### **3.3.1 High-pressure experiments**

Our starting materials for FeNi<sub>5</sub>C and FeNi<sub>3</sub>C were Fe (99.9+% purity, Aldrich Chemical Company) and Ni (99.99% purity, Aldrich Chemical Company) powders mixed with graphite (99.9995% purity, Alfa Aesar Company) powder. The mixtures were ground in acetone using an agate mortar for more than 1 hour to achieve composition homogeneity, and then dried in a vacuum oven at high temperature (~383 K) for overnight before being sealed in glass vials. The powder samples were cold pressed to cylinders of 1 mm in diameter and 1 mm in length and placed in the BN capsule. The high-pressure experiments were carried out at the High Pressure Collaborative Access Team (HPCAT) Sector 16-BMB beamline of the APS, ANL, using the VX-3 type Paris-Edinburgh press (Figure 3.1) (Kono et al., 2014). The temperature was estimated from the power curve at each load (Kono et al., 2014) and the pressures of the sample were estimated based on the thermal equation of state of MgO as well as the calibrated pressure gradient in the cell assembly at each temperature (Kono et al., 2014). The uncertainty of the pressures is estimated to be up to 0.15 GPa and the temperature uncertainty is approximately 25 K (Kono et al., 2014).

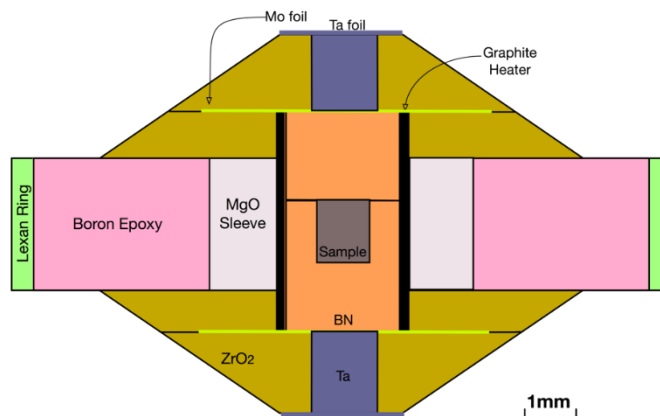


Figure 3.1. Cross-section of the cell assembly for liquid structure measurements in a Paris-Edinburgh press, modified after (Kono et al., 2014). The Fe-Ni-C sample is encapsulated in a boron nitride (BN) sample chamber.

At each experimental run, the cell assembly was cold compressed to the target load in the P-E press, and then sintered at 1073 K for at least 0.5 hour to minimize the possibilities of liquid sample leaking. The sample was further heated to the target temperature at the rate of approximately 1 K per second. The disappearance of crystalline diffraction peaks was utilized as the criterion of the onset of sample melting (Figure 3.2). The multi-angle EDXD measurements were used to determine the liquid structure of the FeNi5C and FeNi3C alloys up to 7.3 GPa (Table 3.1). The EDXD data were collected at various  $2\theta$  angles ( $4^\circ$ ,  $5^\circ$ ,  $7^\circ$ ,  $9^\circ$ ,  $12^\circ$ ,  $16^\circ$ ,  $21^\circ$ ,  $27^\circ$ ,  $33^\circ$ ) (Figure 3.3). For each set of EDXD measurements, the total structure factor,  $S(q)$ , was obtained by merging the fragmented structure factor at those  $2\theta$  angles with respect to the highest angle fragment. An evenly spaced  $S(q)$  was obtained after error-weighted spline-smoothing of overlapped structure factor fragment (Figure 3.3 and 3.4a). The reduced PDF,  $G(r)$ , were obtained by iteration of the Fourier and inverse Fourier transformation of the  $S(q)$  using a maximum  $q$  range of  $18.0 \text{ \AA}^{-1}$  by an Igor Pro (WaveMetrics, Lake Oswego, OR, USA) procedure by Kono et al. (2014) (Figure 3.4b). As the oscillatory features of the structure factor persist at the  $q_{\text{max}}$ , a resolution broadening correction function, known as the Lorch function, was utilized to remove the artifact “ghost ripples” in the PDFs (Kono et al., 2014).

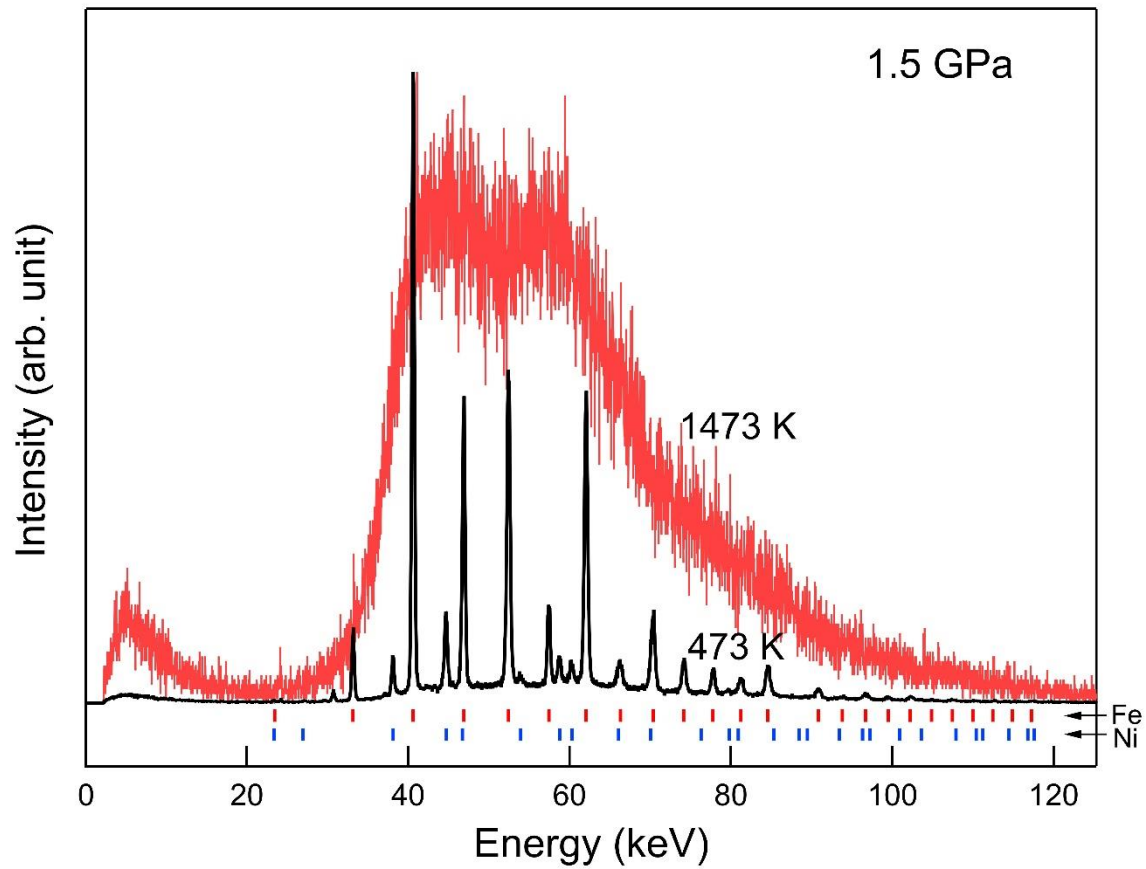


Figure 3.2. EDXD patterns before and after melting the sample  $(\text{Fe}_{90}\text{Ni}_{10})\text{-5wt.\%C}$  collected at  $15^\circ$ . The EDXD pattern before melting can be indexed by *bcc*-Fe (Space group *Im3m*) and *fcc*-Ni (Space group *Fm3m*) phases. Graphite phase is not shown in the EDXD pattern before melting because the carbon atom has an X-ray scattering factor 50 times lower than Fe and Ni. The X-ray diffraction pattern for the liquid was scaled up for clarity.

Table 3.1. Peak positions for the integrated 1st and 2nd atomic shells.

$P$ (GPa)	$T$ (K)	$r_1$ (Å)	$r_{2s}$ (Å)		$r_{2m}$ (Å)	
Fe <sub>90</sub> Ni <sub>10</sub> -5wt.% C						
1.5	1523	2.561	(.004)	4.299	(.019)	4.950 (.015)
2.6	1473	2.555	(.004)	4.292	(.018)	4.946 (.015)
3.8	1573	2.552	(.003)	4.261	(.021)	4.921 (.016)
4.8	1573	2.547	(.003)	4.193	(.018)	4.883 (.013)
5.7	1573	2.546	(.004)	4.207	(.020)	4.886 (.014)
6.3	1673	2.544	(.003)	4.216	(.020)	4.884 (.014)
6.7	1673	2.545	(.006)	4.197	(.045)	4.910 (.031)
6.3*	1673	2.543	(.002)	4.219	(.019)	4.895 (.013)
6.8*	1673	2.541	(.002)	4.234	(.022)	4.897 (.014)
Fe <sub>90</sub> Ni <sub>10</sub> -3wt.% C						
3.4	1773	2.546	(.003)	4.289	(.019)	4.935 (.017)
4.2	1773	2.552	(.003)	4.271	(.024)	4.919 (.018)
5.1	1773	2.543	(.003)	4.203	(.020)	4.885 (.014)
6.3	1773	2.544	(.003)	4.182	(.022)	4.876 (.014)
7.3	1773	2.542	(.003)	4.179	(.020)	4.872 (.013)

Note: The  $r_1$  peak position for the first NNs near 2.55 Å at each pressure was fitted by an exponentially modified Gaussian (ExpModGaussian) function in the multi-peak fitting package of the Igor Pro software (WaveMetrics, Lake Oswego, OR, USA). The peak for the second NNs at 4-5 Å were fitted by two Gaussian peaks  $r_{2s}$  and  $r_{2m}$ . Uncertainties were estimated from the standard deviation of the fittings enclosed in parentheses. Pressure uncertainty is typically about 0.15 GPa and temperature uncertainty is about 25 K (Kono et al., 2014).

\* Data collected from a different experimental run with 80% of the collection time of the other data points.

### 3.3.2 Theoretical calculations

The first-principles MD simulations were based on the Density Functional Theory and plane wave basis sets as implemented in VASP (Vienna Ab initio Simulation Package) (Kresse and Furthmüller, 1996). The Projector-Augmented Wave method and exchange-correlation as parameterized by the PBE (Perdew, Burke and Ernzerhof) functional were applied in the GGA (Blöchl, 1994; Perdew et al., 1992). A supercell containing 140 Fe, 14 Ni and 38 C was created for calculation. For Fe, 8 electrons (3d and 4s) was treated as valence electrons and the core electrons had [Ar] configuration. For Ni, 10 electrons were treated as valence electrons and the core electrons had [Ar] configuration. For C, 4 electrons were treated as valence electrons and the core electrons had [He] configuration.

All the calculations were performed with a system size of 192 atoms and the energy cut-off for the plane-wave basis was set to 520.00 eV, and  $\Gamma$  point Brillouin Zone sampling for the molecular dynamics simulations. Ferromagnetic ordering was initiated at the start of molecular dynamics simulations but allowed to evolve during the equilibration simulations. Molecular-dynamics simulations were performed using a NVT ensemble with the Nosé-thermostat for  $\sim 3$  ps for equilibration, which was checked by monitoring a number of parameters including electronic cycle convergence, temperature, pressure, potential energy of the systems, the partition of the kinetic energy of Fe, Ni and C subsystems, and displacement of atoms, among other system parameters. The time step is 1 fs. The total energy drift was  $\sim 2-5$  meV/atom/ps. Extensive tests were performed to balance between the accuracy and duration of the simulations by systematically tuning simulation parameters including those related to convergences, real space projection, and time step. After equilibrations, simulations run up to  $\sim 7$  ps for statistical analysis. For comparison with our experimental results, the intensities of radial distribution functions (RDFs) of different ionic pairs (Fe-Fe, Fe-Ni, Ni-Ni, Fe-C, Ni-C and C-C pairs) are scaled using the scattering factors derived under the experimental conditions.

## 3.4 Results

### 3.4.1 Structure measurements for Fe-Ni-C liquids

The total structure factor  $S(q)$  of the FeNi<sub>5</sub>C and FeNi<sub>3</sub>C liquids at each pressure was obtained by analyzing the multi-angle EDXD patterns collected at angles ranging from  $4^\circ$  to  $33^\circ$  in the P-E large volume press (Figures 3.3 and 3.4 for representative data). The first sharp peak

or the main peak,  $q_1$ , of  $S(q)$  characterizes the short-range order in the fluid. The  $q_1$  peaks of FeNi5C and FeNi3C at all pressures were fitted by Lorentzian functions and we observed an apparent change in its positions at approximately 5 GPa (Figure 3.5a, 3.5c and 3.6). The observed evolution of  $q_1$  position with pressure implies that both FeNi5C and FeNi3C liquids may undergo structural change at approximately 5 GPa, similar to the Fe-3.5wt% C liquid (Shibazaki et al., 2015).

The PDFs,  $G(r)$ , were obtained from the Fourier transformation of  $S(q)$  using a maximum  $q$  range of  $18.0 \text{ \AA}^{-1}$  (Figure 3.5b, 3.5d and Figure 3.4b). The first peaks ( $r_1$ ) of the PDFs near  $2.56 \text{ \AA}$  for both FeNi5C and FeNi3C liquids are sharp and simple, which are associated with the short-range orders (SRO) of the first nearest-neighbor shell (NNs) (Figure 3.5b & 5d). As shown in Figure 3.7, the peak positions  $r_1$  ( $\sim 2.56 \text{ \AA}$  at 2 GPa) for both FeNi5C and FeNi3C liquids are slightly lower than that of Fe ( $\sim 2.58 \text{ \AA}$  at 2 GPa) (Kono et al., 2015; Sanloup et al., 2000). For both the FeNi5C and FeNi3C liquids,  $r_1$  decreases almost linearly with pressure and no notable changes were observed up to the pressure of 7.3 GPa.

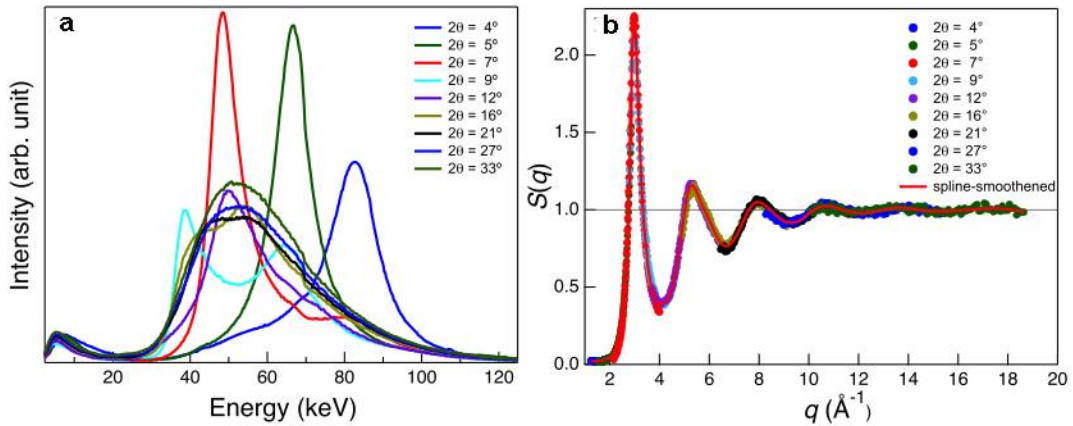


Figure 3.3. Representative experimental data and total structure factor  $S(q)$  of  $\text{Fe}_{90}\text{Ni}_{10}$ -5wt.% C liquid at 1.5 GPa and 1523 K. (a) Energy dispersive X-ray diffraction spectra of  $\text{Fe}_{90}\text{Ni}_{10}$ -5wt.% C liquid collected at  $2\theta$  angles from  $4^\circ$  to  $33^\circ$ . (b) Total structure factor  $S(q)$  of the  $\text{Fe}_{90}\text{Ni}_{10}$ -5wt.% C liquid at 1.5 GPa and 1523 K composed of structure factor fragments from measurements at different  $2\theta$  angles. The red solid curve is obtained after error-weighted spline-smoothing of the overlapped structure factor fragments.

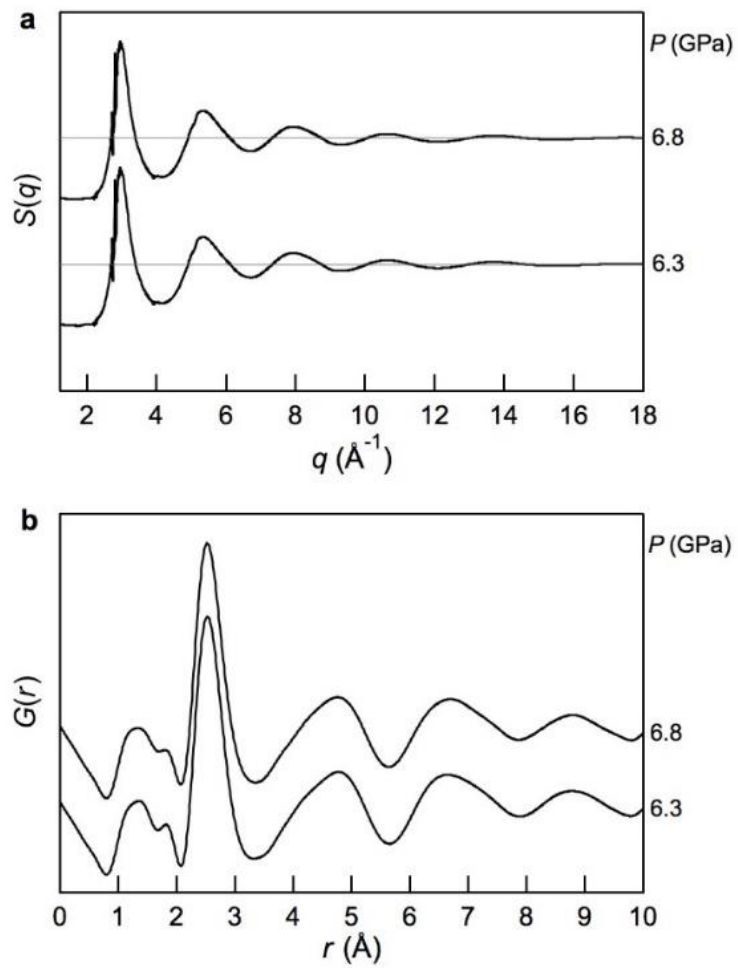


Figure 3.4. Total structure factor  $S(q)$  and reduced pair distribution function  $G(r)$  of  $\text{Fe}_{90}\text{Ni}_{10}$ -5wt.%C liquids at high pressure and temperature. (a)  $S(q)$ , and (b)  $G(r)$  of  $\text{Fe}_{90}\text{Ni}_{10}$ -5wt.%C liquids at 6.3 and 6.8 GPa.

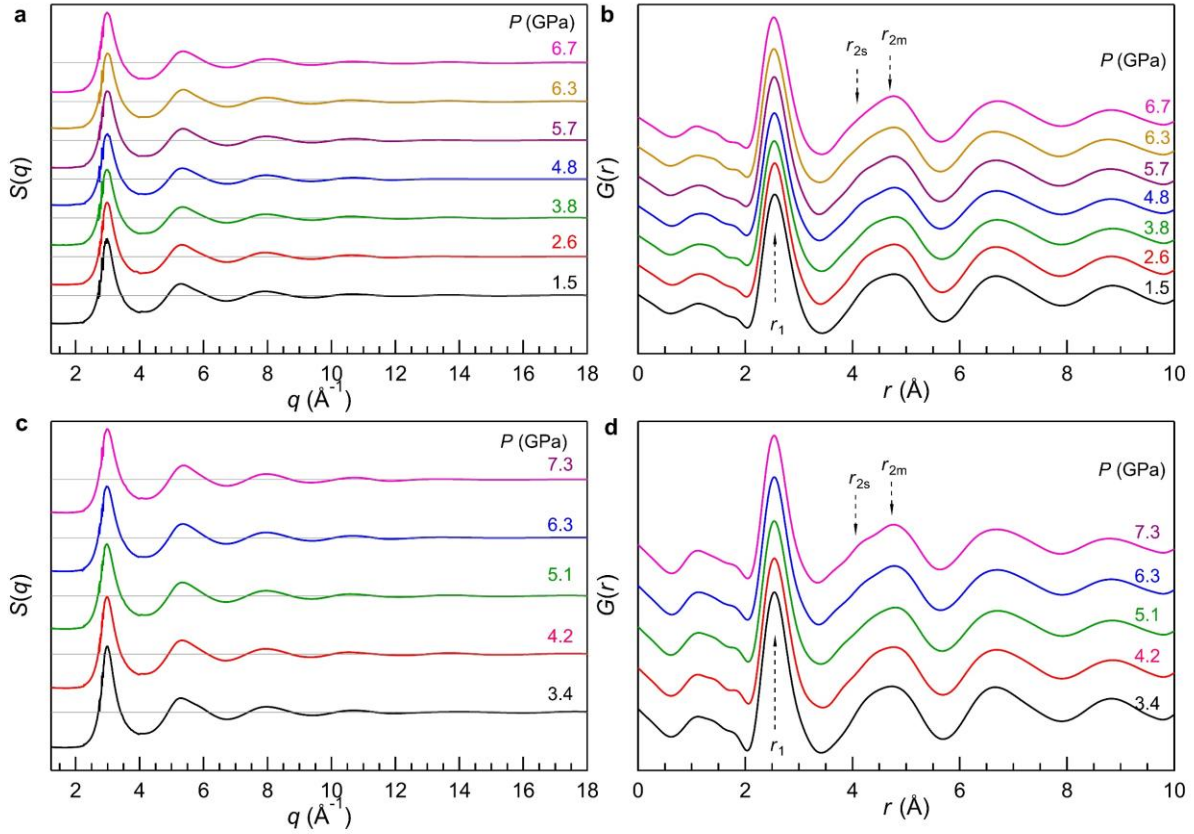


Figure 3.5. Representative total structure factor  $S(q)$  and reduced pair distribution function  $G(r)$  of  $\text{Fe}_{90}\text{Ni}_{10}$ -5wt.% C and  $\text{Fe}_{90}\text{Ni}_{10}$ -3wt.% C liquids at high pressure and temperature. (a)  $S(q)$  and (b)  $G(r)$  of  $\text{Fe}_{90}\text{Ni}_{10}$ -5wt.% C liquids up to 6.7 GPa, (c)  $S(q)$  and (d)  $G(r)$  of  $\text{Fe}_{90}\text{Ni}_{10}$ -3wt.% C liquids up to 7.3 GPa.

At each pressure, the second NNs peaks ( $r \sim 4\text{--}5 \text{ \AA}$ ) in  $G(r)$  for both liquids show much richer features than the first NNs peak at  $r_1$ , indicating the SROs of the second NNs become more complex. In Figure 3.3, we observed an obvious splitting of the second NNs peak of  $G(r)$  at each pressure. The second NNs peaks were fitted by two Gaussian-shaped sub-peaks: a shoulder peak at  $r_{2s}$  and a main peak at  $r_{2m}$  (Table 3.1 and Figure 3.4). The  $r_{2s}$  and  $r_{2m}$  values for both liquids were found to drop markedly at  $\sim 5 \text{ GPa}$ ; the magnitude of the change in  $r_{2s}$  is approximately  $-0.1 \text{ \AA}$  at  $\sim 5 \text{ GPa}$ , a factor of 2 of that for  $r_{2m}$  (Figure 3.4). The change and differentiation of  $r_{2s}$  and  $r_{2m}$  are indicative of a polyamorphic transition. As shown in Figure 3.4, previous studies reported similar but somewhat ambiguous changes of  $r_2$  associated with the second NNs for Fe (Kono et al., 2015; Sanloup et al., 2000) and Fe-3.5wt.% C liquids (Shibazaki et al., 2015), in which the second peak was treated as a single peak in the PDFs and observed to

noticeably shift to lower values at ~5–6 GPa. The previous observations of the changes in  $r_2$  with pressure for the Fe-rich liquids, however, were not sufficient to provide critical information on liquid structure and its evolution with pressure. The underlying nature of the liquid structure and structural transition at ~5 GPa may be unveiled by interpreting the rich feature of the second NNs peak observed in our study for FeNi5C and FeNi3C with the aid from our MD calculations.

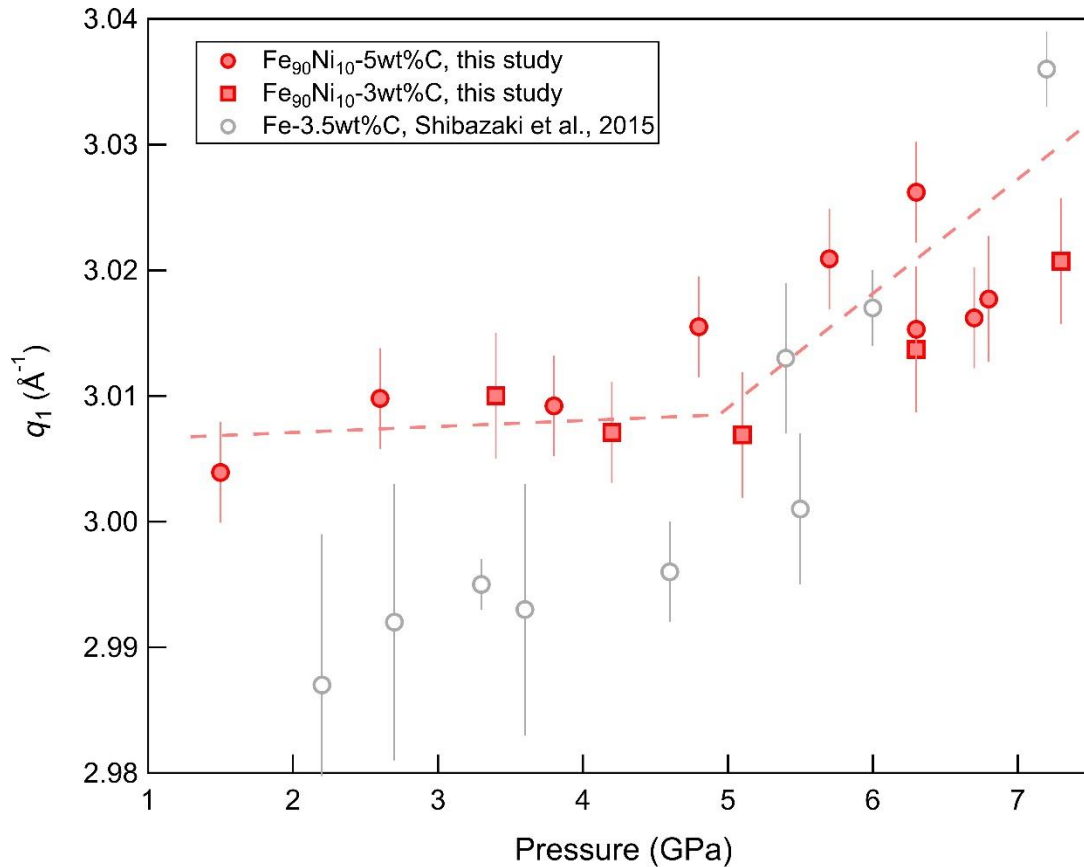


Figure 3.6. Pressure dependence of the main  $S(q)$  peak of Fe-Ni-C liquids. Solid red symbols denote data for the FeNi5C and FeNi3C liquids from the present study. Open gray symbols denote the data for the Fe-3.5 wt%C liquid [Shibazaki *et al.*, 2015]. The peak position at each pressure was determined by fitting the first  $S(q)$  peak with a Lorentzian function [Shibazaki *et al.*, 2015]. The dashed line serves as a guide for eyes to show the change at approximately 5 GPa.

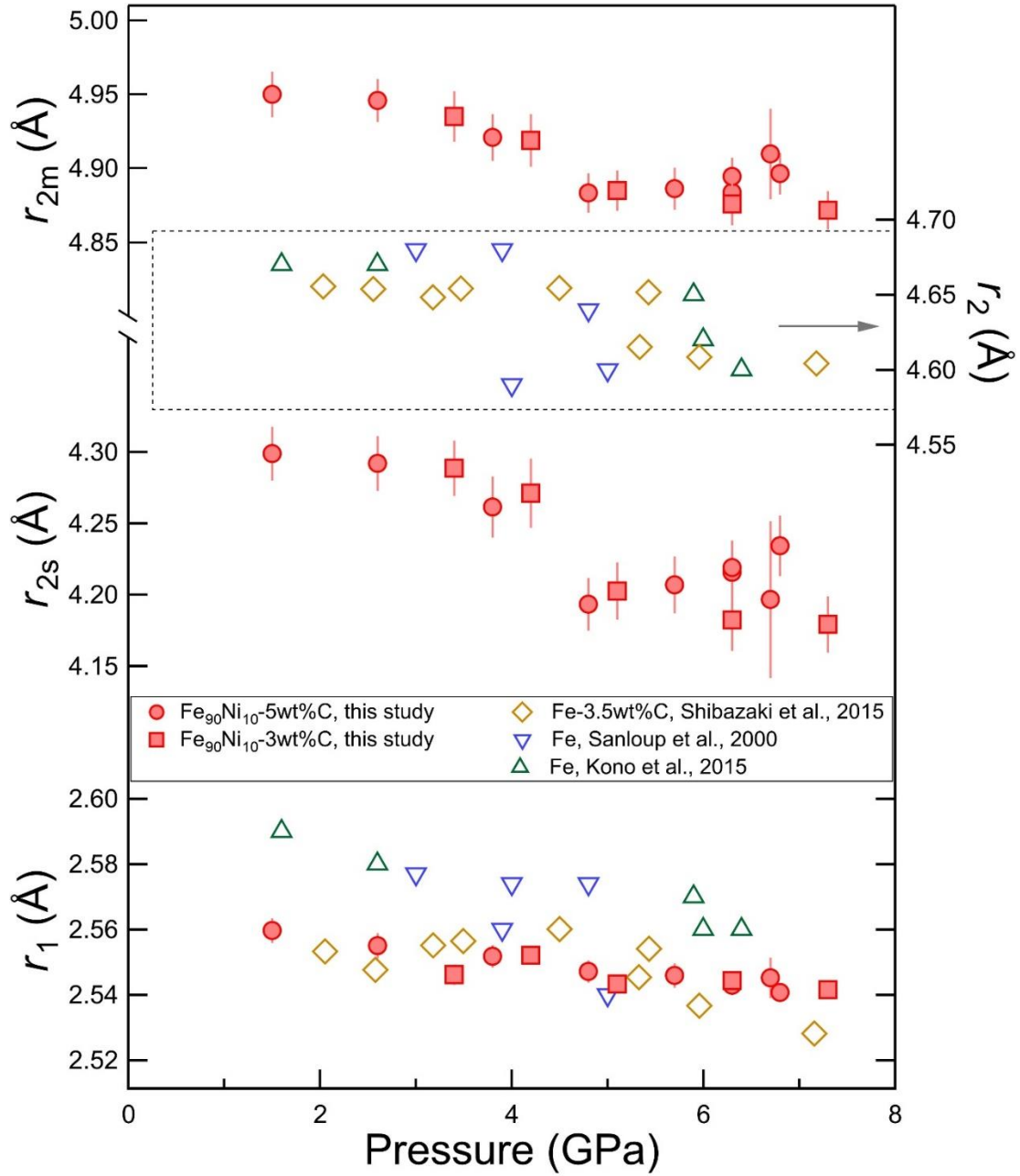


Figure 3.7. Pressure dependence of peak positions for the 1<sup>st</sup> and 2<sup>nd</sup> nearest-neighbor shells (NNs) from reduced pair distribution functions  $G(r)$  of  $\text{Fe}_{90}\text{Ni}_{10}$ -5wt.% C and  $\text{Fe}_{90}\text{Ni}_{10}$ -3wt.% C liquids (this study), Fe-3.5wt.% C liquid, and Fe liquid (Kono et al., 2015; Sanloup et al., 2000; Shibazaki et al., 2015). The first peaks of  $G(r)$  at 2.5-2.6 Å are fitted by one single peak ( $r_1$ ) in all the studies in the figure. The second peaks of  $G(r)$  are fitted by one single peak ( $r_2$ ) in other studies (Kono et al., 2015; Sanloup et al., 2000; Shibazaki et al., 2015), but are best fitted by two subset peaks shown as a shoulder peak ( $r_{2s}$ ) at ~4.2-4.3 Å and a main peak ( $r_{2m}$ ) at ~4.87-4.95 Å for the Fe-Ni-C liquids in this study. The uncertainties were estimated from standard deviations of the peaking fittings.

### 3.4.2 Molecular dynamics calculations for Fe-Ni-C liquids

We performed first-principles MD calculations for the Fe<sub>91</sub>Ni<sub>9</sub>-5wt.% C liquids to decipher the nature of the observed polyamorphic transition. Our computational results can reproduce the peak positions and peak shapes of PDFs for the FeNi<sub>5</sub>C liquids (Figure 3.8): The first NNs peaks of the FeNi<sub>5</sub>C liquid shown as  $r_1$  in the PDFs and the second NNs peaks at 4-5 Å are dominated by Fe-Fe and Fe-Ni pairs (Kono et al., 2015; Sanloup et al., 2000). Notably, our computational results indicate that the peak at approximately 1.8 Å corresponds to Fe-C and Ni-C pairs (Figure 3.8). This peak, however, becomes considerably small after normalizing the computed PDFs using their X-ray scattering factors, because the carbon atom has an X-ray scattering factor 50 times lower than Fe and Ni. Our experimental PDFs of FeNi<sub>5</sub>C and FeNi<sub>3</sub>C liquids also show a weak but visible peak at ~1.8-1.9 Å at each pressure of the measurements (Figure 3.4 and Figure 3.5). As suggested by our MD simulations and previous MD results [Soblev and Mirzoev, 2013], this peak is associated with the Fe-C pairs. The calculated PDFs from MD simulations yield no peak or zero intensity for  $r < 1.6$  Å. It should be noted that the peaks for  $r < 1.6$  Å in the experimentally determined PDFs have no physical meanings and are likely due to the artifact from the Fourier transformations of  $S(q)$  data at limited  $q$  ranges.

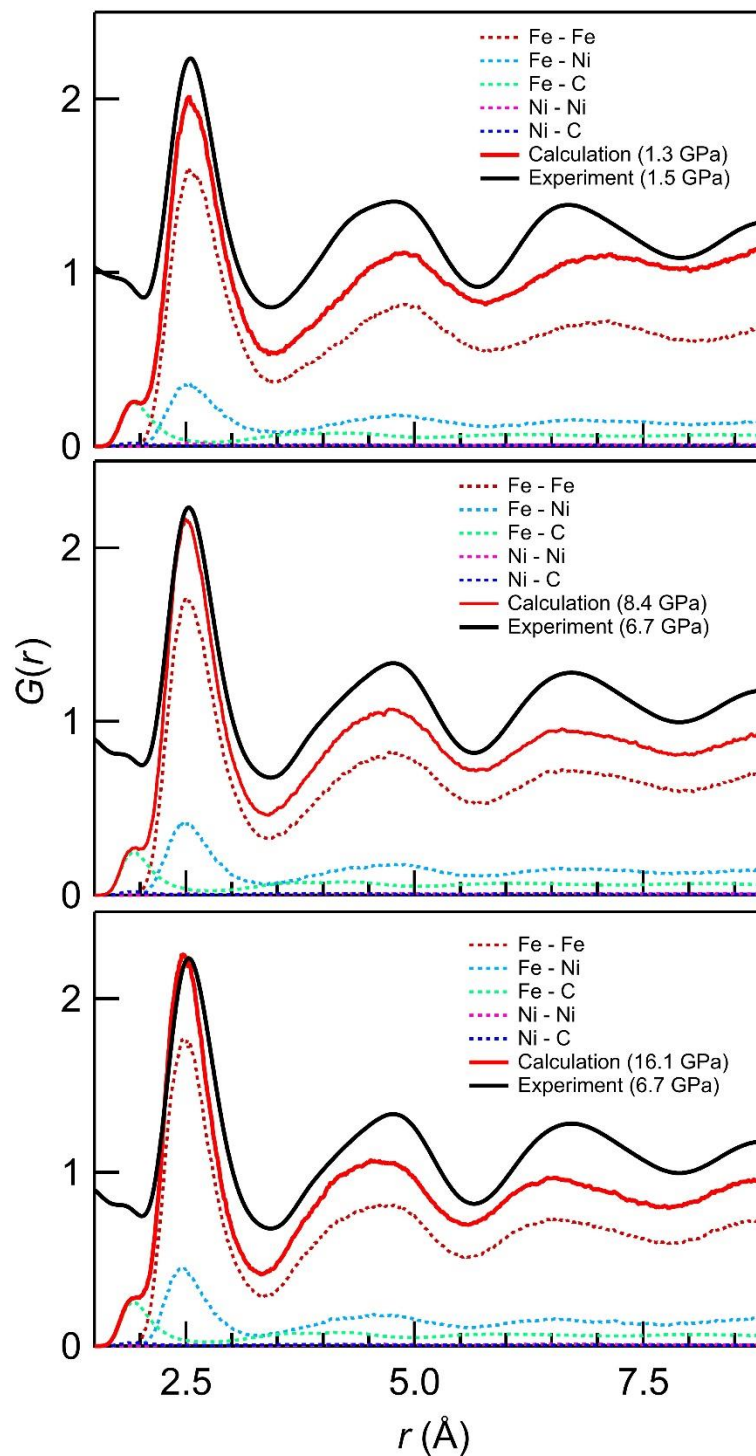


Figure 3.8. Computational total and partial RDFs of  $\text{Fe}_{91}\text{Ni}_9\text{-5wt.\% C}$  liquid. The RDFs are normalized by the scattering coefficients of corresponding pairs. Experimental results of  $\text{Fe}_{90}\text{Ni}_{10}\text{-5wt.\% C}$  at similar  $P$ - $T$  conditions were also appended for comparison.

Similar to our experimental results, the computed second NNs peaks in  $G(r)$  for the Fe-Ni-C liquid at 1.3, 8.4 and 16.1 GPa (at 1673 K) are asymmetric and may imply complex SROs of the second NNs (Figure 3.8). The splitting of the second NNs peaks appears to be intrinsic to the liquid structure, from which critical liquid structural information can be retrieved for better understanding the nature of the liquid structural transition at  $\sim 5$  GPa. The origin of the splitting of the second NNs peak has been computationally investigated for metallic glasses and liquids from the perspective of different connection schemes of atomic packing motifs (e.g. Ding et al., 2015). That is, four different schemes of coordination polyhedral connections with the shared atoms from 1 to 4 contribute to the complex features of the second NNs peak. The linked coordination polyhedra are corner-shared for the 1-atom scheme, edge-shared for 2-atom scheme, and face-shared for 3- and 4-atom schemes. The ideal positions of the second NNs peak of the four schemes are  $2r_1, \sqrt{3}r_1, \sqrt{8/3}r_1$  and  $\sqrt{2}r_1$ , respectively (Ding et al., 2015).

The atomic correlations contributing to the second NNs peaks in PDFs of the Fe-Ni-C liquids were evaluated using the connection schemes of Fe/Ni atomic packing motifs. Fe/Ni atomic packing motifs in the liquids are the polyhedra of the first Fe/Ni-Fe/Ni NNs with a coordination number (CN) ranging from 11.8 to 12.2 from ambient pressure to 8.4 GPa, which reflects the near optimal packing of hard spheres of Fe/Ni atoms. Figure 3.6 shows the calculated partial PDFs for the Fe/Ni-Fe/Ni pairs and the decomposed PDFs for the first NNs and second NNs via 1-atom, 2-atom, 3-atom and 4-atom coordination polyhedra connections at 1.3 and 8.4 GPa. The PDF peak for the 3-atom faced-shared connection appears to be stronger in intensity and thus markedly favored at higher pressure of 8.4 GPa, whereas those for other connection schemes, the intensities of the peaks became relatively weaker (Figure 3.9). The peak for the 3-atom scheme has lower  $r$  value, likely responsible for the marked reduction in the  $r_{2s}$  and  $r_{2m}$  values at  $>5$  GPa observed from our experiments (Figure 3.9).

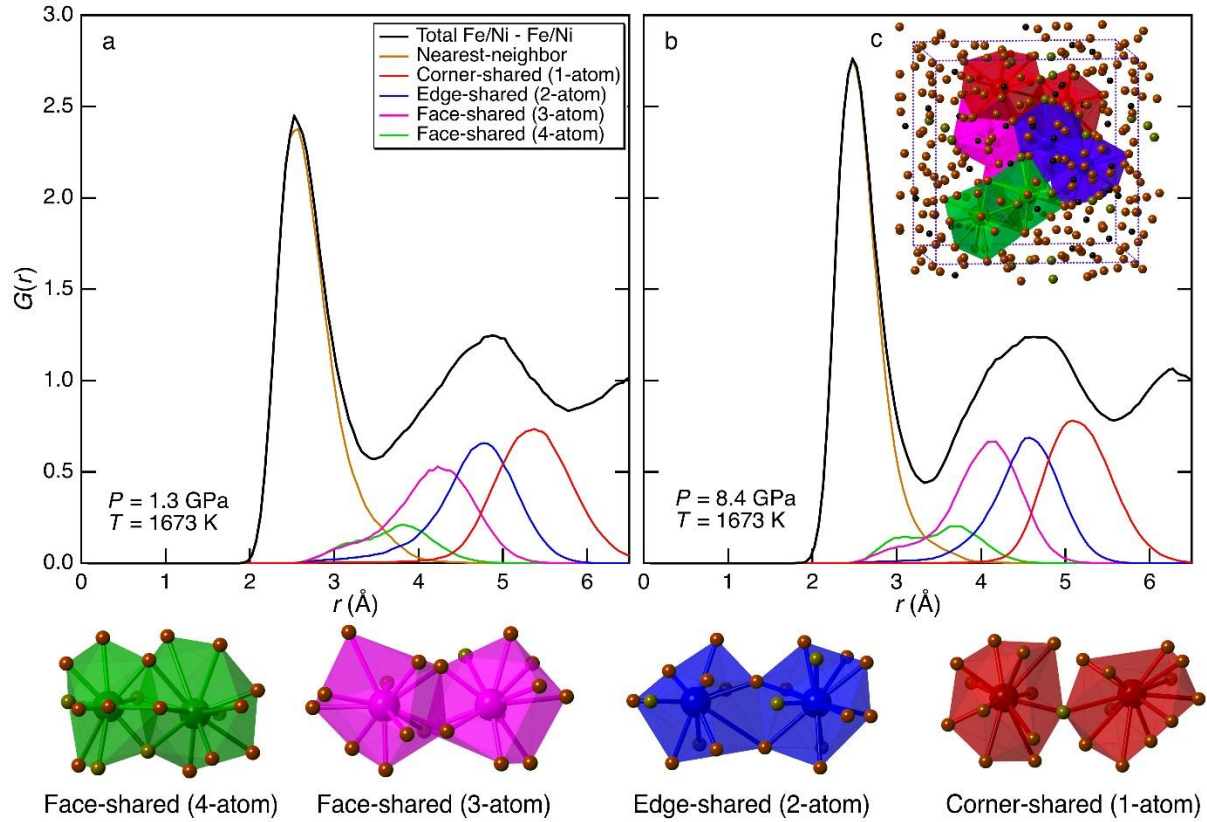


Figure 3.9. Total RDFs and decomposed RDF for the second coordination connection schemes at (a) 1.3 GPa, 1673 K and (b) at 8.4 GPa, 1673 K. (c) Inset: snapshot of MD simulations with the computational super cell highlighted in dashed lines. The highlighted polyhedra are 1-atom corner-shared (red), 2-atom edge-shared (blue), 3-atom face-shared (magenta), and 4-atom distorted face-shared (green) connections of Fe/Ni atom with their second nearest neighbors. Center atoms in the polyhedra are Fe/Ni atoms, with their sizes enlarged for clarity.

With the guides from the MD calculations, we further illustrated the spectral analyses of the experimentally determined  $G(r)$  within the framework of the connection schemes. The  $G(r)$  peaks of liquids are characteristically broader than those of metallic glasses, normally resulting from the vibrational thermal contributions by high temperatures in liquids. Figure 3.10 illustrates the representative spectra analyses of the FeNi<sub>3</sub>C liquid at 3.4 and 7.3 GPa. It is extremely difficult, if at all possible, to deconvolute the second NNs peak to 3 or 4 peaks of the liquids related to the four connection schemes (Ding et al., 2015). As shown in Figure 3.10, the ideal peak positions of the 2-atom and 3-atom schemes are close to each other, with 2-atom scheme at  $\sqrt{8/3} r_1$  and 3-atom scheme at  $\sqrt{3} r_1$ . At  $< 5 \text{ GPa}$ , as represented by the 3.4 GPa data, the fitted position of  $r_{2s}$  locates in between the ideal positions for the 2-atom and 3-atom schemes,

indicating that the fraction of the 3-atom peak is comparable to that of the 2-atom peak. However, at  $>5$  GPa, the fitted peak position of  $r_{2s}$ , as represented by the 7.3 GPa data, locates almost on top of the ideal position for the 3-atom scheme, implying an increased contribution from the 3-atom polyhedral connections compared to that from the 2-atom connections in the liquid, consistent with the theoretical results as demonstrated in Figure 3.9. Nevertheless, the observed splitting of the second NNs peaks in the PDFs infers the inherent structure of the liquids that could be characterized by the different connection schemes of atomic packing motifs and their relative fractions in the liquids.

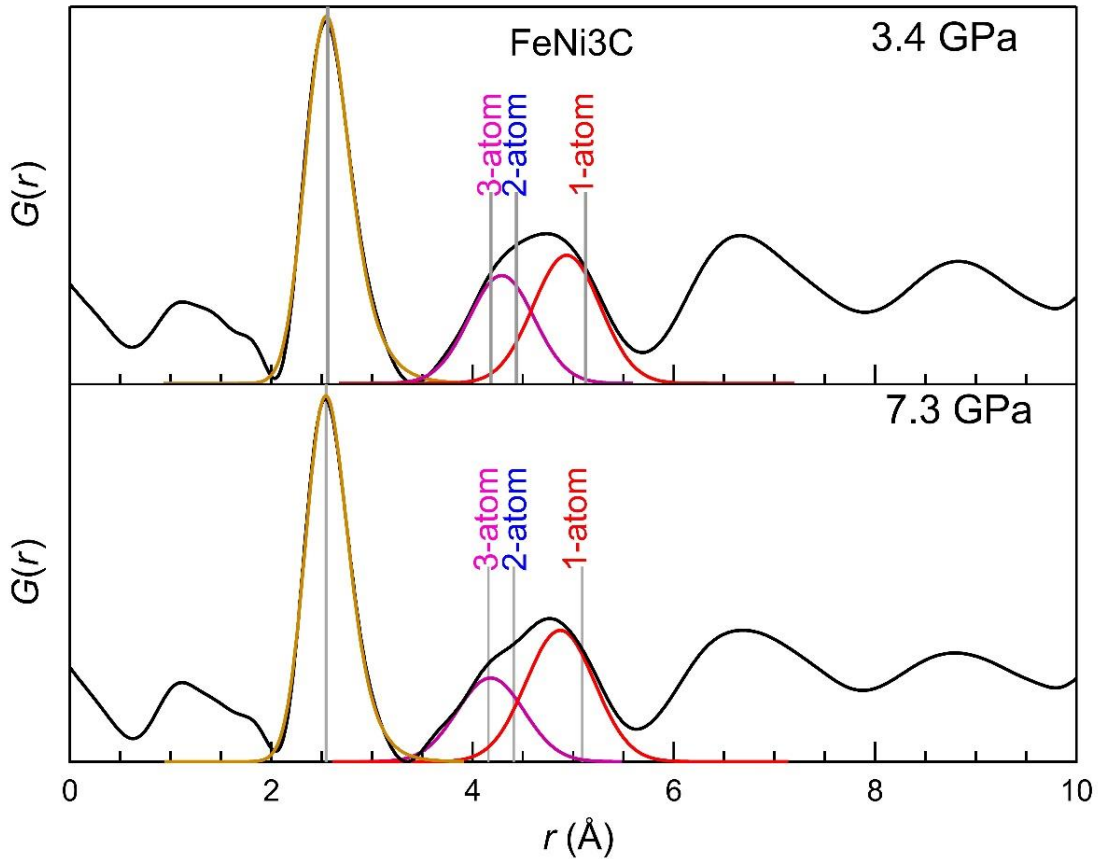


Figure 3.10. Representative experimentally-determined  $G(r)$  for FeNi<sub>3</sub>C liquid at 3.4 GPa and 7.3 GPa and fitting results of the first and second NNs peaks. The first NNs peak was fitted by the ExpModGaussian function (gold color) and the second NNs peak was fitted with two Gaussian peaks (dark magenta and blue color). The fitted  $r_1$  position and the derived ideal positions for 1-atom, 2-atom and 3-atom connection schemes were illustrated using grey vertical lines. See text for the detailed discussion.

The fitted positions of  $r_{2s}$  and  $r_{2m}$  plotted against  $r_1$  from our experimental data provide further support for the liquid structure and the inferred motif connection schemes changes at approximately 5 GPa (Figure 3.11). The  $r_{2m}$  data points are between the ideal positions for 1-atom and 2-atom connection schemes, but closer to those for the 1-atom connection scheme. Before the structural transition at around 5 GPa, the  $r_{2s}$  data points are between those for the 2-atom and 3-atom connection schemes. After the transition, both the  $r_{2m}/r_1$  and  $r_{2s}/r_1$  ratios drop noticeably. Particularly, the  $r_{2s}$  peak positions mostly fall towards the line for the 3-atom connection scheme at  $>5$  GPa. This is probably caused by the favoring of the 3-atom connection scheme after the liquid structural transition. As indicated by the computed partial PDFs in Figure 3.11, the  $r_{2s}$  peaks can be explained by the contributions mainly from the 3-atom face-shared connection scheme with its ideal position at  $\sqrt{8/3}r_1$  and partly from 4 atom face-shared and 2-atom edge-shared connection scheme. The favoring of the 3-atom connection scheme with relatively low ideal  $r$  values can thus cause the reduction in  $r_{2s}$  across the liquid structure transition.

Our MD simulations provide critical information on C-Fe/Ni and Fe/Ni-Fe/Ni coordination environments. The calculated average coordination number (CN) of first NNs for the C-Fe/Ni coordination continuously increases from  $\sim 6.5$  at ambient pressure to 7.0 at 8 GPa, 7.9 at 30 GPa, and 8.5 at 67 GPa, whereas the cut-off distance for the C-Fe/Ni coordination decreases from 2.81 to 2.76 Å, 2.73 Å, and 2.71 Å at respective pressures. Our calculated partial CN of the Fe/Ni-Fe/Ni second NNs with 3-atom connections increases prominently from  $\sim 8.5$  at 1.3 GPa to  $\sim 10.0$  at 8.4 GPa across the structural transition, whereas the calculated partial CNs of other connection schemes of the second NNs decreased slightly in the pressure range studied. The calculated total CNs for the Fe/Ni-Fe/Ni coordination have an initial increase from 11.8 to 12.2 across the liquid structural transition, but remain almost constant at 12.2 at 5-67 GPa. A previous study suggested that regions with Fe<sub>3</sub>C-like structure (a deformed epsilon( $\epsilon$ )-Fe lattice) exist in the Fe-C liquids when the carbon concentration is higher than 3 wt.% at ambient condition (Sobolev and Mirzoev, 2013). As revealed by our MD calculations, the C-Fe/Ni polyhedra are also found in the liquid structure and they become severely distorted as compared to crystal Fe<sub>3</sub>C structure at high pressure (Figure 3.12).

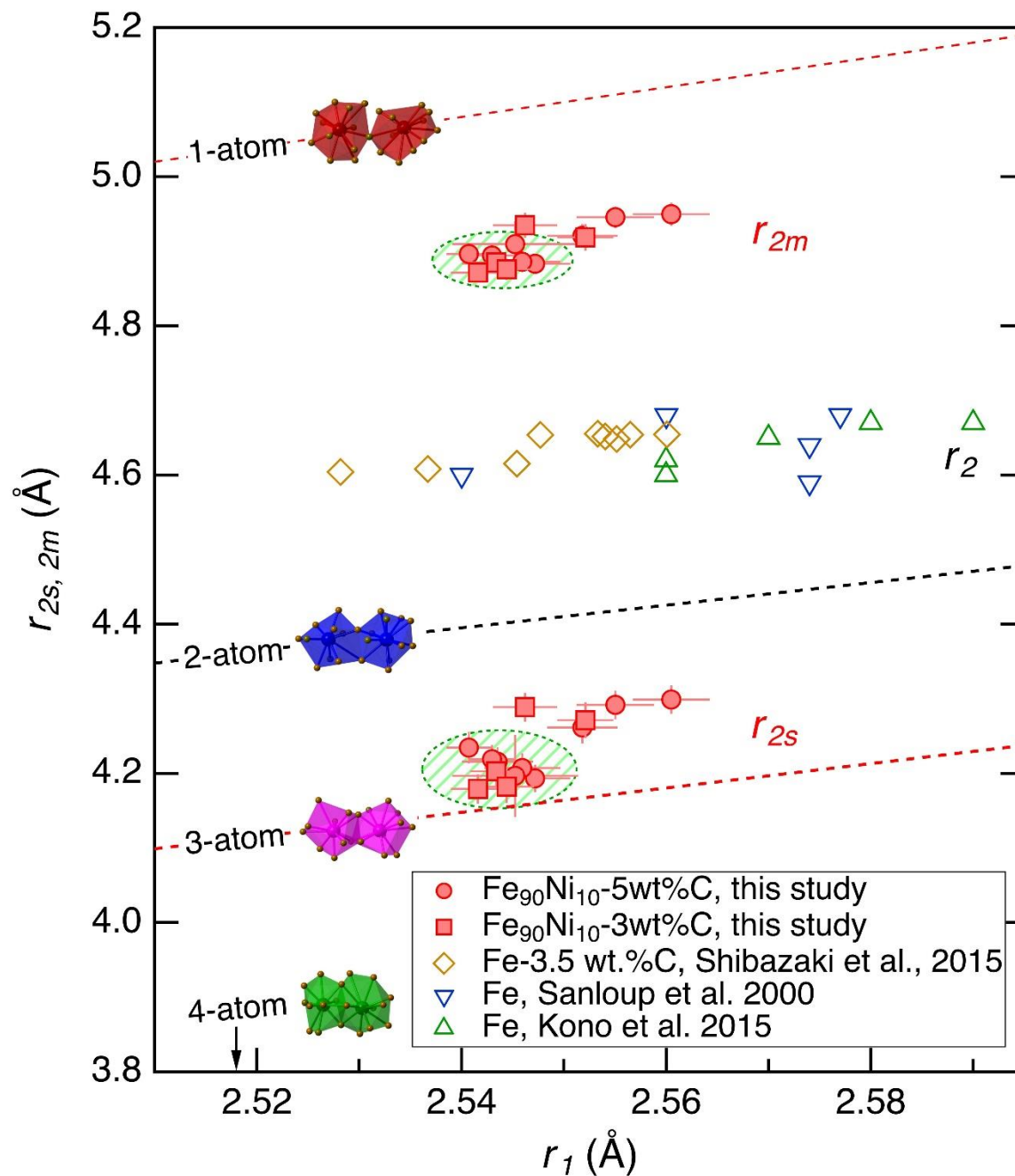


Figure 3.11. Peak positions  $r_{2s}$  and  $r_{2m}$  as a function of  $r_1$ . Solid symbols are peak fitting results from this study and open symbols are peak fitting results from previous studies (Kono et al., 2015; Sanloup et al., 2000; Shibazaki et al., 2015). Dashed lines represent the ideal positions for 1-atom, 2-atom, 3-atom and 4-atom motif connections. The data in the green shaded areas represent the high-pressure liquid phase  $>5$  GPa.

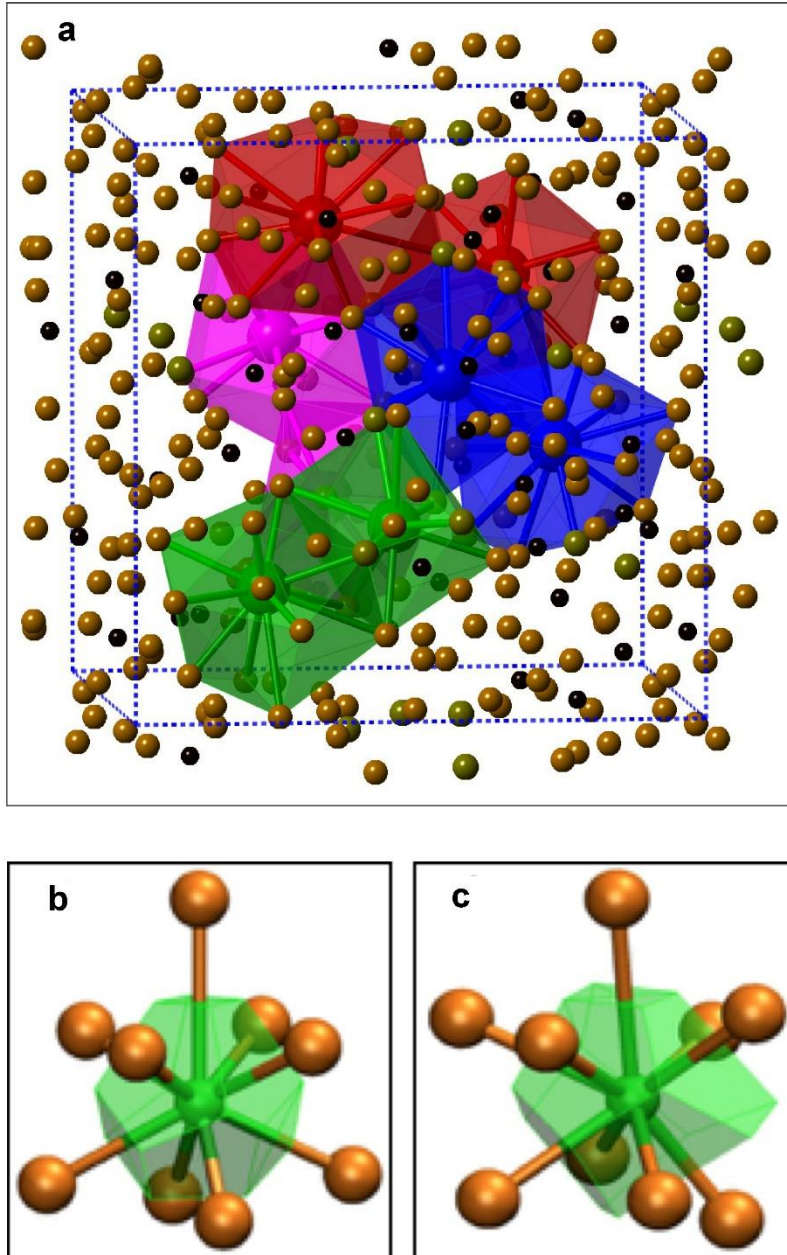


Figure 3.12. Structure information of  $\text{Fe}_{91}\text{Ni}_9$ -5wt.% C liquid and  $\text{Fe}_3\text{C}$  from first-principles molecular dynamics simulations. (a) Snapshot of MD simulations with the computational super cell highlighted in dashed lines. The highlighted polyhedra are 1-atom corner-shared (red), 2-atom edge-shared (blue), 3-atom face-shared (magenta), and 4-atom distorted face-shared (green) connections of Fe/Ni – Fe/Ni pair with their second nearest neighbors. Center atoms in the polyhedra are Fe/Ni atoms, with their sizes enlarged for clarity. Fe: brown, Ni: olive, C: black. (b) Carbon coordination environment of crystalline  $\text{Fe}_3\text{C}$ . (c) Carbon coordination environment of  $\text{Fe}_{91}\text{Ni}_9$ -5wt.% C liquid at 5.1 GPa, 1673 K, the center atoms are carbon. In B, C, green polyhedral are the Voronoi polyhedral of the center carbon.

### 3.5 Discussion and geophysical implications

The viscoelastic properties, such as the density, sound velocity, and viscosity of the Fe-Ni-C liquids may be affected by the observed structural change at ~5 GPa. Indeed, recognizable compressibility behavior anomalies reported for liquids Fe-5.7 wt.% C (Sanloup et al., 2011), Fe-6.7 wt.% C (Terasaki et al., 2010) and Fe-3.5wt.% C (Shimoyama et al., 2013) at ~5 GPa can be readily explained by the liquid structure transition. Measurements for viscosity (Terasaki et al., 2006) and sound velocity (Kuwabara et al., 2016; Shimoyama et al., 2016) for Fe-(Ni)-C liquids are limited to <5 GPa or extremely sparse, and the effect of structural transition on these properties remains unclear. On the analogy of metallic glass systems in which clusters with 3-atom connections are stiffer than the 2-atom and 4-atom counterparts (Ding et al., 2015), higher viscosity is anticipated for the Fe-Ni-C liquids with higher fraction of 3-atom connections above ~5 GPa.

The understanding of the structural evolution of metallic liquids upon pressure is essential for modeling the structure and dynamics of terrestrial planets and moons with relatively low core-mantle boundary pressures of ~5-8 GPa, such as the Moon, Mercury, Ganymede, and Europa (Chen et al., 2008; Dasgupta et al., 2009; Garcia et al., 2011; Hauck et al., 2013). For larger terrestrial planets such as Mars, Venus, and the Earth, the extrapolation of liquid properties measured at low to moderate pressures needs to be performed with extreme caution and structural evolution of Fe-rich liquids needs to be considered so as to construct realistic and reliable geophysical models for the outer cores.

Liquid structure and pressure-induced polyamorphic transitions of the Fe-Ni-C liquids, as revealed by the cooperation between experiments and calculation, may have important implications into the physicochemical evolution of terrestrial planets and moons. The distinct isotopic compositions of bulk silicate Earth (BSE) in comparison with other terrestrial planets or planetesimals (i.e., Vesta and Mars) and primitive undifferentiated meteorites (chondrites) may own their origin to the metal-silicate differentiation during the core formation. Earth, Mars and Vesta have all undergone core formation and therefore should exhibit similar isotopic signatures. However, many mantle-derived rocks of the Earth have relative enrichments of heavy carbon and Fe isotopes, related to Mars, Vesta and primitive undifferentiated meteorites (chondrites) (Poitrasson et al., 2004; Polyakov, 2009; Wood et al., 2013). The metal-silicate equilibration under different physicochemical conditions that prevailed during core formation could have left

behind distinct geochemical signatures in the silicate mantles; the pressure at the bottom of deep magma ocean in proto-Earth is likely ~50-60 GPa whereas the pressure is likely <5 GPa for smaller terrestrial planets, moons, and planetary bodies such as Mars and Vesta (Wood et al., 2013). The equilibration might have taken place between the high-pressure forms of liquid Fe-rich metals such as the Fe-Ni-C liquids and mantle-forming silicates for the Earth. The low-pressure forms of metallic liquids might have been involved in the metal-silicate separation in Vesta and Mars. Our calculated results for the C-Fe/Ni coordination show that the high-pressure liquid phase has a CN of ~7.0 at 8 GPa, an ~8% increased from 6.5 for the low-pressure liquid phase, while the C-Fe cut-off distance decreases by ~2% from 0 to 8 GPa. For the Fe/Ni-Fe/Ni coordination, the CN increases from 11.8 to 12.2 (~3%) from ambient pressure to 8.4 GPa, while cut-off distance decrease from 3.49 Å to 3.42 Å (~2%). Schauble (2004) noted that generally lighter stable isotopes preferentially occupy the higher coordinated sites with long and weaker bonds and heavier isotopes prefer lower coordinated sites with short and stronger bonds. The profound changes in CNs of both C-Fe/Ni and Fe/Ni-Fe/Ni coordination environments enhanced by the polyamorphic transition at 5 GPa may lead to intriguing isotope signatures in core-forming and mantle-forming materials in terrestrial bodies. Compared to the low-pressure Fe-Ni-C liquid phase, the high-pressure liquid phase with higher Fe-C and Fe-Fe coordination, involved in the formation of the Earth's core, is able to preferentially sequester lighter Fe or C isotopes into the core. Distinct geochemical traces in the BSE may have been rendered by the pressure-induced structural change of the core-forming metals during formation of planetary cores. Liquid structure and onset of pressure-induced structural change depend on the species and concentrations of light elements in liquid Fe. Further investigations are thus needed to understand the structural evolution and determine the viscoelastic properties of Fe liquids alloyed with other light elements at high pressures.

### 3.6 Conclusions

The cooperation between experiments and computations has provided critical information on the structural evolution of the Fe-Ni-C liquids with pressure. X-ray diffraction measurements on FeNi5C and FeNi3C liquids have been conducted in a Paris-Edinburgh press up to 7.3 GPa. The notable changes of the rich features of the second NNs peaks in the derived PDFs were used as primary indication of a polyamorphic liquid structural transition at ~5 GPa for both liquids.

The changes are manifested as notable reduction in peak positions of the subpeaks of the second NNs at around 5 GPa for both the liquids. The structural evolution of the liquids upon compression was further investigated by the first-principles MD calculations. We found that the liquid structural transition is due to the notable favoring of the 3-atom polyhedra connections of Fe-Ni atomic motifs in the high-pressure liquids at >5 GPa, in comparison to the low-pressure counterpart. The computed CNs for the Fe/Ni-Fe/Ni coordination environment show a slight increase up to 5 GPa and become almost constant at 5-67 GPa. In contrast, the computed CNs for the C-Fe/Ni coordination environment exhibit a significant increase from 6.5 at ambient pressure to 8.5 at 67 GPa. The structural evolution of liquid Fe alloys upon compression, as exemplified by the Fe-Ni-C liquids in this study, may have significant effect on the liquid properties, such as viscosity, sound velocity, and density. The liquid structure change may also influence the partitioning behaviors of major or trace elements and isotopic fractionation between metal and silicates during planetary core formations. As such, our findings may provide unique insights into the core formation processes that set the Earth apart from other planets or planet-forming bodies, particularly in terms of geochemical signatures. The distinct geochemical imprints (i.e., Fe and C isotopes) left behind by the formation of the Earth's core, in comparison with other terrestrial planets or planetary bodies (i.e., Mars and Vesta) and primitive undifferentiated meteorites (chondrites), may own their origins to the liquid structural change. The knowledge of the polyamorphic transitions in core-forming liquid Fe alloys is thus crucial for our understanding of the chemical evolution of terrestrial planets and moons.

### **3.7 Acknowledgments**

Supporting data are available in Table 3.1. This work was performed at HPCAT (Sector 16), APS, ANL. HPCAT operation is supported by DOE-NNSA under Award No. DE-NA0001974, with partial instrumentation funding by NSF. The Advanced Photon Source is a U.S. Department of Energy (DOE) Office of Science User Facility operated for the DOE Office of Science by Argonne National Laboratory under Contract No. DE-AC02-06CH11357. This work was supported by NSF grants (EAR-1555388 and EAR-1565708) to BC. Computational work was support by NSF grant (EAR-1565678) to JW. This research used resources of the National Energy Research Scientific Computing Center, a DOE Office of Science User Facility supported by the Office of Science of the U.S. Department of Energy under Contract No. DE-AC02-

05CH11231. Portions of this research were conducted with high performance computing resources provided by Louisiana State University (<http://www.hpc.lsu.edu>). X. L. thanks the support from Bullard award, University of Hawai‘i at Mānoa. Y.K. acknowledges the support of DOE-BES/DMSE under Award DE-FG02-99ER45775.

## Chapter 4

# Thermoelastic Properties of Fe<sub>7</sub>C<sub>3</sub> at High Pressures by Single-Crystal X-Ray Diffraction

*This chapter has been published as Xiaojing Lai, Feng Zhu, Jiachao Liu, Dongzhou Zhang, Yi Hu, Gregory Finkelstein, Przemyslaw Dera, and Bin Chen (2018). The high-pressure anisotropic thermoelastic properties of a potential inner core carbon-bearing phase, Fe<sub>7</sub>C<sub>3</sub>, by single-crystal X-ray diffraction. American Mineralogist, 103(10), 1568-1574.*

### 4.1 Abstract

Carbon has been suggested as one of the light elements existing in the Earth's core. Under core conditions, iron carbide Fe<sub>7</sub>C<sub>3</sub> is likely the first phase to solidify from an Fe-C melt and has thus been considered a potential component of the inner core. The crystal structure of Fe<sub>7</sub>C<sub>3</sub>, however, is still under debate, and its thermoelastic properties are not well constrained at high pressures. In this study, we performed synchrotron-based single-crystal X-ray diffraction experiment using an externally-heated diamond anvil cell to determine the crystal structure and thermoelastic properties of Fe<sub>7</sub>C<sub>3</sub> up to 80 GPa and 800K. Our diffraction data indicate that Fe<sub>7</sub>C<sub>3</sub> adopts an orthorhombic structure under experimentally investigated conditions. The pressure-volume-temperature data for Fe<sub>7</sub>C<sub>3</sub> were fitted by the high-temperature Birch-Murnaghan equation of state, yielding ambient-pressure unit cell volume  $V_0 = 745.2(2) \text{ \AA}^3$ , bulk modulus  $K_0 = 167(4) \text{ GPa}$ , its first pressure derivative  $K_0' = 5.0(2)$ ,  $dK/dT = -0.02(1) \text{ GPa/K}$ , and thermal expansion relation  $\alpha_T = 4.7(9) \times 10^{-5} + 3(5) \times 10^{-8} \times (T-300) \text{ K}^{-1}$ . We also observed an anisotropic elastic response to changes in pressure and temperature along the different crystallographic directions. Fe<sub>7</sub>C<sub>3</sub> has strong anisotropic compressibilities with the linear moduli  $M_a > M_c > M_b$  from zero pressure to core pressures at 300K, rendering the  $b$  axis the most compressible upon compression. The thermal expansion of  $c^3$  is approximately four times larger than that of  $a^3$  and  $b^3$  at 600K and 700K, implying that the high temperature may significantly influence the elastic anisotropy of

$\text{Fe}_7\text{C}_3$ . Therefore, the effect of high temperature needs to be considered when using  $\text{Fe}_7\text{C}_3$  to explain the anisotropy of the Earth's inner core.

*Key words* : iron carbide, thermal equation of state, anisotropy, inner core, temperature effect

## 4.2 Introduction

Earth's inner core is considered to consist primarily of iron alloyed with nickel and one or more light elements e.g. sulfur, silicon, oxygen, hydrogen and carbon, as informed by numerous geophysical and geochemical constraints (recently reviewed by Hirose et al., 2013; Li and Fei, 2014; Litasov and Shatskiy, 2016). The Fe-C system has been proposed as a candidate composition for the Earth's core largely due to the high cosmochemical abundance of carbon, the frequent occurrence of iron carbide phases in meteorites, and the high solubility of carbon in Fe-Ni liquids under the core-mantle differentiation conditions (Wood, 1993). If the liquid core contained carbon, the iron carbide phase,  $\text{Fe}_7\text{C}_3$ , may be the first phase to crystallize from the iron-carbon melt under core conditions rather than other iron carbide phases such as  $\text{Fe}_3\text{C}$ , as suggested by previously published Fe-C phase diagrams (Fei and Brosh, 2014; Lord et al., 2009; Nakajima et al., 2009). The extrapolated density and sound velocity of  $\text{Fe}_7\text{C}_3$  may account for the density deficit and low S-wave velocity ( $v_s$ ) of the inner core (Chen et al., 2012; Chen et al., 2014; Liu et al., 2016b; Nakajima et al., 2011). In addition, its high Poisson's ratio at inner core conditions was suggested to be comparable to that of the inner core (Prescher et al., 2015). Moreover, the melting experiments by Liu et al. (2016c) suggested that  $\text{Fe}_7\text{C}_3$  may be a constituent of the innermost inner core for carbon-bearing core composition due to its high melting temperature.

The crystal structure of  $\text{Fe}_7\text{C}_3$  has remained controversial over the last few decades. Previous experimental studies reported its structure as either hexagonal ( $P6_3mc$ ) (Herbstein and Snyman, 1964) or orthorhombic ( $Pnma$ ,  $Pmn2_1$ ,  $Pmc2_1$ ,  $Pmcn$  or  $Pbca$ ) (Barinov et al., 2010; Bouchard, 1967; Fruchart et al., 1965; Prescher et al., 2015). Theoretical calculations also compared the stability of hexagonal and orthorhombic phases. Fang et al. (2009) determined that the orthorhombic phase ( $Pnma$ ) is more stable than the hexagonal phase ( $P6_3mc$ ), whereas Raza et al. (2015) calculated that the orthorhombic phase (space group  $Pbca$ ) is the stable phase below 100 GPa and the hexagonal phase becomes more stable above 100 GPa.

The elastic constants of  $\text{Fe}_7\text{C}_3$  were also calculated at 0K for the two crystal structures with space groups of  $P6_3mc$  and  $Pbca$  (Mookherjee et al., 2011; Raza et al., 2015). There has been, however, only one study that calculated the thermoelasticity of  $\text{Fe}_7\text{C}_3$  with the space group of  $P6_3mc$  (Li et al., 2016). Most of the high-pressure experimental studies of the density of  $\text{Fe}_7\text{C}_3$  were performed at room temperature. The thermal equation of state (EoS) parameters have only been determined below 30 GPa (Litasov et al., 2015; Nakajima et al., 2011), which leads to a large uncertainty when extrapolating the experimental data to the pressure and temperature ( $P$ - $T$ ) conditions of the inner core. Accurate knowledge on the crystal structure and thermoelastic properties of  $\text{Fe}_7\text{C}_3$  under core conditions is needed to construct a comprehensive and seismologically consistent Fe-C inner core compositional model.

For the inner core, seismic waves travel faster along the rotational axis than in the equatorial plane; one possible explanation for this anisotropy is the presence of preferentially-orientated iron with strong single-crystal elastic anisotropy in the Earth's inner core (Deuss, 2014; Hirose et al., 2013). The alloying of light elements with iron often leads to different crystal structure and elasticity (Litasov and Shatskiy, 2016). Thus, quantification of the elastic anisotropy of iron alloys is essential for us to understand the inner-core anisotropy. For *hcp* metals and isostructural iron alloys such as Fe-Ni-Si system, the elastic anisotropy is related to the  $c/a$  ratio, that is, the compressibilities and thermal expansion of the  $a$  and  $c$  unit cell parameters under high pressure and high temperature (Fischer and Campbell, 2015; Steinle-Neumann et al., 2001; Wenk et al., 1988). For orthorhombic  $\text{Fe}_7\text{C}_3$ , the elastic anisotropy is also correlated with the different compressional response to applied pressure of each primary crystallographic axis as reported in a calculation by Raza et al. (2015). Therefore, it is crucial to constrain how the compressibility and thermal expansion along individual crystallographic axes respond to pressure and temperature, so as to understand the potential for this material to contribute to the seismic anisotropy observed in the inner core (Deuss, 2014). In this study, we determined the thermal EoS and the thermoelastic properties of  $\text{Fe}_7\text{C}_3$  along different crystallographic axes up to 80 GPa and 800K by employing an externally-heated diamond anvil cell with synchrotron-based single-crystal X-ray diffraction.

### 4.3 Methods

The  $\text{Fe}_7\text{C}_3$  single crystal sample was synthesized at 18 GPa and 1773 K in a multi-anvil press (Prescher et al., 2015). Single-crystal XRD characterizations of the sample at ambient conditions were conducted at beamline 13-BMC, APS, ANL and at the University of Hawai'i at Mānoa using a Bruker D8 Venture single-crystal diffractometer ( $\lambda = 0.5609 \text{ \AA}$ ). The sample was mounted on a MiTeGen micromesh that was attached to a goniometer head. At beamline 13-BMC, the sample was rotated from  $-60^\circ$  to  $+60^\circ$ .  $120^\circ$  wide-angle exposure and  $1^\circ$  step exposures were collected. For the ambient characterization of the sample at UHM, a preliminary matrix run was first completed with  $1^\circ$  steps through orthogonal slices of reciprocal space. Indexing of diffraction peaks from the matrix run was used by Bruker APEX 3 software to determine an optimal data collection strategy that ensured 100% completeness to a resolution limit of  $0.65 \text{ \AA}$ . This strategy was then used to collect a full dataset.

A BX90 DAC with a pair of  $250 \mu\text{m}$ -culet diamond anvils was used for the high-pressure XRD experiments (Kantor et al., 2012). A cubic boron nitride seat on the upstream side and a large-opening tungsten carbide seat on the downstream side were used to maximize access to reciprocal space for the single-crystal XRD measurements. A pyrophyllite ring-heater base was fabricated using a milling machine and sintered in a furnace at 1373 K for 20 hours. Three Pt-10wt.%Rh (0.01") wires were wound around the heater base and covered by high-temperature cement. Two K-type thermocouples (Chromega-Alomega 0.005" and Chromega-Alomega 0.010") were mounted near the diamond culet and in touch with the downstream diamond to measure the temperature. The rhenium gasket was pre-indented to a thickness of  $\sim 35 \mu\text{m}$  and a sample chamber of  $150 \mu\text{m}$  in diameter was drilled by an electrical discharge machine (EDM). A  $10 \mu\text{m}$  thick  $\text{Fe}_7\text{C}_3$  single-crystal grain and two pressure calibrants, a small ruby sphere (Mao et al., 1986) for the neon gas loading and a piece of gold foil near the sample as the primary pressure scale in experiments (Fei et al., 2007), were loaded in the sample chamber. Neon gas, which was used as a pressure-transmitting medium, was loaded in the sample chamber using the gas loading machine at GeoSoilEnviroCARS of the APS. The pressure uncertainties were estimated by the pressure difference of gold and neon (Fei et al., 2007).

The high-pressure and high-temperature synchrotron-based single-crystal XRD experiments were conducted at beamline 13-BMC, APS, Argonne National Lab. The typical size of the focused monochromatic X-ray beam ( $\lambda = 0.4340 \text{ \AA}$ ) was  $16 \times 11 \mu\text{m}^2$ . A MAR165 charged

coupled device (CCD) detector was used to collect the diffraction patterns. The X-ray accessible opening angle of the DAC was  $\pm 20^\circ$ . The rotation axis for the single-crystal diffraction experiment was placed horizontally, perpendicular to the incident X-ray beam. A series of  $10^\circ$  wide-angle exposures and  $1^\circ$  step exposures from  $-20^\circ$  and  $20^\circ$  were collected at four different detector positions for each pressure and temperature point. The investigated range of pressure was 1 bar to 79.2 GPa and range of the temperature was 300K to 800K (Figure 4.1).

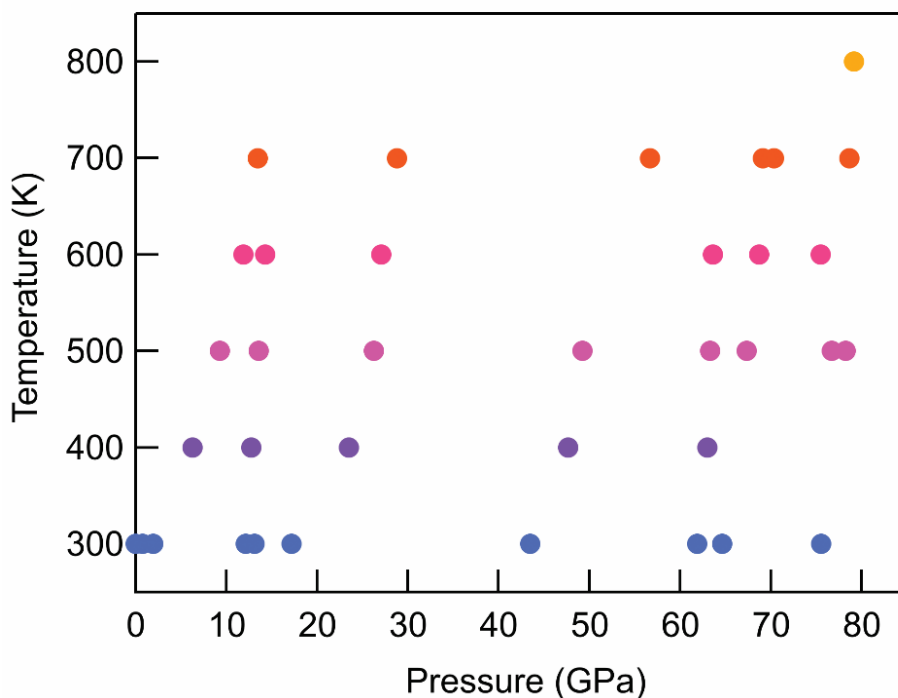


Figure 4.1. *P-T* coverage of the XRD experiments of Fe<sub>7</sub>C<sub>3</sub> in the diamond anvil cell.

To analyze the synchrotron-based single crystal XRD data, we utilized the ATREX software package for peak fitting and intensity corrections (Dera et al., 2013). The unit cell and orientation matrix were determined by the CELL\_NOW software (Bruker AXS Inc.). Lattice parameters were refined by least-squares fitting in the RSV software (Dera et al., 2013). The structure refinement was performed using SHELXL (Sheldrick, 2008). The ambient pressure data collected at UHM were analyzed using the Bruker APEX 3 software package to solve the complexity in the crystal structure. The *P-V-T* data and *P-x* (i.e. *a/b/c* axes) were fitted by the EosFit7-GUI program (Gonzalez-Platas et al., 2016).

## 4.4 Results and discussion

### 4.4.1 The crystal structure of $\text{Fe}_7\text{C}_3$ at room pressure and temperature

The indexing of single-crystal XRD patterns of  $\text{Fe}_7\text{C}_3$  at ambient conditions indicates an orthorhombic lattice with space group  $Pbca$  ( $Z = 8$ ), and with unit-cell parameters of  $a = 11.979(1)$  Å,  $b = 4.5191(8)$  Å and  $c = 13.767(2)$  Å. However, the ambient data indicate some structural complexity beyond the simple ideal structure described previously (Prescher et al., 2015), and consistently present in all of the several single crystal specimens that we have examined. This non-ideality involves the presence of twin micro-domains, but seems to also include structural modulation.

The presence of peaks that could not be indexed using a single orientation matrix to the initially indexed domain indicates a likely twinned crystal structure (Figure 4.2). The second domain is significantly weaker than the first. A total of 1651 peaks from the dominant domain were utilized to refine the crystal structure (Figure 4.3), which is generally consistent with that reported by Prescher *et al.* (2015). In the  $Pbca$  structure, three distorted  $\text{CFe}_6$  trigonal prisms form triads by sharing corners. The triads are stacked parallel to the  $b$  axis to form a column. Each stack is rotated  $\sim 60^\circ$  relative to its neighbors. Columns are oriented inversely along the  $b$  axis compared to their neighbor columns. Columns with the same direction are edge sharing and columns with the opposite direction are corner sharing (Figure 4.3).

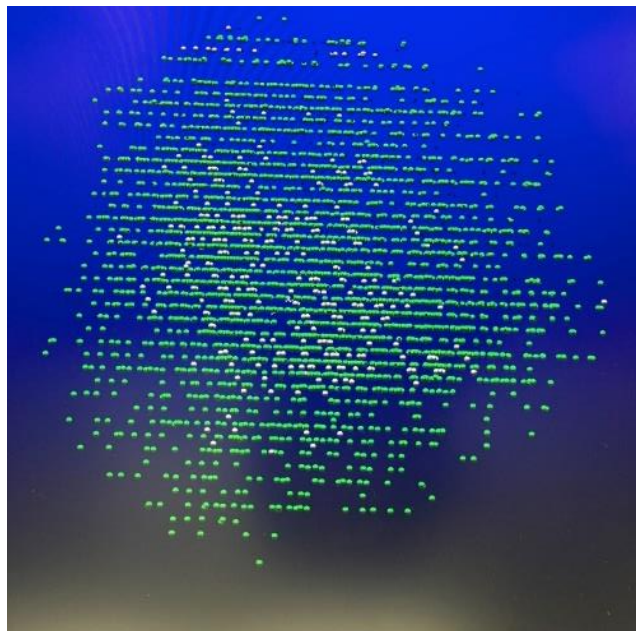


Figure 4.2. All the peaks harvested from single-crystal XRD measurements of  $\text{Fe}_7\text{C}_3$  at UHM. The green peaks were used for indexing and refinement of the crystal structure at ambient conditions and may correspond to a dominant twin domain (as described in the main text). The white peaks are unique to the secondary twin domain. This corresponds to a  $180^\circ$  rotation around the  $[-1\ 0\ 2]$  axis.

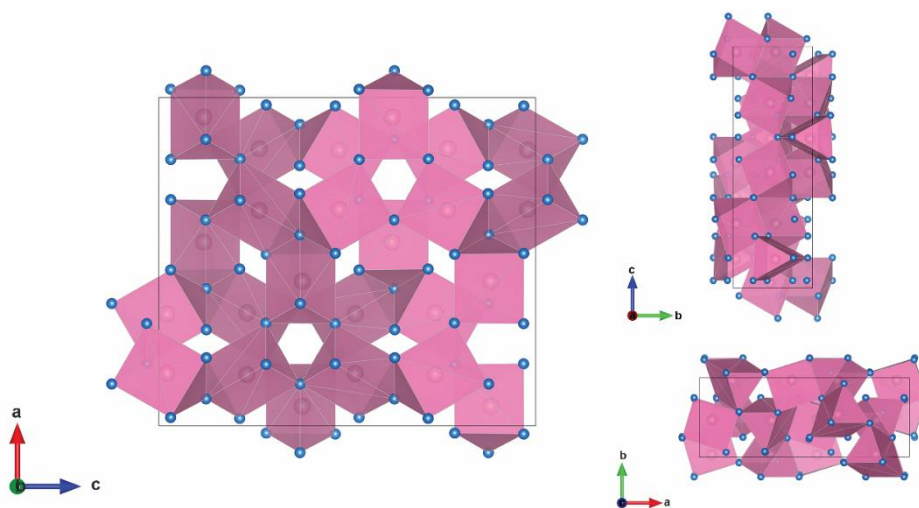


Figure 4.3. Crystal structure of  $\text{Fe}_7\text{C}_3$  projected along the  $b$  axis (left), the  $a$  axis (upper right) and the  $c$  axis (lower right) at ambient conditions (space group  $Pbca$ ,  $Z = 8$ ). Blue balls represent Fe. One carbon (pink) is located in the center of each  $\text{CFe}_6$  trigonal prism colored in pink.

The quality of structural refinement was high ( $R_{\text{int}} = 7.26\%$  and  $R_1 = 4.97\%$ ), however, we noted some artifacts that may be related to the twinning and/or the additional disorder within the structure. Three noticeably large peaks appeared in the difference Fourier map with heights above  $2.5 \text{ e}/\text{\AA}^3$ , located about  $0.8 \text{ \AA}$  from carbon atoms, and  $1.6 \text{ \AA}$  from closest Fe atoms. We attempted to reduce the symmetry to allowed orthorhombic and monoclinic subgroups of *Pbca* but could not find an alternative space group that would better account for this difference electron density. We also noted that the residual electron density reported by Prescher et al. (2015) was also quite high ( $2.022 \text{ e}/\text{\AA}^3$ ), which may indicate similar structural complexity in their samples. Proper refinement of such complexity in the structure may require a description using a 4-dimensional space group and the introduction of an extra basis vector or modulation vector. Additional ambient pressure experiments at varied temperatures are needed to confirm the likelihood of the modulation and whether the modulation is commensurate or incommensurate. Detailed crystallographic studies will be required to determine the exact origin of this difference electron density, but this is out of the scope for the present study which is primarily focused on the thermoelastic behaviors.

#### 4.4.2 Thermal equation of state of $\text{Fe}_7\text{C}_3$

The unit cell volumes of  $\text{Fe}_7\text{C}_3$  along various isotherms from 300K to 800K were determined by synchrotron-based single-crystal XRD measurements up to 79.2 GPa (Figure 4.4, Figure 4.5 and Table 4.1). No discontinuous crystal-structure change was observed over the entire pressure and temperature range. The room temperature  $P$ - $V$  data were fitted by the third-order Birch-Murnaghan Equation of State (B-M):

$$P = \frac{3}{2}K_{T_0} \left[ \left( \frac{V_{T_0}}{V} \right)^{\frac{7}{3}} - \left( \frac{V_{T_0}}{V} \right)^{\frac{5}{3}} \right] * \left\{ 1 + \frac{3}{2}(K_{T_0}' - 4) \left[ \left( \frac{V_{T_0}}{V} \right)^{\frac{2}{3}} - 1 \right] \right\} \quad (1)$$

where  $K_{T_0}$ ,  $K_{T_0}'$  and  $V_{T_0}$  are the isothermal bulk modulus, its first pressure derivative and the unit cell volume at ambient pressure and given temperature  $T$ , respectively. The 10  $P$ - $V$  data were weighted by the uncertainties in both pressure and volume and fitted by the third-order B-M EoS with  $K_0 = 165(4) \text{ GPa}$ ,  $K_0' = 5.1(2)$  and  $V_0 = 745.3(2) \text{ \AA}^3$  ( $K_0$ ,  $K_0'$  and  $V_0$  are for  $T = 300\text{K}$ ). Normalized stress ( $F_E$ ) as a function of the Eulerian finite strain ( $f_E$ ) is also plotted as an inset of Figure 4.5, where  $f_E = [(V/V_0)^{-2/3} - 1]/2$  and  $F_E = P/[3f_E(1+2f_E)^{5/2}]$  and the EoS can be simplified as  $F_E = K_0 + 3K_0/2(K_0' - 4)f_E$ , neglecting the high order terms (Angel, 2000). The  $f$ - $F$  plot can be used

to verify which order of the B-M EoS is sufficient to satisfactorily represent the compression behavior of the sample (Angel, 2000). The quasi-linear  $f$ - $F$  relationship suggests the adequacy of using the third-order B-M EoS and its positive slope indicates  $K_0' > 4$  (Figure 4.5 inset). Previous studies reported that the slope of the  $f$ - $F$  plot changed abruptly as a result of the magnetic transitions of hexagonal  $\text{Fe}_7\text{C}_3$  (Chen et al., 2012; Liu et al., 2016b), but we did not observe this, potentially due to the sparsity of our data at 300K (Figure 4.5 inset).

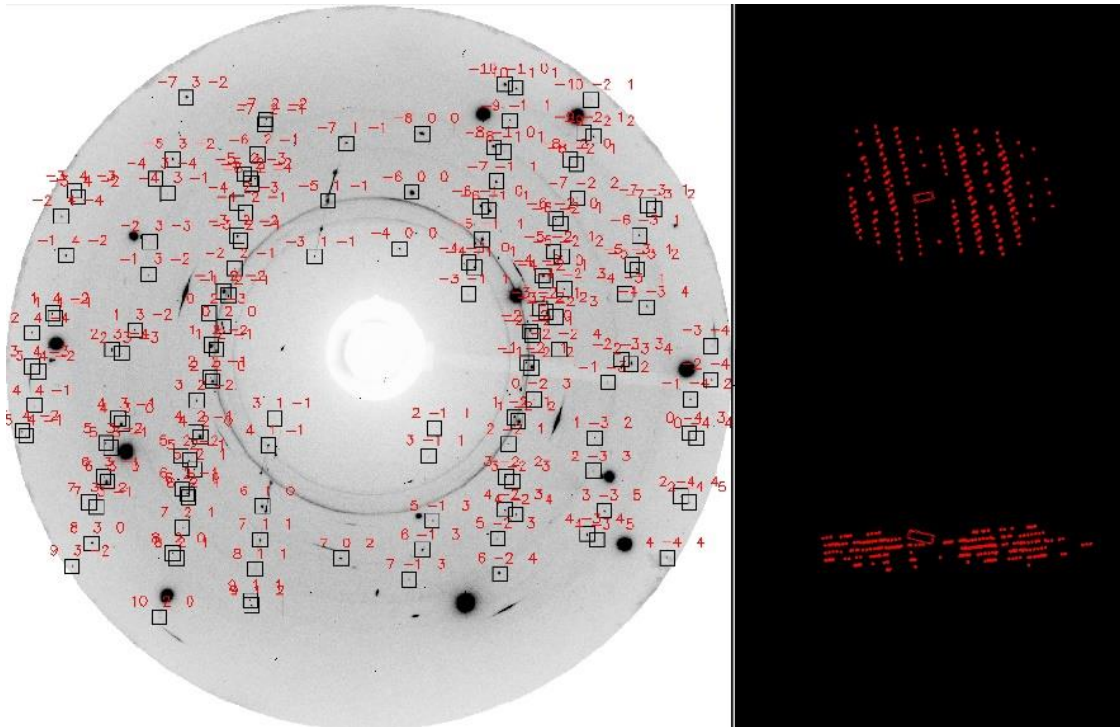


Figure 4.4. Representative single-crystal XRD image at 28.8 GPa and 700 K(left) and projections of the  $\text{Fe}_7\text{C}_3$  crystal structure in reciprocal space along different crystallographic directions (right). Red labels in the measured patterns correspond to Miller indices (hkl) of the reflections. The upper right projection is perpendicular to the X-ray beam.

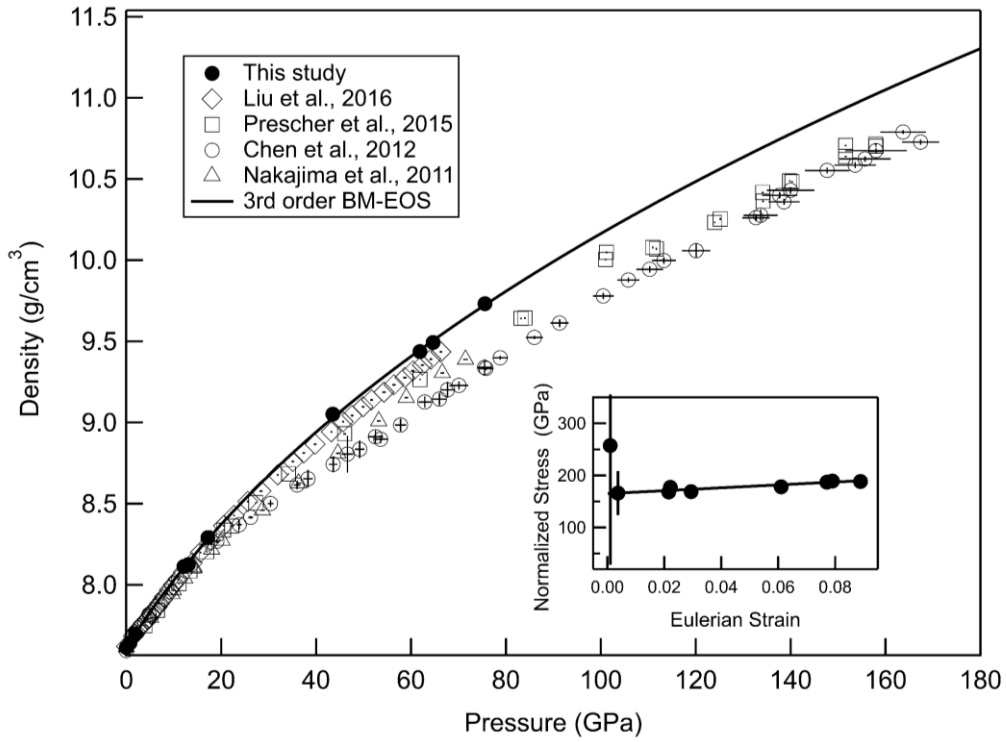


Figure 4.5. Density of the orthorhombic  $\text{Fe}_7\text{C}_3$  at 300K in this study compared with other studies. The fitted density using the third-order Birch-Murnaghan EoS is also displayed as the solid line. The solid circles represent the density of orthorhombic  $\text{Fe}_7\text{C}_3$  in this study. The pressure and density uncertainties are mostly within the symbols. The open symbols are from other studies for comparison (Chen et al., 2012; Liu et al., 2016b; Nakajima et al., 2011; Prescher et al., 2015). Inset is the  $F$ - $f$  plot of data in this study.

Table 4.1. Lattice parameters of Fe<sub>7</sub>C<sub>3</sub> obtained by high-pressure and high-temperature single-crystal X-ray Diffraction.

Pressure (GPa)	<i>a</i> (Å)	<i>b</i> (Å)	<i>c</i> (Å)	Volume (Å <sup>3</sup> )
300 K				
0.00001	11.979(1)	4.5191(8)	13.767(2)	745.3(2)
0.8(1)	11.954(2)	4.513(1)	13.76(3)	743(2)
1.9(1)	11.936(2)	4.503(1)	13.71(3)	737(2)
12.1(1)	11.766(2)	4.416(1)	13.47(2)	699.5(9)
13.1(1)	11.752(2)	4.405(1)	13.49(2)	698.4(9)
17.2(5)	11.701(2)	4.375(1)	13.37(2)	684(1)
43.5(7)	11.432(3)	4.228(1)	12.97(3)	627(1)
61.9(1)	11.266(3)	4.159(1)	12.83(2)	601(1)
64.7(1)	11.244(3)	4.150(1)	12.81(2)	598(1)
75.6(8)	11.178(3)	4.112(1)	12.68(2)	583(1)
400 K				
6.3(1)	11.872(2)	4.465(1)	13.63(2)	722(1)
12.8(1)	11.768(3)	4.407(1)	13.53(2)	702(1)
23.5(7)	11.636(2)	4.341(1)	13.27(2)	670(1)
47.7(3)	11.389(4)	4.219(1)	12.94(4)	622(2)
63(1)	11.264(3)	4.159(1)	12.83(2)	601(1)
500 K				
9.3(1)	11.839(3)	4.439(1)	13.65(3)	717(2)
13.6(1)	11.777(2)	4.407(1)	13.50(2)	700.8(9)
26.3(9)	11.607(2)	4.329(1)	13.38(2)	672(1)
49.3(6)	11.391(3)	4.213(1)	13.01(2)	624(1)

Table 4.1. (continued) Lattice parameters of Fe<sub>7</sub>C<sub>3</sub> obtained by high-pressure and high-temperature single crystal X-ray Diffraction.

63(1)	11.264(3)	4.158(1)	12.85(3)	602(1)
67.4(3)	11.237(3)	4.145(1)	12.85(2)	599(1)
77 (2)	11.178(3)	4.113(1)	12.71(2)	584(1)
78.2(2)	11.167(3)	4.108(1)	12.72(2)	583.3(9)
600 K				
11.9(1)	11.809(3)	4.423(1)	13.62(3)	711(2)
14.3(2)	11.779(2)	4.406(1)	13.55(2)	703.4(9)
27.1(9)	11.607(3)	4.328(1)	13.39(3)	672(1)
64(1)	11.268(2)	4.163(1)	12.90(2)	605.0(9)
68.7(6)	11.231(2)	4.144(1)	12.88(2)	599(1)
76 (1)	11.188(3)	4.119(1)	12.75(2)	587.4(9)
700 K				
13.4(1)	11.798(4)	4.418(1)	13.58(4)	708(2)
28.8(9)	11.600(2)	4.320(1)	13.36(2)	669(1)
57 (1)	11.323(2)	4.190(1)	13.04(2)	618.4(9)
69.1 (7)	11.237(3)	4.144(1)	12.87(3)	599(1)
70(1)	11.332(4)	4.139(1)	12.90(3)	599(1)
78.7(9)	11.161(3)	4.115(1)	12.83(4)	589(2)
800 K				
79.2(8)	11.171(3)	4.116(1)	12.80(3)	589(1)

Notes: The 10  $P$ - $V$  data at 300K were utilized in the BM-EoS fit. The 10  $P$ - $x$  (i.e  $a/b/c$ ) at 300K were utilized in the linear EoS fit. All the 36  $P$ - $V$ - $T$  data were utilized in the high-temperature BM-EoS fit. All the data were weighted by the uncertainties in both pressure and volume in the fittings.

Due to the similarity between the orthorhombic structure with the  $Pbca$  space group and the hexagonal structure with  $P6_3mc$  space group, the compressibility of  $Fe_7C_3$  was compared with the compressibility of both orthorhombic and hexagonal  $Fe_7C_3$  in the previous studies (Table 4.2 and Figure 4.5). Our bulk modulus is consistent with the orthorhombic  $Fe_7C_3$  phase from Prescher et al. (2015), but its pressure derivative,  $K'$ , is smaller (5.1(2) in this study while 6.1(1) in Prescher et al. (2015)). The discrepancy may be caused by two reasons. First, we used a gold pressure standard whereas Prescher et al. (2015) used ruby as their pressure standard. Second, our experiment involved external heating while the experiments in Prescher et al. (2015) were conducted at room temperature. The larger  $K'$  in their study may indicate less hydrostatic sample chamber with increasing pressure (this is seen in other materials, e.g. Finkelstein et al. (2017)). High temperatures could help to relax the deviatoric stress present in the sample chamber. Comparing with the hexagonal  $Fe_7C_3$  shown in Figure 4.5 and Table 4.2, our density as a function of pressure and compressibility is similar to the values reported by Liu et al. (2016b), who argued that the pressure calibration in his study might be more accurate because the Au pressure standard was placed on the top of the sample.

Table 4.2. Thermoelastic properties of Fe<sub>7</sub>C<sub>3</sub> compared with previous studies.

<i>P</i> range (GPa)	<i>T</i> range (K)	<i>K</i> <sub>0</sub> (GPa)	<i>K</i> <sub>0</sub> '	Normalized <i>V</i> <sub>0</sub> (Å <sup>3</sup> ) <sup>a</sup>	Thermoelastic properties	Method	Reference
Orthorhombic ( <i>Pbca</i> )							
0-79.2	300	165(4)	5.1(2)	93.2(3)	—	SCXRD+DAC	This study
0-79.2	300-800	167(4)	5.0(2)	93.2(3)	$dK/dT = -0.02(1)$ GPa/K $a_0 = 4.7(9) \times 10^{-5}$ K <sup>-1</sup> $a_1 = 3(5) \times 10^{-8}$ K <sup>-2b</sup>	SCXRD+DAC	This study
4-158	300	168(4)	6.1(1)	93.1 (1)	—	SCXRD+DAC	Prescher et al. (2015)
Hexagonal ( <i>P6<sub>3</sub>mc</i> )							
fm	0-18	201 (2)	4 (fixed)	93.2(1)	—	PXRD+DAC+ multianvil press	Nakajima et al. (2011)
pm	18-71.5	253 (7)	3.6(2)	92.1 (3)	$\gamma_0 = 2.57(5)$ $\theta = 920$ (140) K $q = 2.2(5)$	PXRD+DAC+ multianvil press	Nakajima et al. (2011)
fm		231	4.4	91			
nm		291	4.5	88			
pm	7-53	201 (12)	8.0 (1.4)	92.4 (2)	—	SCXRD+DAC	Chen et al. (2012)
nm	53-167	307 (6)	3.2 (1)	91.5 (4)	—	SCXRD+DAC	Chen et al. (2012)
	0	297-911	—	—	$a_0 = 3.1(6) \times 10^{-5}$ K <sup>-1</sup> $a_1 = 1.2(6) \times 10^{-8}$ K <sup>-2c</sup>	PXRD	Litasov et al. (2015)
fm	0-7	186(5)	6.9(2.2)	93.1 (1)	—	PXRD+DAC	Liu et al. (2016b)
nc	7-20	166(13)	4.9 (1.1)	93.5(4)	—	PXRD +DAC	Liu et al. (2016b)
pm	20-66	196(9)	4.9 (2)	92.3 (5)	—	PXRD +DAC	Liu et al. (2016b)

Notes: SCXRD and PXRD are acronyms of single-crystal XRD and powder XRD, respectively. fm, pm, nm and nc are acronyms of ferromagnetic, paramagnetic, nonmagnetic and noncollinear, respectively.

<sup>a</sup>Normalized *V*<sub>0</sub> represents volume per Fe<sub>7</sub>C<sub>3</sub> formula.

<sup>b</sup>The coefficient of thermal expansion was calculated as  $\alpha = \alpha_0 + \alpha_1 \times (T-300)$ .

<sup>c</sup>The coefficient of thermal expansion was calculated as  $\alpha = \alpha_0 + \alpha_1 \times T$ .

In our study, Equation (1) was used along various high-temperature isotherms at 300K, 400K, 500K, 600K, 700K, and 800K (Table 4.1 and Figure 4.6). Assuming that  $dK/dT$  is constant through the temperature ranges,  $K_{T0}$  and  $K_{T0}'$  can be described as:

$$K_{T0} = K_0 + dK/dT \times (T-300) \quad (2)$$

$$K_{T0}' = K_0' \quad (3)$$

and the temperature dependence of volume can be expressed by the empirical polynomial equation (Berman, 1988) as:

$$V_{T0} = V_0(1 + \alpha_0(T-300) + \frac{1}{2}\alpha_1(T-300)^2) \quad (4)$$

Taking the first derivative of the Equation (4) gives the thermal expansion coefficient  $\alpha_T = \alpha_0 + \alpha_1(T-300)$  by approximation. The fit to the  $P$ - $V$ - $T$  data (Table 4.1) using Equations (1-4) results in  $K_0 = 167(4)$  GPa,  $K_0' = 5.0(2)$  and  $V_0 = 745.2(2)$  Å<sup>3</sup>,  $dK/dT = -0.02(1)$  GPa/K and thermal expansion  $\alpha_T = 4.7(9) \times 10^{-5} + 3(5) \times 10^{-8} \times (T-300)$  K<sup>-1</sup>.  $K_0$ ,  $K_0'$  and  $V_0$  obtained by the high-temperature Birch-Murnaghan EoS are consistent with the values by only fitting the 300K data within the uncertainties.

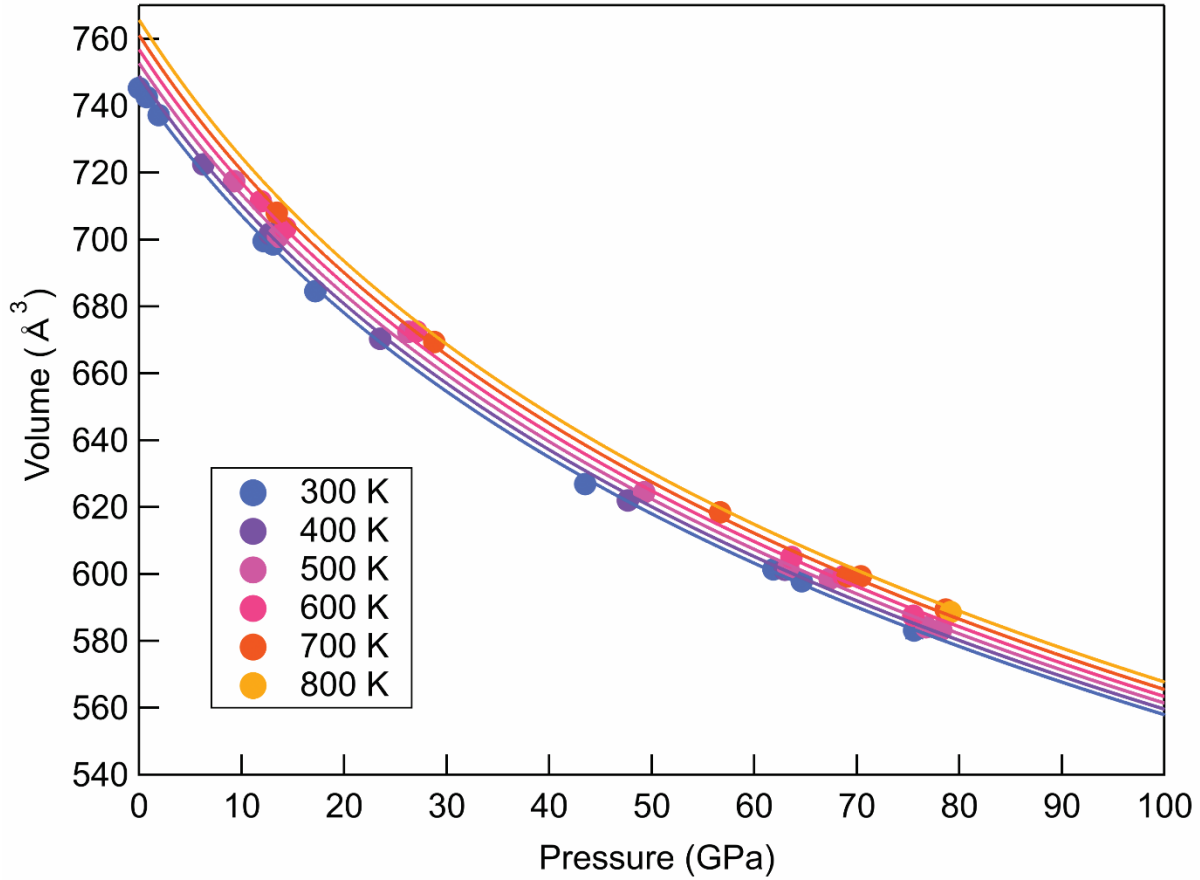


Figure 4.6.  $P$ - $V$ - $T$  data of  $\text{Fe}_7\text{C}_3$  fitted by the high-temperature Birch-Murnaghan EoS. The pressure and volume uncertainties are within the symbols. Solid curves are the fitting results.

#### 4.4.3 Compressibilities and thermal expansions of the $a$ , $b$ and $c$ axes

The compression data of the  $a$ ,  $b$  and  $c$  axes at 300 K were fitted by the EosFit7-GUI program (Gonzalez-Platas et al., 2016). The program fits the cube of the lattice parameters to obtain the linear moduli and its pressure derivative, typically denoted as  $M$  and  $M'$ , respectively (Angel et al., 2014).  $M$  is the inverse of the linear compressibility  $\beta$  ( $\beta_i = x_i^{-1}(\partial x_i / \partial P)_T$ ) and three times that of the volume-like  $K$  value (Angel, 2000). The fitting yields  $M_a = 577(14)$  GPa,  $M_a' = 18.6(9)$ ,  $M_b = 438(9)$  GPa,  $M_b' = 12.7(4)$ ,  $M_c = 490(32)$  GPa and  $M_c' = 16(2)$ .  $M_a > M_c > M_b$  indicates that the axial compressibilities of  $\text{Fe}_7\text{C}_3$  are anisotropic (Figure 4.7). Considering the trade-off between  $M$  and  $M'$ , compressibilities of the  $a$ ,  $b$  and  $c$  axes are distinguishable from each other (Figure 4.7a inset). Given that  $M_a' > M_c' > M_b'$  and considering their magnitudes, the  $b$  axis would stay the most compressible,  $\sim 17.4\%$  smaller than the  $c$  axis and  $\sim 26.5\%$  smaller than the  $a$  axis in linear modulus at 330-364 GPa (Figure 4.7b). The reason that the  $a$  and  $c$  axes are less compressible than the  $b$  axis is that Fe ions are distributed more densely in the same  $a$ - $c$

plane than in the  $b$  direction, which makes the Fe-Fe bonds shorter and stronger in  $a$  and  $c$  directions (Figure 4.3). Similar to our results, theoretical calculations by Raza et al. (2015) also indicated that the axial compressibilities of the orthorhombic  $\text{Fe}_7\text{C}_3$  are discernably anisotropic, and the compressibility of the  $b$  axis is most obviously different from those of the other axes. The calculated sound velocity ( $v_p$ ) of  $\text{Fe}_7\text{C}_3$  in  $b$  direction is the slowest, while the sound velocities in the  $a$  and  $c$  directions are relatively similar at 360 GPa (Raza et al., 2015), which is consistent with our linear incompressibility results.

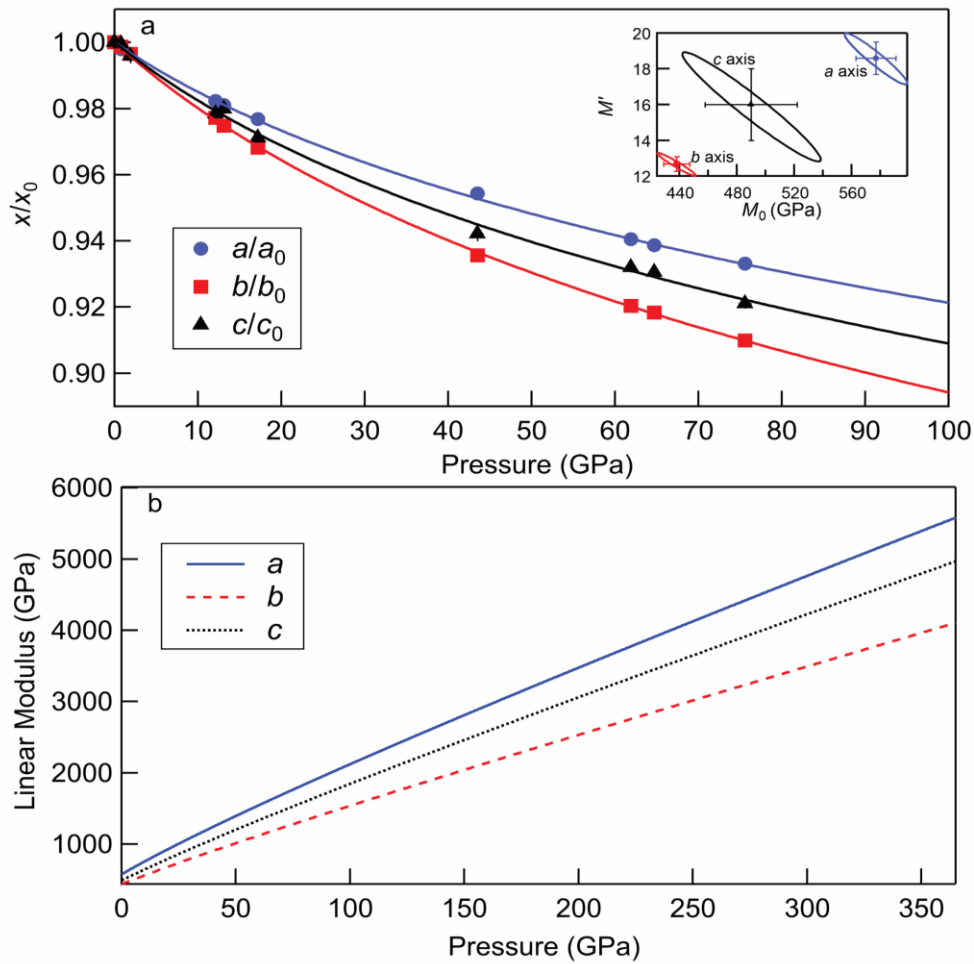


Figure 4.7. Compressibilities of the  $a$ ,  $b$  and  $c$  axes of  $\text{Fe}_7\text{C}_3$  as a function of pressure. **(a)** The variation of  $a/a_0$ ,  $b/b_0$  and  $c/c_0$  as a function of pressure were fitted by the linear EoS. The uncertainties are mostly within the symbols. Inset: the confidence ellipses for the  $a$ ,  $b$  and  $c$  axes, illustrating the trade-off between  $M_0$  and  $M'$ . **(b)** The calculated and extrapolated linear moduli of the  $a$ ,  $b$  and  $c$  axes as a function of pressure.

Thermal expansion of  $a^3$ ,  $b^3$  and  $c^3$  are also calculated using the Equation (5)(Figure 4.8 and 4.9):

$$\alpha = \frac{x_{T(P)}^3 - x_{0(P)}^3}{x_{0(P)}^3 (T - T_0)} \quad (5)$$

We found that the thermal expansions of  $c^3$  (about  $8 \times 10^{-5} \text{ K}^{-1}$ ) from 300K to 600K or 700K were larger than that of  $a^3$  and  $b^3$  by a factor of approximately 4, indicating that there are anisotropic responses of lattice expansion to high temperature along different crystallographic directions (Figure 4.9). The anisotropic response was also reflected by an increase in the  $c/a$  ratio upon heating (Figure 4.10). The  $b/a$  ratio was nearly unchanged with temperature and the  $b/c$  ratio decreased with temperature (Figure 4.10). This means that the significant change of the  $c/a$  ratio with temperature can be mainly attributed to the large expansion of the  $c$  axis upon heating.

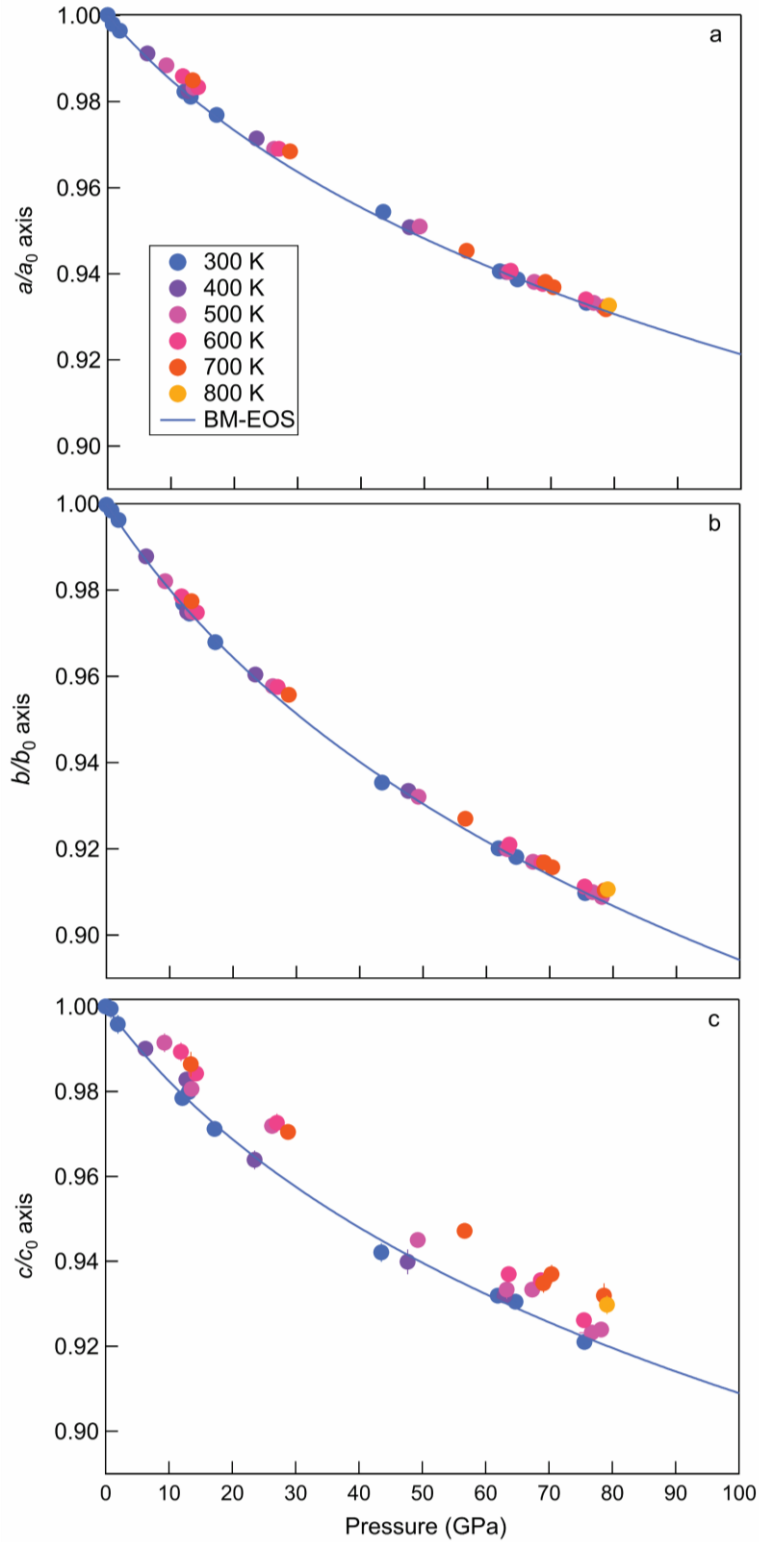


Figure 4.8. High-temperature (a)  $a/a_0$ , (b)  $b/b_0$  and (c)  $c/c_0$  of  $\text{Fe}_7\text{C}_3$  versus pressure. The room-temperature data were fitted by the linear EoS.

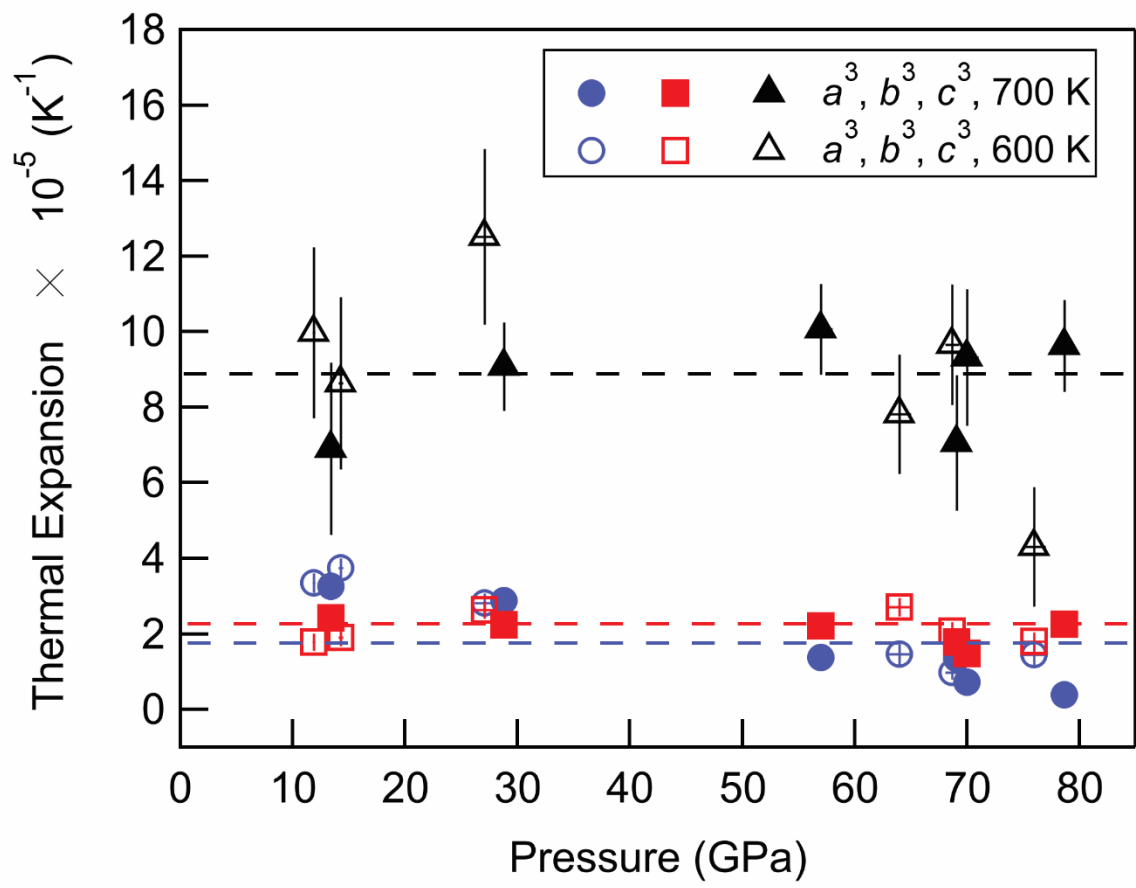


Figure 4.9. Thermal expansion of  $a^3$ ,  $b^3$  and  $c^3$  axes of  $\text{Fe}_7\text{C}_3$  at 600K and 700K. Open symbols represent the calculated thermal expansion for different axes. Dashed lines are guide lines showing the thermal expansion of  $c^3$  is approximately 4 times larger than  $a^3$  and  $b^3$ .

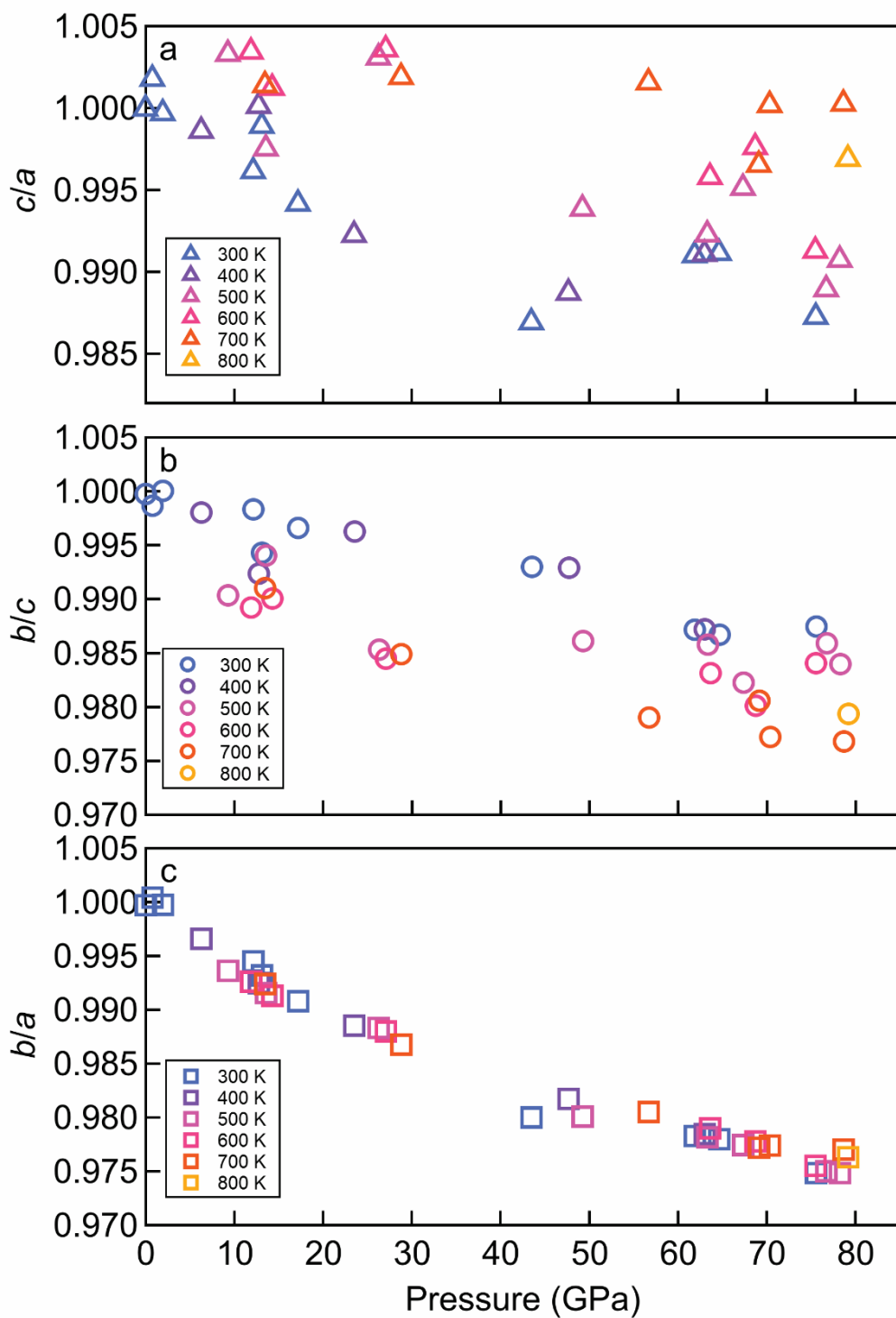


Figure 4.10. (a)  $c/a$  ratio, (b)  $b/c$  ratio and (c)  $b/a$  ratio of Fe<sub>7</sub>C<sub>3</sub> up to 800K as a function of pressure.

The distinct anisotropic responses could influence the compressibility and sound velocities of Fe<sub>7</sub>C<sub>3</sub>. For *hcp* iron, the *c/a* ratio also increases upon heating and the elastic anisotropy changes, showing that the corresponding longitudinal modulus of *c* axis,  $C_{33}$  decreases and becomes smaller than  $C_{11}$  (Steinle-Neumann, 2001). This suggests that an expanded *c* axis may result in elastic softening along this crystallography direction. One consequence might be a large sound velocity reduction along the *c* axis than the other axes at high temperatures. Although the crystal structure of *hcp* iron is different from that of Fe<sub>7</sub>C<sub>3</sub>, the change of the *c/a* ratios upon heating in Fe<sub>7</sub>C<sub>3</sub>, resulted from the compressibilities change of the crystallographic axis, may still indicate the change of the elastic anisotropy.

Along the isotherms, the *c/a* ratio gradually decreases up to ~40 GPa and then increases abruptly (Figure 4.10), probably due to the high-spin to low-spin transition of Fe<sub>7</sub>C<sub>3</sub> (Chen et al., 2012; Chen et al., 2014). For higher temperature data, the change occurs at higher pressures: this is consistent with that high temperature would promote low-spin to high-spin transition in 3d metal compounds (Gütlich et al., 1994) and probably indicates a positive slope for the spin transition (Liu et al., 2016b). The spin transition may have led to the kink in the *c/a* ratio at ~40 GPa at 300K (Figure 4.10). After the spin transition, it appears that the *c/a* ratio decreases at a similar slope as before the spin transition. The effect of the spin transition on the compressibilities of crystallographic axes is not obvious in this study. We found it was reasonable to use one linear equation of state to describe the compressibilities of crystallographic axes (Figure 4.7). Further studies with denser data coverage and to higher pressure are required to further confirm that.

Temperature may significantly influence the elastic properties of Fe<sub>7</sub>C<sub>3</sub> at high pressures. When only pressure is taken into account, the *a* and *c* axes of Fe<sub>7</sub>C<sub>3</sub> have relatively similar compressibility but the *b* axis is more compressible. According to theoretical calculations, the *b* axis is also the direction along which acoustic waves travel the slowest (Raza et al., 2015). When temperature is considered, the *c* axis expands more significantly than the other axes and thus becomes elastically softer at high temperatures, which suggests that the acoustic wave traveling along the *c* axis may also slow down and influence the elastic anisotropy. At high pressure and temperature conditions like in the inner core, the *a* axis of Fe<sub>7</sub>C<sub>3</sub> will stay the most incompressible and thus has the highest sound velocity along *a* axis. Our data implies that

temperature is an important factor when considering the anisotropy of  $\text{Fe}_7\text{C}_3$  at core conditions and caution needs to be exercised for extrapolating to the inner-core conditions.

## 4.5 Geophysical implications for the Earth's inner core

Seismological data suggest that the Earth's inner core exhibits strong elastic anisotropy, an anomalously high Poisson's ratio and low shear-wave velocity ( $v_s$ ) (Deuss (2014) and the papers cited within). These seismic features are possibly linked to the crystallographic anisotropy of the inner-core crystals. According to the theoretically calculated Fe-C phase diagram at 330 GPa, if an Fe-C liquid has >2wt.% carbon,  $\text{Fe}_7\text{C}_3$  would crystallize first to form an iron carbide inner core (Fei and Brosh, 2014); the innermost inner core has been further suggested to be  $\text{Fe}_7\text{C}_3$  based on the melting experiments of the Fe-C system to core pressures (Liu et al., 2016c). With decreasing core temperature and the depletion of carbon in the outer core by the growth of  $\text{Fe}_7\text{C}_3$  in the inner core, the Fe-C melt will approach the eutectic composition. C-doped Fe and  $\text{Fe}_7\text{C}_3$  would crystallize from the eutectic composition and form the outer part of the inner core which surrounds the innermost inner core. Our results on the anisotropic compressibility and thermal expansion of the different crystallographic axes of  $\text{Fe}_7\text{C}_3$  may provide an explanation for the seismic observations of the inner core, particularly the observed inner core anisotropy. The effect of temperature on the elastic properties and anisotropy of Fe alloys such as  $\text{Fe}_7\text{C}_3$  are crucial for us to construct a seismologically consistent core compositional model and thus inform better understanding of the composition and structure of the inner core. The thermal expansions of iron carbides at high pressures are crucial for modeling the Fe-C phase relations at extreme conditions (Fei and Brosh, 2014), which may inform our understanding of the mineralogy of the inner core and the role of carbon during inner core crystallization.

## 4.6 Acknowledgments

This work was performed at GeoSoilEnviroCARS (The University of Chicago, Sector 13), Advanced Photon Source, Argonne National Laboratory. GeoSoilEnviroCARS is supported by the National Science Foundation-Earth Sciences (EAR-1128799) and Department of Energy-GeoSciences (DE-FG02-94ER14466). This research used resources of the Advanced Photon Source, a U.S. Department of Energy (DOE) Office of Science User Facility operated for the DOE Office of Science by Argonne National Laboratory under Contract No. DE-AC02-

06CH11357. Development of the ATREX software, which was used for experimental data analysis was supported by National Science Foundation (NSF) EAR GeoInformatics grant 1440005. Development of the X-ray Atlas instrument was funded by NSF EAR Infrastructure and Facilities grant 1541516. This work was supported by the Bullard award, University of Hawai‘i at Mānoa to XL and NSF grant EAR-1555388 to BC. We are grateful to Danielle Gray for the valuable discussion.

## Chapter 5

# High-pressure Melting in the Fe-C-(H) System with Implications for the Fate of Subducted Carbon

*This chapter will be submitted as Xiaojing Lai, Feng Zhu, Jing Gao, Yingxin Liu, Eran Greenberg, Vitali B. Prakapenka, and Bin Chen, High-pressure melting in Fe-C-(H) system with implications for the fate of subducted carbon.*

### 5.1 Abstract

The subducted oceanic crust delivers significant amounts of carbon and hydrogen from the surface into the deep mantle. Through slab-mantle interactions, subducted carbon and hydrogen react with metallic iron in the metal-saturated mantle to form various reduced species such as diamond, C-H fluids and iron alloys. Therefore, the phase stability and melting behavior of the Fe-C-(H) system has been one of the foci of controversy regarding carbon and hydrogen cycling. Here we report high-pressure results on the phase relations and melting behavior of the Fe-C and Fe-C-H systems by both multi-anvil press and diamond anvil cell techniques. Metallic iron was found to react with an organic C-H compound, which served as a source for carbon and hydrogen, at high pressure and temperature conditions. With excess C-H compound, Fe carbide formed first from the reaction at relatively low temperatures of <2000 K; the sample then reacted further to form Fe hydride at higher temperatures, with diamond exsolved up to 57 GPa. Conversely, with excess Fe, the existence of hydrogen was found to depress the melting temperature of the Fe-C system, and the eutectic melting temperatures of both Fe-C and Fe-C-H system are below the mantle geotherm, facilitating the cycling of subducted carbon and hydrogen as molten iron alloy in the deep mantle. These metallic melts may provide a necessary environment for macro diamond growth and serve as a potential reservoir for both carbon and hydrogen in the mantle.

## 5.2 Introduction

The carbon and hydrogen cycles in deep Earth have attracted significant attention in recent years because C and H are not only important light element candidates for the Earth's inner and outer core, but are also essential elements for life on our habitable planet. The subducting slab, one of the most active regions in deep Earth, plays a significant role in transporting carbon- and hydrogen-bearing materials such as carbonates, hydrocarbons, and hydrous minerals into the mantle (Dasgupta and Hirschmann, 2010; Peacock, 1990). In recent years, the melting behavior of carbon- and hydrogen-bearing phases, as well as their reactions with mantle and core materials, has been extensively studied to understand the deep carbon and hydrogen cycles (Dasgupta and Hirschmann, 2010; Mao et al., 2017; Rohrbach and Schmidt, 2011).

As the mantle may become metal saturated from 250 km to the CMB (Frost et al., 2004; Rohrbach et al., 2007), the redox coupling between mantle and slab may reduce carbonates in the slab into diamond or iron carbides (Palyanov et al., 2013; Rohrbach and Schmidt, 2011; Zhu et al., 2018). Diamond has been considered to be “frozen” as a solid phase in the mantle (Rohrbach and Schmidt, 2011). However, the state of iron carbide is still under debate. The determined eutectic melting temperatures of the Fe-C system vary in previous studies. Some were lower than the mantle geotherm, which leads to the formation of metallic pockets in the mantle (Rohrbach et al., 2014), while the others were higher than the mantle geotherm, such that Fe-C phases remain solid from the upper mantle to the bottom of the lower mantle (Liu et al., 2016a). Laser heating experiments in the Fe-C system have usually yielded higher melting temperatures than large volume press experiments (Fei and Brosh, 2014; Hirayama et al., 1993; Liu et al., 2016a; Liu et al., 2016c; Lord et al., 2009; Morard and Katsura, 2010; Rohrbach et al., 2014).

Methane and hydrogen associated with metallic iron melt have been found in a group of superdeep diamonds originating from deep upper mantle to transition zone depths (Smith et al., 2016). Carbon and hydrogen were inferred to dissolve in the metallic iron phase in the deep mantle. The existence of H, even a small amount, can lower the melting point of Fe and its alloys dramatically (Fischer, 2016; Murphy, 2016). The incorporation of H may also lower the melting point of the Fe-C system, facilitating metallic melt in the mantle for diamond growth. However, the effect of H in the Fe-C-H ternary system has rarely been studied. In this study, we determined the phase relations and melting behavior of the Fe-C and Fe-C-H systems at mantle

conditions using multi-anvil press and laser-heated diamond anvil cell techniques and discuss the occurrence of C and H in the carbon and hydrogen cycles between surface and mantle.

## 5.3 Methods

### 5.3.1 Multi-anvil press experiment

Our starting materials were Fe-3 wt.%C and Fe-1-6 wt.%C0.21-1.26 wt.%H by mixing Fe (99.9+% purity, Aldrich Chemical Company) powders with graphite (99.9995% purity, Alfa Aesar Company) powder and C<sub>14</sub>H<sub>12</sub> powder (scintillation grade, Matheson Coleman & Bell Manufacturing Chemists), respectively. C<sub>14</sub>H<sub>12</sub> served as both carbon and hydrogen source. In run PL074 and PL075, TiH<sub>2</sub> + Mg(OH)<sub>2</sub> was used as hydrogen source and graphite was used as the carbon source. Experiments were conducted in a 2000-ton Walker-type multi-anvil press (Walker, 1991) at the University of Hawai‘i at Mānoa. MgO octahedra of 14 or 10 mm edge-length were compressed using tungsten carbide cubes with truncated edge of a 8 or 5mm, respectively. Pressure in 14/8 and 10/5 experiments was calibrated using the phase transitions of Bismuth (I-II transition at 2.55 GPa and transition III-IV at 7.7 GPa) (Decker et al., 1972) as well as ZnTe (9.6 and 12 GPa) (Kusaba et al., 1993). Temperature was measured using a W97%Re3%-W75%Re25% thermocouple. The Cell assembly is standard COMPRES configuration (Leinenweber et al., 2012). MgO was used as the sample capsule and it was dried and sintered in a furnace at about 1273 K for at least 12 h. After loading the sample, the cell assembly was placed in a vacuum oven at 383 K for the Fe-C sample and 353 K for the Fe-C-H sample to get rid of moisture. The sample was cold compressed to target pressure first, then temperature was increased to the target temperature in 20 min and kept at that temperature for a minimum of 15 min. The sample was then quenched by cutting power. The quenched sample was mounted in epoxy and ground longitudinally to expose its cross section. The polished samples were surrounded with silver paste as electron conductor and analyzed by a JEOL JXA-8500F field-emission gun electron microscope (EPMA), University of Hawai‘i at Mānoa under operating conditions of 15 kV and 10 nA. The samples were Aluminum coated and analyzed by a JOEL-7800FLV scanning electron microscope (SEM) at the Electron Microbeam Analysis Laboratory of the University of Michigan under operating conditions of 15 kV and 12 nA.

### 5.3.2 Laser-heated DAC experiment

High-pressure experiments were performed in BX90-type and symmetric DACs with diamonds of 250 or 300  $\mu\text{m}$  culet size. Rhenium gaskets were pre-indented to a thickness of  $\sim 30$ - $45$   $\mu\text{m}$  and sample chambers of 120 and 150  $\mu\text{m}$  in diameter were drilled. There were three configurations of the sample loadings: The first one consisted of a 5-7  $\mu\text{m}$  thick iron foil (GoodFellow, purity 99.85%) sandwiched between two  $\sim 10$   $\mu\text{m}$  thick disks of compressed  $\text{C}_{14}\text{H}_{12}$  powder (scintillation grade, Matheson Coleman & Bell Manufacturing Chemists).  $\text{C}_{14}\text{H}_{12}$  was characterized by XRD and Raman spectroscopy at the University of Hawai'i at Mānoa. The  $\text{C}_{14}\text{H}_{12}$  served as a reactant, thermal insulator, and pressure medium. Ruby was also loaded into the DAC for the pressure calibration. In the second loading, the thickness of compressed  $\text{C}_{14}\text{H}_{12}$  disks used in the first loading was reduced and KCl disks were added as thermal insulators on both sides of the first loading to make the heating more stable. The third loading comprised a small piece of 5- $\mu\text{m}$ -thick synthetic Fe-C alloy (1.2 wt% C) foil synthesized at the Geophysical Lab of the Carnegie Institution for Science, with one corner in contact with two pieces of compressed 5  $\mu\text{m}$   $\text{C}_{14}\text{H}_{12}$  disks as a hydrogen source. Two 10  $\mu\text{m}$  thick KCl disks were also loaded as the thermal insulator. In the second and third configurations, KCl served as the pressure marker; rubies were also loaded in the DACs as pressure marker for offline compression to the target pressures. A micro-manipulator at Sector 13, GSECARS, APS, ANL was used to load these complicated multi-layer samples.

High-pressure laser-heated XRD experiments were conducted at beamline 13-IDD, APS, ANL using a wavelength of 0.3344  $\text{Å}$  with a beam size of  $2.5 \times 3.5$   $\mu\text{m}$  and beamline 16-IDB, APS, ANL using a wavelength of 0.4066  $\text{Å}$  with a beam size of  $6.8 \times 5.0$   $\mu\text{m}$ . The double-sided laser heating spot is  $10 \mu\text{m} \times 15 \mu\text{m}$  at 13-IDD and  $\sim 30$   $\mu\text{m}$  in diameter at 16-IDB. A fast-reading Pilatus detector was used at 13-IDD and a MAR165 charged-coupled device (CCD) detector was used at 16-IDB. Samples were heated at an interval of 100-200 K using continuous or burst heating techniques. Burst heating was commonly used to detect melting (Prakapenka et al., 2008). It can effectively minimize the sample's exposure to the laser beam so as to prevent chemical exchanges between the heated sample and the surrounding materials. Samples were quickly heated to high temperature by setting the estimated powers of the lasers and quenched in 1-2 s. The laser shutter, temperature reading, and XRD measurement were synchronized in the heating

process. Powder XRD spectra were integrated using Dioptas software (Prescher and Prakapenka, 2015). The synchrotron XRD patterns were fitted by PDindexer software (Seto, 2010).

## 5.4 Results and discussion

### 5.4.1 Multi-anvil press experiment

Multi-anvil press experiments on the Fe-C and Fe-C-H systems were conducted at 8 GPa and 14 GPa. Starting materials comprised Fe mixed with graphite for the Fe-C experiments, and Fe mixed with C<sub>14</sub>H<sub>12</sub> for the Fe-C-H experiments. Concentrations of mixed carbon were close to the eutectic point in the Fe-C phase diagram to obtain a large proportion of melt above the melting temperature according to the lever rule for phase diagrams (Fei and Brosh, 2014; Nakajima et al., 2009). At each pressure, a series of experiments over a range of temperatures was carried out to determine melting temperatures. Melting temperatures were bracketed by textural analysis of the quenched run products which were analyzed by SEM or EPMA (Table 5.1, Table 5.2 and Figure 5.1).

Table 5.1. Experimental conditions and run products in multi-anvil press melting experiments for the Fe-C system

Run #	<i>P</i> (GPa)	<i>T</i> (K)	Heating time (min)	Phases
PL083	8	1423	30	Fe+Fe <sub>3</sub> C
PL082	8	1473	30	Melt
PL058	14	1473	30	Fe+Fe <sub>3</sub> C
PL078	14	1523	15	Fe+Fe <sub>3</sub> C
PL040	14	1573	15	Melt
PL035	14	1673	15	Melt

Table 5.2. Experimental conditions and run products in multi-anvil press melting experiments for the Fe-C-H system

Run #	$P$ (GPa)	$T$ (K)	Heating time (min)	Phases
PL075	8	1373	15	Fe+Fe <sub>3</sub> C
PL084	8	1423	20	Melt
PL085	8	1433	45	Melt
PL074	8	1473	45	Melt
PL054	14	1373	30	Fe+Fe <sub>3</sub> C+diamond
PL050	14	1473	30	Fe <sub>3</sub> C+eutectic melt
PL068	14	1473	30	Fe+eutectic melt
PL079	14	1523	30	Melt
PL087	14	1573	30	Melt
PL034	14	1673	15	Melt

The representative backscattered electron (BSE) images of the quenched samples in the Fe-C runs at 14 GPa are shown in Figure 5.1a and 5.1b. The quenched texture of Run PL078 at 1523 K is a typical subsolidus texture: granular Fe<sub>3</sub>C with straight grain boundaries in a ground mass of Fe (Figure 5.1a). The quenched texture of Run 040 at 1573 K was a dendritic melt texture composed of Fe carbide as the dendrite and Fe as the ground mass. This indicates that the onset of melting is between 1523 K and 1573 K. We chose the midpoint, 1548 K, as the eutectic melting temperature. The same processing also applied to runs at 8 GPa, which obtained 1448 K as the eutectic melting temperature. (Figure 5.2a and Figure 5.3). The slope of melting in a  $P$ - $T$  diagram was calculated to be 16.7 K/GPa, but it may have significant uncertainties due the limited pressure coverage.

Melting points in the Fe-C-H system were determined similarly. Representative BSE images from experimental runs at 14 GPa are shown in Figure 5.1c and 5.1d. Hydrogen was not detectable in the quenched product because iron hydride is not quenchable at ambient pressure (Badding et al., 1991). In Figure 5.1c, the sample of run PL054 at 1373 K is not molten. Similar subsolidus texture were observed at 1373 K. A diamond grain was found surrounded by an iron carbide phase in a ground mass of iron, likely formed from a large piece of C<sub>14</sub>H<sub>12</sub> loaded in this run. Carbon and hydrogen in C<sub>14</sub>H<sub>12</sub> can both diffuse into Fe, forming iron carbide and iron hydride. Due to the slow diffusion rate of carbon compared with hydrogen, elemental carbon can form before it fully equilibrates with iron through the surrounding carbides. Figure 5.1d shows a eutectic Fe-C melt with the intergrowth of Fe and Fe<sub>3</sub>C in the quenched sample of run PL050 at

1473 K, which can pin down the eutectic melting temperature. The eutectic melting temperature of the Fe-C-H system was determined to be 1398 K and 1473 K at 8 GPa and 14 GPa, respectively (Figure 5.2b and Figure 5.3). The slope was estimated at 12.5 K/GPa.

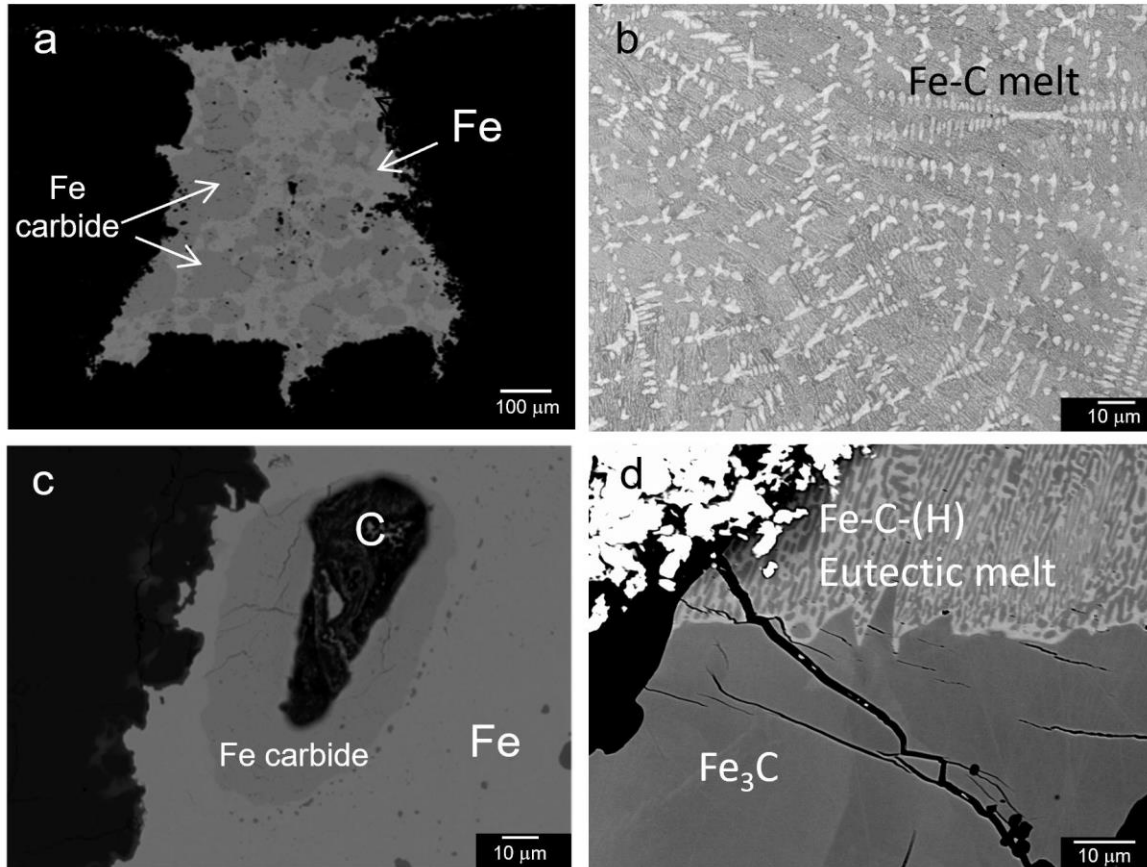


Figure 5.1. Representative BSE images of quenched texture of the run products. (a) Run PL078 conducted at 14 GPa and 1523 K. (b) Run PL040 conducted at 14 GPa and 1573 K. (c) Run PL054 at 14 GPa and 1373 K (d) Run PL050 at 14 GPa and 1473 K. (a) and (b) are the quenched products of melting experiments of Fe-C system. (c) and (d) are the quenched products of melting experiments of Fe-C-H system.

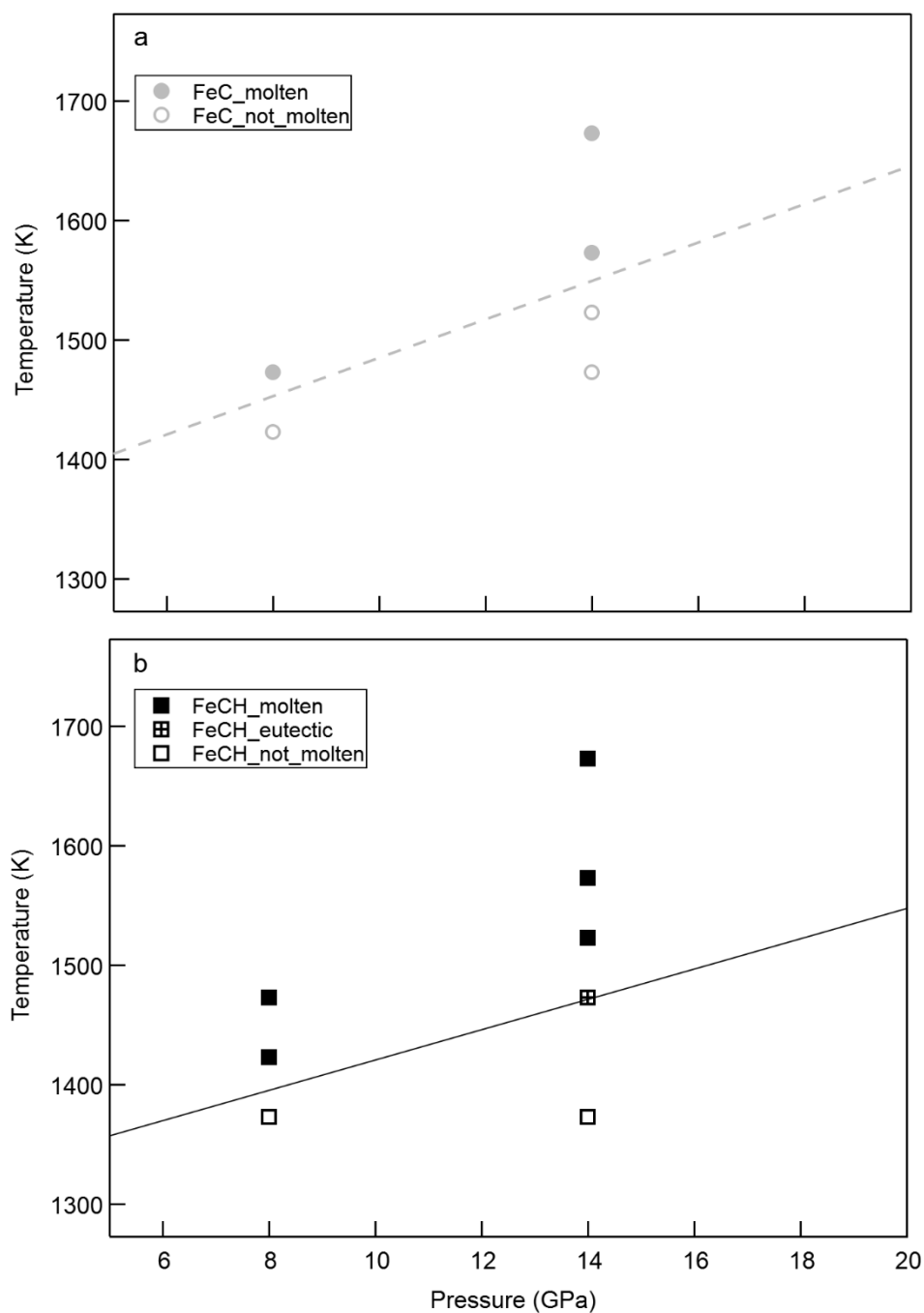


Figure 5.2. Summary of the experimental runs of (a) the Fe-C system and (b) the Fe-C-H system. The solid symbols represent runs in which the sample was molten or partially molten. The symbol with a cross inside represents the run in which eutectic melt was observed. The open symbols represent runs in which the sample was not molten. Middle point of solid and open symbol was chosen as the eutectic melting temperature except for the Fe-C-H system at 14 GPa. Dashed grey line and solid black line represent the melting lines estimated from the melting experiments.

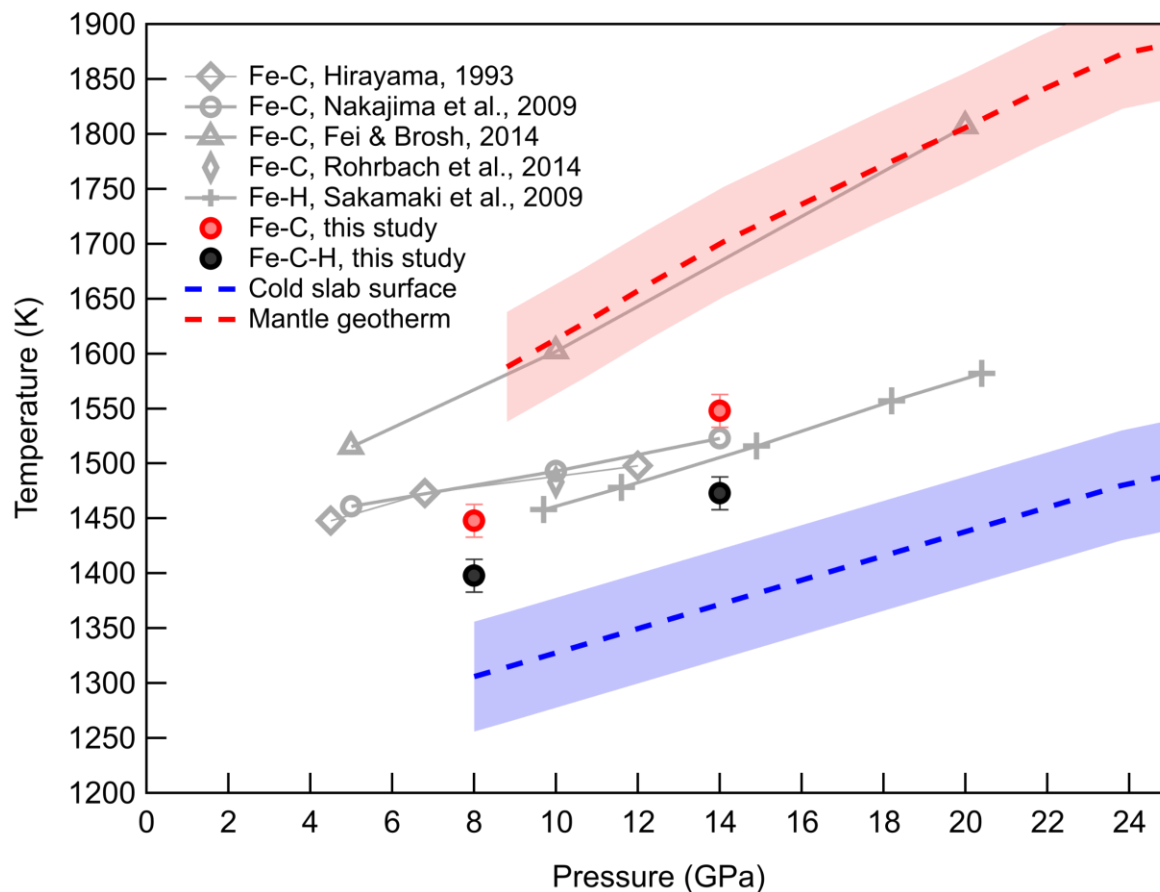


Figure 5.3. Melting temperatures of Fe-C and Fe-C-H determined by large volume press experiments compared with melting temperatures of Fe-C, Fe-H in previous large volume press studies. Mantle geotherm (red dashed line) and cold slab surface (blue dashed line) are also plotted for comparison.

The eutectic melting temperatures of the Fe-C system at 8 GPa and 14 GPa in this study agree well with the work of Rohrbach et al. (2014). They are also consistent with results of Hirayama et al. (1993) and Nakajima et al. (2009), although the slope is slightly steeper. It has the same slope as that of Fei and Brosh (2014) but the melting temperatures in this study are ~100 K lower (Figure 5.3). It is apparent from the multi-anvil press experiments in this study and previous works that the sequence of melting temperature is Fe-C > Fe-H > Fe-C-H (Figure 5.3). This indicates that a eutectic point may exist in the ternary Fe-C-H system. The average C concentration in the eutectic melt of the Fe-C-H system (run PL050) was measured by EPMA at the University of Hawai‘i at Mānoa to be 3.96(12) wt.%. This is close to the eutectic melting

composition in the Fe-C system within the uncertainties (Fei and Brosh, 2014). The hydrogen concentration cannot be estimated due to the dehydrogenation of iron hydride during decompression (Badding et al., 1991).

The lower melting temperature of the Fe-C-H system indicates that hydrogen decreased the melting temperature of the Fe-C system by 50 to 75 K at pressures of 8 GPa and 14 GPa in this study. Our results show that the eutectic melting temperatures of the Fe-C and Fe-C-H systems are above the cold slab surface and ~150 K-230 K lower than the mantle geotherm at the investigated pressure range (Figure 5.3). This could result in the melting or partial melting of these two systems, depending on the carbon concentration. When carbon and hydrogen in the subducted slab meet the iron-saturated mantle, iron carbide or iron hydride will form. There is a gradient of carbon and hydrogen concentration from the carbon- and hydrogen-enriched slab surface to the mantle. When iron becomes excess, Fe-C melt can be formed, and the presence of H will reduce the melting point of Fe-C to form Fe-C-H melt below the mantle geotherm. Both Fe-C and Fe-C-H melts provide a new way of transporting C and H from the surface into the mantle. The LVP experiments were carried out only up to 14 GPa, which represents the upper mantle pressure. Experiments under lower mantle conditions still need to be conducted.

#### **5.4.2 Laser heating experiment**

In order to study the phase relations of the Fe-C-H system and the melting behavior of Fe-C and Fe-C-H at lower mantle conditions, laser heating experiments were conducted up to 65.6 GPa. Three types of sample loadings were performed as described in the method section to serve different purposes.

##### *Reactions between Fe and C<sub>14</sub>H<sub>12</sub> at HPHT*

The DAC experiments, run-1 and run-2, were performed to study the reaction between Fe and C<sub>14</sub>H<sub>12</sub> with the first type of sample loading at 16-IDB and 13-IDD, APS, ANL, respectively. The configuration is an iron foil sandwiched between C<sub>14</sub>H<sub>12</sub> disks, which serves as C and H source as well as the thermal insulator. The disadvantage of this loading is that after several runs of heating, the insulating layers will be gradually consumed, leading to low heating efficiency due to fast thermal conductivity through diamond culets. Therefore, this loading was used only to obtain phase relations in the Fe-C-H system at HPHT.

In this reaction, the carbon and hydrogen provided by the C<sub>14</sub>H<sub>12</sub> layers were in excess compared with iron, meaning there was not enough iron to react with all C<sub>14</sub>H<sub>12</sub>. At 10 GPa and 1200 K, Fe reacted with C<sub>14</sub>H<sub>12</sub> and only Fe<sub>3</sub>C was formed (reaction 1) with no signal of hydride, which confirmed the deficiency of iron compared with C<sub>14</sub>H<sub>12</sub>. Fe prefers to combine with carbon to form iron carbide more than hydrogen to form iron hydride at this pressure and temperature (Figure 5.4). This preference to form carbide was confirmed up to 57 GPa when the heating temperature was low.



Interestingly, when iron carbide was formed, we found that free hydrogen combined with Fe away from the heating area to form FeH<sub>x</sub> (Figure 5.5):



The high diffusivity of H in hcp/fcc Fe may explain this observation. When heating the region with FeH<sub>x</sub> + C<sub>14</sub>H<sub>12</sub>, the intensity of FeH<sub>x</sub> peaks decreased while the intensity of Fe carbide rose (Figure 5.5), indicating the following reaction:



This confirmed our observation above that C has higher priority to form iron alloy and can drive H out from hydride when starting from FeH<sub>x</sub> + C<sub>14</sub>H<sub>12</sub> at high pressure and relatively low temperature (< 2000 K).

When the sample was heated to higher temperature, FeH<sub>x</sub> and diamond became the more stable phase assembly (reaction 4 and Figure 5.6a). This observation is consistent with Narygina's study (Narygina et al., 2011; Thompson et al., 2018). The diamond formed from the reaction is powder with a shape of rings in 2D image (Figure 5.6b) distinct from the single crystal diamond of the diamond anvil with a shape of points in the 2D image (Figure 5.6b).



In this sample loading, because carbon and hydrogen are excess compared with iron, the produced iron alloy phase are iron carbide without hydrogen ( $\text{Fe}_3\text{C}/\text{Fe}_7\text{C}_3$ ) or iron hydride without carbon ( $\text{FeH}_x$ ) depending on the phase stability. The melting temperature it can measure would be the melting temperature of end member of  $\text{Fe}_3\text{C}/\text{Fe}_7\text{C}_3$  and  $\text{FeH}_x$  rather than the eutectic melting temperature of the Fe-C-H ternary system. Different sample configurations, as discussed below, were designed to ensure Fe excess in the heating area, in order to measure the eutectic melting temperature of the Fe-C-H system.

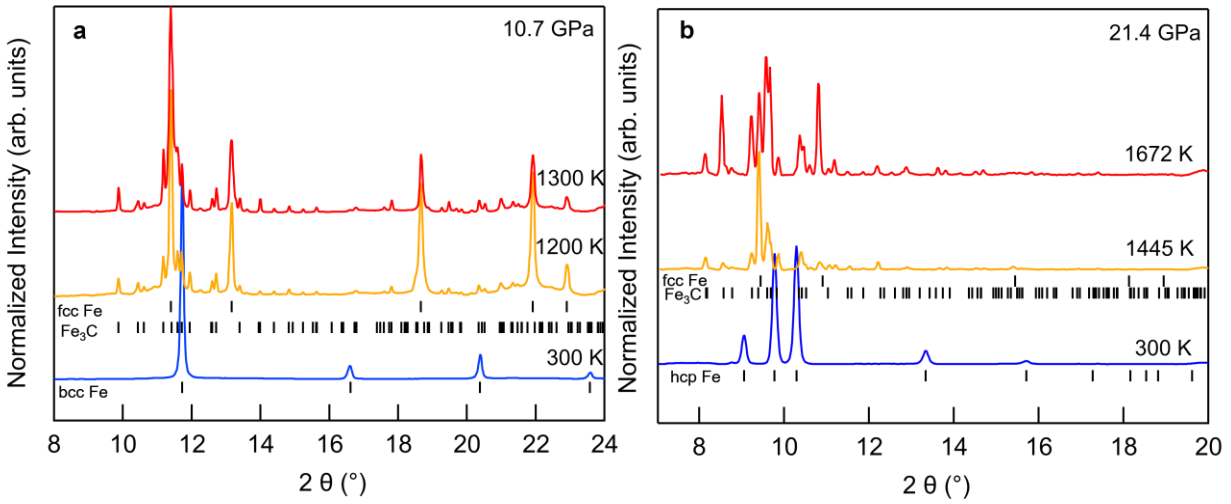


Figure 5.4. Reactions of Fe and  $\text{C}_{14}\text{H}_{12}$  (a) up to 1300 K at 10.7 GPa in run-1 and (b) up to 1672 K at 21.4 GPa in run-2. Vertical bars represent the phases identified. The XRD peaks of  $\text{C}_{14}\text{H}_{12}$  were blocked by the double-sided heating mirrors so that it was not shown in the XRD spectrum at 300 K.

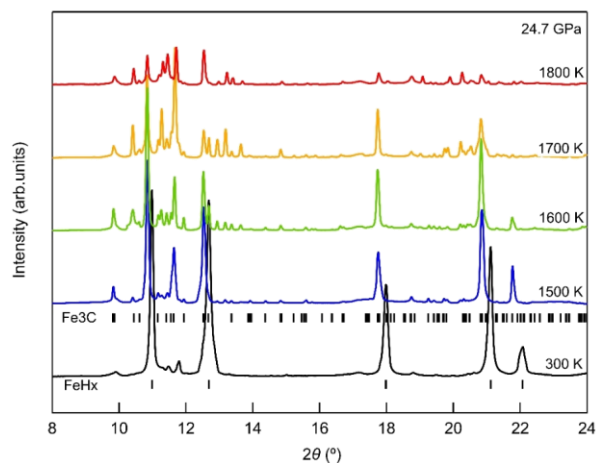


Figure 5.5. Reaction between iron hydride and  $C_{14}H_{12}$  in run-1. Vertical bars represent the phases identified from XRD.

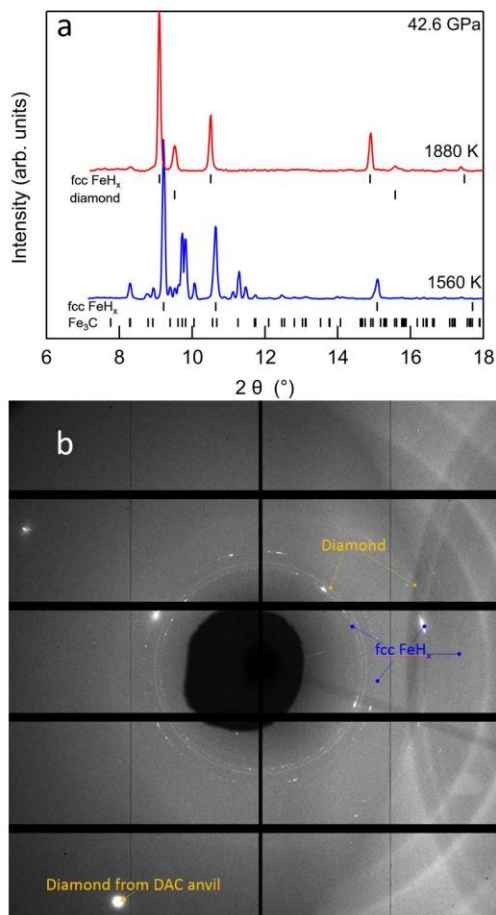


Figure 5.6. Reaction of Fe and  $C_{14}H_{12}$  up to 1880 K at 42.6 GPa in run-2. (a) Integrated XRD patterns upon heating at 42.6 GPa. Vertical bars represent the phases identified. (b) 2D image of the XRD patterns at 1880 K, 42.6 GPa.

### *Melting of Fe-C-H system*

Melting experiments (run-3 and run-4) were conducted using the second and third sample loading configurations at beamline 13-IDD of APS. In run-3 we used the second sample loading configuration, which is 5-layer loading by adding a KCl disk on each side of the C<sub>14</sub>H<sub>12</sub>-Fe sandwich. Less C<sub>14</sub>H<sub>12</sub> was loaded to make Fe excess. KCl serves as thermal insulator and the heating is more stable so that similar temperature can be reproduced by applying similar power.

Run-4 was carried out using the third sample loading. It is a synthetic Fe-interstitial 1.2 wt.%C (Fe-C hereafter) disk with one corner contacted with two pieces of compressed C<sub>14</sub>H<sub>12</sub> in a DAC. KCl served as the pressure transmitting medium and thermal insulator (Figure 5.7). The Fe-C alloy has the same structure as pure Fe, while carbon occupies the interstitial site of the iron structure. The sample was cold compressed to 24.8 GPa first. From XRD, the Fe-C alloy adopted an hcp structure. We continuously heated the C<sub>14</sub>H<sub>12</sub> in contact with one corner of Fe-C alloy (blue box in the Figure 5.7) and found that hydrogen was released into the Fe-C alloy and gradually diffused to the Fe-C far away (green box in the Figure 5.7), as confirmed by the observation of unit-cell expansion of an hcp-type Fe-C phase (Figure 5.8). This indicates formation of a Fe-C-H alloy. Hydrogen content can be calculated using the equation:

$$x=(V_{\text{Fe-C-H}_x}-V_{\text{Fe-C}})/\Delta V_{\text{H}}$$

where  $V_{\text{Fe-C}}$  and  $V_{\text{Fe-C-H}_x}$  are the atomic volume of initial Fe-C alloy and newly formed Fe-C-H alloy.  $\Delta V_{\text{H}}$  is the volume expansion caused by hydrogen per atom.  $\Delta V_{\text{H}} = 1.9 \text{ \AA}^3$  was used according to the previous work on FeH<sub>x</sub> (Narygina et al., 2011). In the Fe-C-H<sub>x</sub>, x was calculated to be 0.1. The formed Fe-C-H<sub>0.1</sub> alloy was used as the starting material of the melting temperature measurement.

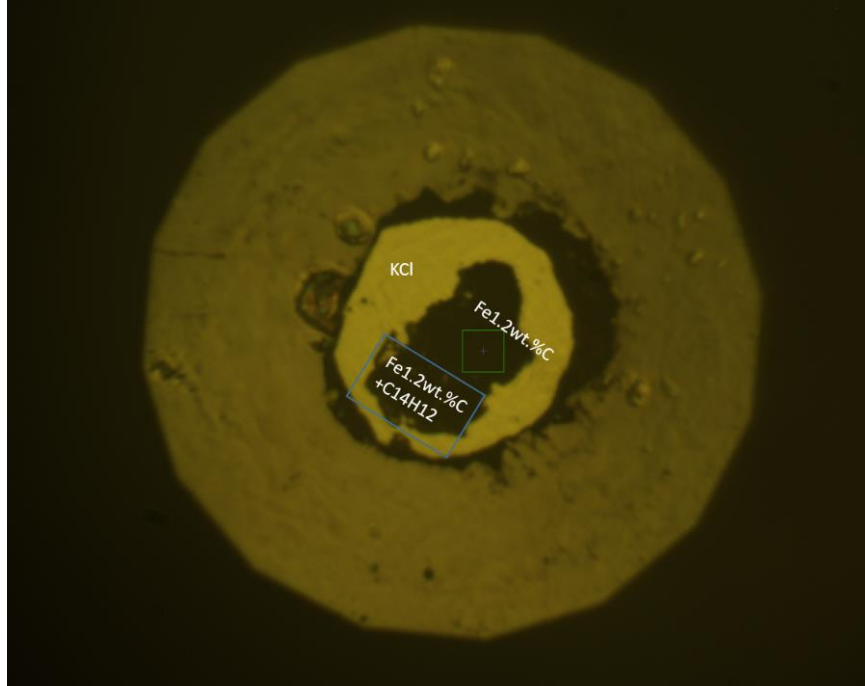


Figure 5.7. Third sample loading configuration used for the Fe-C-H melting experiment. By heating the region of the blue box, hydrogen was released to Fe1.2wt%C in the green box.

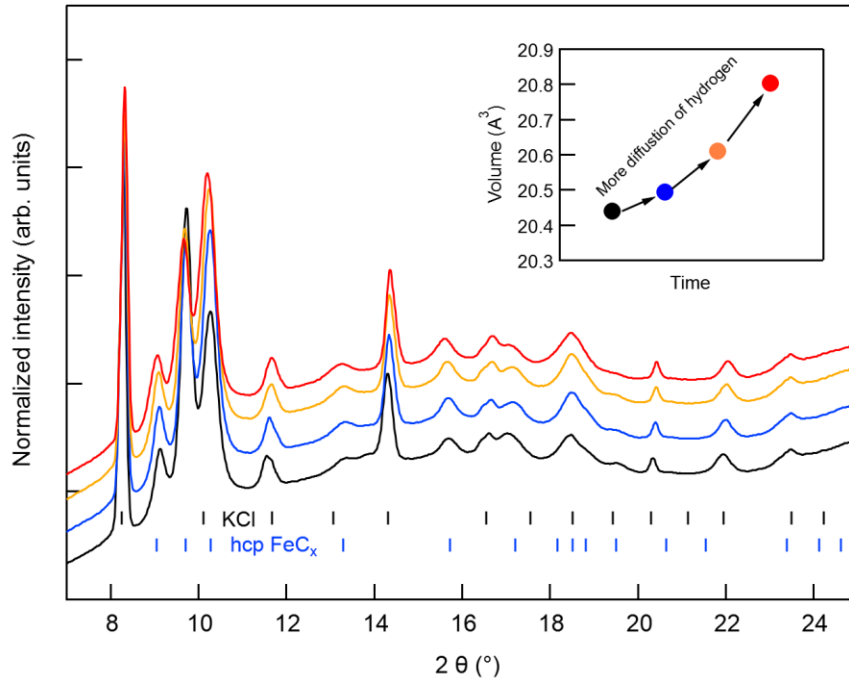


Figure 5.8. XRD patterns of hcp Fe-C before and after diffusion of hydrogen in run-4 at 13-IDD. Inset shows the volume expansion of Fe-C after gradual diffusion of hydrogen.  $\text{Fe-C-H}_x$  were formed after adding hydrogen to the crystal structure.

Melting behavior was investigated by burst heating experiments. The first observation of diffuse scattering, which is indicated by the elevated background, was used to detect the onset of melting (Figure 5.9). Melting temperature were bracketed by the highest temperature at which the sample was solid and the lowest temperature at which the diffuse scattering rings were observed. As melting occurred, the crystalline sample peaks shrank.

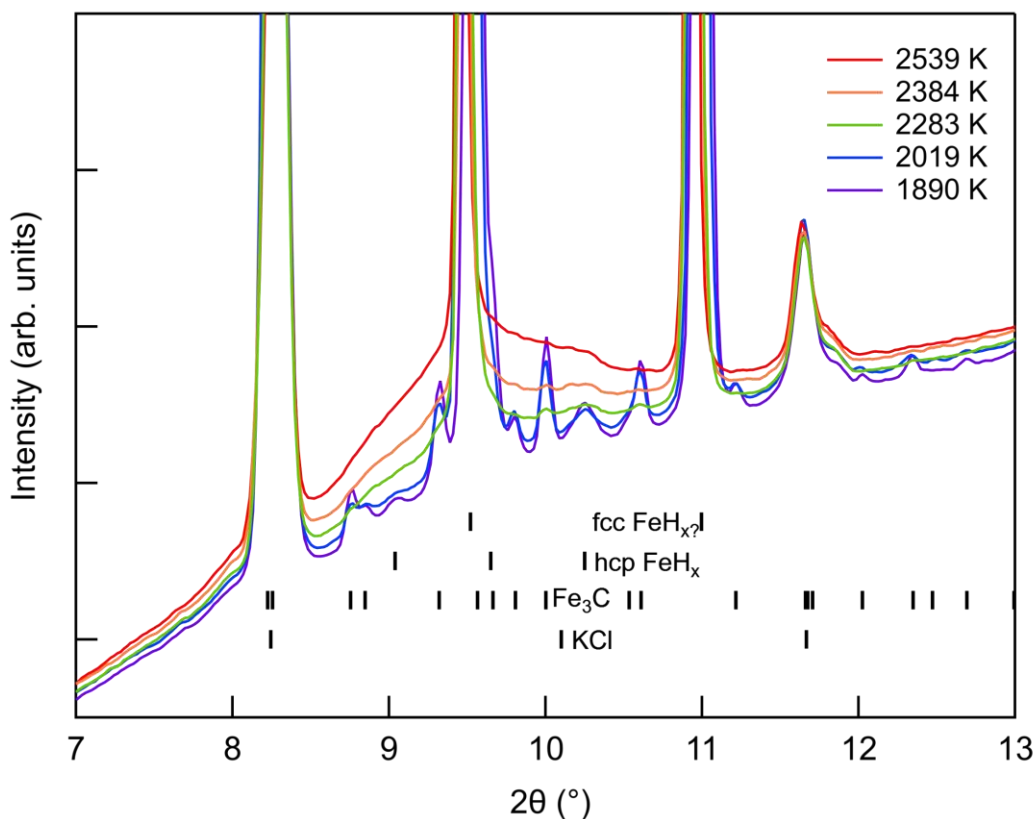


Figure 5.9. Series of representative integrated X-ray diffraction patterns at HPHT showing the evolution of melting. Purple pattern is a solid phase. The baseline was gradually elevated with increasing temperature. The elevated baseline was caused by the thermal diffuse scattering, which indicates the onset of melting, accompanied by a gradually decrease in the intensities of the crystalline peaks.

In the melting experiment of run-3, the carbon and hydrogen content in the starting material cannot be well controlled by directly reacting Fe with  $C_{14}H_{12}$  compound. If the quenched products examined by XRD consisted of both iron carbide and iron hydride, we consider it results from the eutectic melting of Fe-C-H system (Figure 5.10a). If the quenched

products consist of only iron carbide phases, we consider it results from the melting of the  $\text{Fe}_3\text{C}$  phase (Figure 5.10b). The melting temperatures of Fe-C-H and  $\text{Fe}_3\text{C}$  were summarized in Table 5.3.

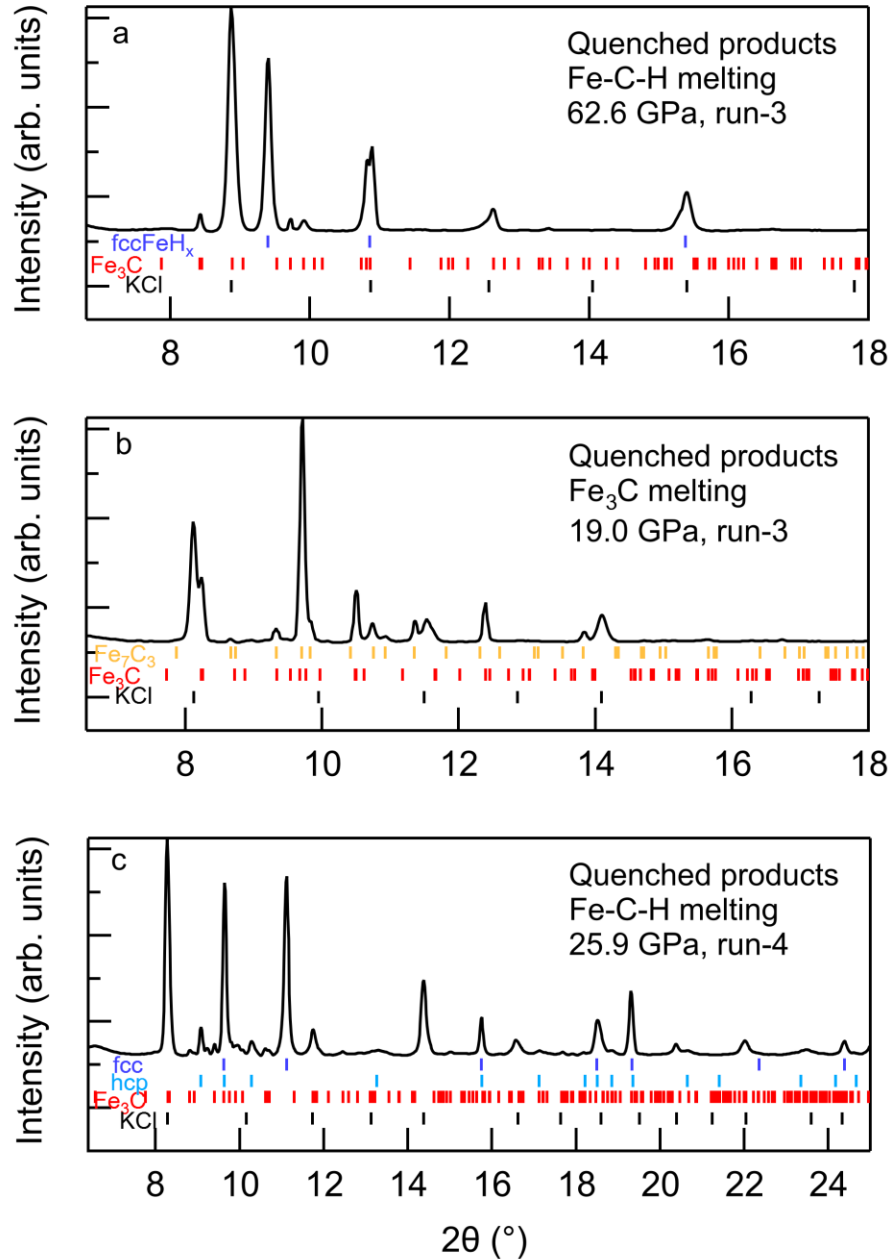


Figure 5.10 Representative XRD patterns of the quenched product after the melting of a) Fe-C-H system in run-3. b)  $\text{Fe}_3\text{C}$  in run-3. c) Fe-C-H in run-4. Vertical bars represent the different phases identified in XRD patterns. In c) the volumes of fcc and hcp phase are larger than the fcc and hcp Fe. This indicates that there are C and/or H in the interstitial sites of the crystal structure of Fe.

Melting experiments (run-4) on Fe-C-H<sub>0.1</sub> were carried out up to 51 GPa. The quenched products at about 25 GPa after melting consist of fcc and hcp Fe alloys as well as Fe<sub>3</sub>C (Figure 5.10c). The compositions of the fcc and hcp phases can be inferred from their unit-cell volumes. The observation of the Fe<sub>3</sub>C phase indicates that some C was exsolved from the starting Fe-C phase. With less carbon in the interstitial sites of the Fe-C alloy, its unit-cell volume should be smaller. The volume of the quenched hcp phase is however slightly larger than the hcp Fe-C before heating. This indicates hydrogenation in the interstitial sites of the hcp phase. Unit-cell volume of fcc Fe-C at these *P-T* conditions was not available from previous studies. At this pressure, the volume per atom of fcc Fe is 1.3% larger than that of hcp Fe. Assuming that in Fe alloy the volume of the fcc and hcp phases has the same ratio, we scaled the unit-cell volume of the fcc phase to compare with hcp Fe-C before heating. The scaled volume is slightly smaller, so it is difficult to know whether there was any hydrogen in the fcc phase after heating. In all, the existence of hydrogen in the quenched hcp phase proves that there was still hydrogen in the system during the melting experiment. The melting points of Fe-C-H in run-4 agree well with those in run-3 (Table 5.3).

Table 5.3. Melting points of Fe<sub>3</sub>C and the eutectic melting points in the Fe-C-H system

Pressure (GPa)	Temperature(K)	Run #
Fe <sub>3</sub> C		
19.0	2016(93)	Run-3
23.8	2188(22)	Run-3
24.0	2156(131)	Run-3
28.7	2250(135)	Run-3
33.1	2236(55)	Run-3
44.7	2301(90)	Run-3
52.1	2477(56)	Run-3
55.6	2508(77)	Run-3
65.6	2629(44)	Run-3
Fe-C-H system		
13.1	1821(40)	Run-3
34.8	2154(68)	Run-3
41.3	2172(85)	Run-3
47.6	2123(87)	Run-3
51.6	2268(107)	Run-3
53.6	2251(49)	Run-3
56.5	2131(86)	Run-3
56.7	2065(76)	Run-3
62.6	2257(49)	Run-3
25.9	1954(71)	Run-4
33.5	2056(83)	Run-4
41.8	2103(41)	Run-4
43.9	2147(51)	Run-4

### 5.4.3 Melting temperature of the Fe-C-(H) system by LVP and DAC

The melting temperatures from the LVP and laser-heated DAC experiments were plotted as a function of pressure, together with data from previous studies (Figure 5.11). The melting points in the Fe-C and Fe-C-H systems determined by laser-heated DAC experiments were systematically higher than those determined by resistively heated LVP experiments by 300-400 K, phenomenon well recognized in previous studies on determining the melting point by XRD using laser-heated DAC (Liu et al., 2016a; Lord et al., 2009; Morard et al., 2017) and by quenched texture using LVP (Hirayama et al., 1993; Nakajima et al., 2009). An example would be Fe: the melting temperature of Fe determined using the appearance of diffuse scattering (Anzellini et al., 2013) is higher than those determined by other newly developed methodologies to detect melting, such as XANES (Aquilanti et al., 2015), synchrotron Mössbauer spectroscopy (Zhang et al., 2016) and the internal resistive heating DAC technique (Sinmyo et al., 2019) by 700-1200 K at inner core pressure.

There are several reasons that melting temperature in the laser-heated DAC, using diffuse scattering signals as the criterion, is systematically overestimated. Firstly, the intensity of diffuse scattering depends on the volume of melt. In a eutectic melting experiment, if the initial composition is far from the eutectic composition, the portion of melt produced at eutectic melting temperature is small and may be below the detection limit. In addition, the generated melt may migrate out of the detection area. Secondly, the axial thermal gradient can be large due to minimal penetration of the laser (Salamat et al., 2014; Sinmyo et al., 2019). The temperature measurement only reads temperature on the surface, which is the hottest part of the sample. When the measured temperature on the surface reaches the melting temperature, the bulk sample in the center is still below the melting point, thus making the melting signal undetectable in XRD. A detectable melting signal requires further heating to higher temperature to melt a larger volume of the sample, resulting in overestimation of the real melting temperature. Compared with the DAC experiment, the melting temperature determined by LVP experiments may be more accurate because the thermal gradient is smaller and a thermocouple is used to measure temperature.

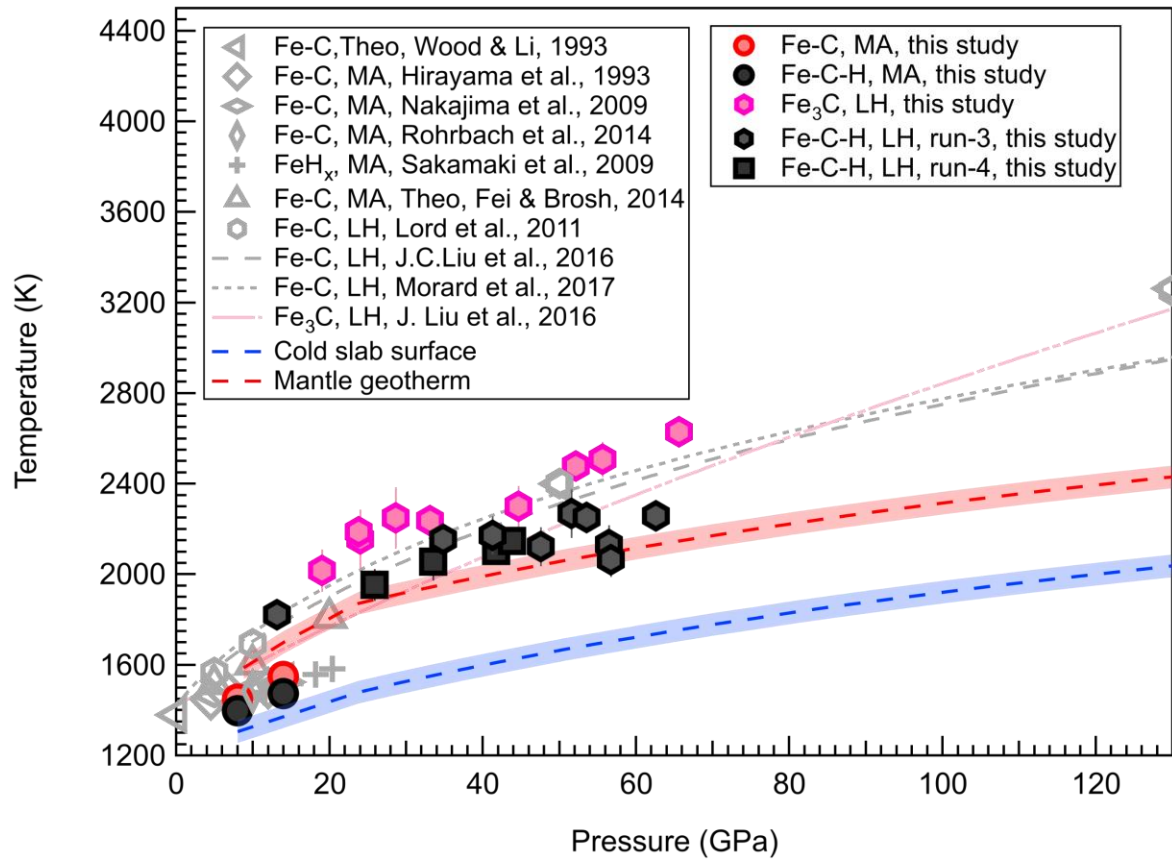


Figure 5.11. Original data for melting temperatures of Fe-C (red circles), Fe-C-H (black circles, squares and hexagons) and Fe<sub>3</sub>C (red hexagons) in this study compared with the melting temperature of Fe-C, Fe-H and Fe<sub>3</sub>C in previous studies (Grey symbols and dashed lines). Mantle geotherm (red dashed line) and cold slab surface (blue dashed line) are also plotted for comparison. MA, LH and Theo are abbreviations of multi-anvil press experiment, laser-heated DAC experiment and theoretical calculations, respectively.

Although there were some discrepancies between externally-heated LVP and laser-heated DAC experiments, curvatures were similar in the low-pressure range. Comparing results in both LVP and DAC experiments conducted at very similar pressure, a shift of -359 K was applied to data from the laser-heated DAC experiments to correct the systematic overestimation of melting temperature in the laser-heated DAC experiments.

After correction, the melting temperature of the samples as a function of pressure were fitted by the Simon-Glatzel equation (Figure 5.12):

$$T_m = T_{m0} \left( \frac{P_m - P_{m0}}{x} + 1 \right)^y$$

where  $T_m$  is the melting point at pressure  $P_m$ ,  $(P_{m0}, T_{m0})$  are the reference point, and  $x, y$  are empirical parameters obtained from the refinement. Refinement of joint LVP and DAC data gave  $x = 23.97$ ,  $y=0.257506$  with the fixed  $T_{m0} = 1398$  K and  $P_{m0} = 8$  GPa for Fe-C-H system, and  $x=73.556$ ,  $y= 0.614405$  with the fixed  $T_{m0} = 1525$  K and  $P_{m0} = 0.0001$  GPa for  $Fe_3C$  (Kubaschewski, 2013). Due to the scarcity of data points, we assumed that the curvature of the Fe-C eutectic melting at high pressures is similar to that for the Fe-C-H (Figure 5.13).

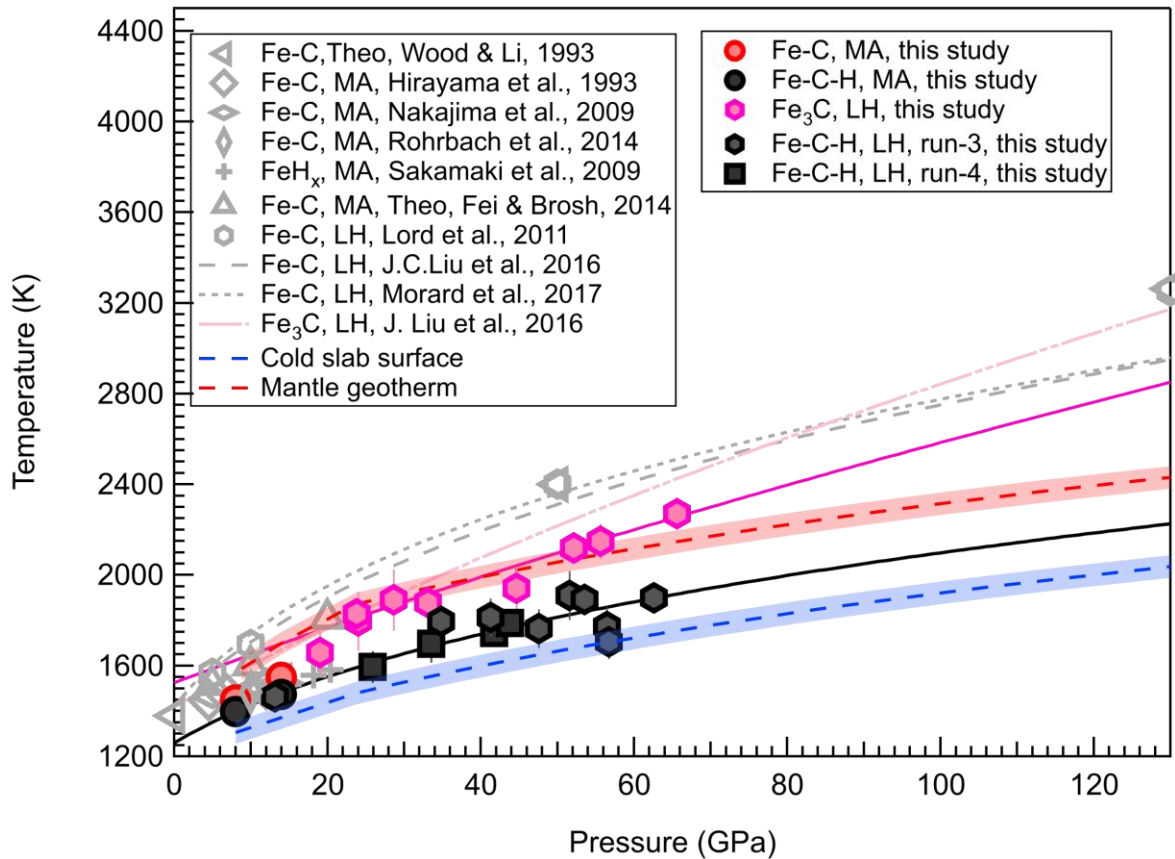


Figure 5.12. Corrected melting temperatures of Fe-C (red circles), Fe-C-H (black circles, squares and hexagons) and  $Fe_3C$  (red hexagons) in this study compared with the melting temperature of Fe-C, Fe-H and  $Fe_3C$  in previous studies (Grey symbols and dashed lines). Mantle geotherm (red dashed line) and cold slab surface (blue dashed line) are also plotted for comparison. MA, LH and Theo are abbreviations of multi-anvil press experiment, laser-heated DAC experiment and Theoretical calculations, respectively.

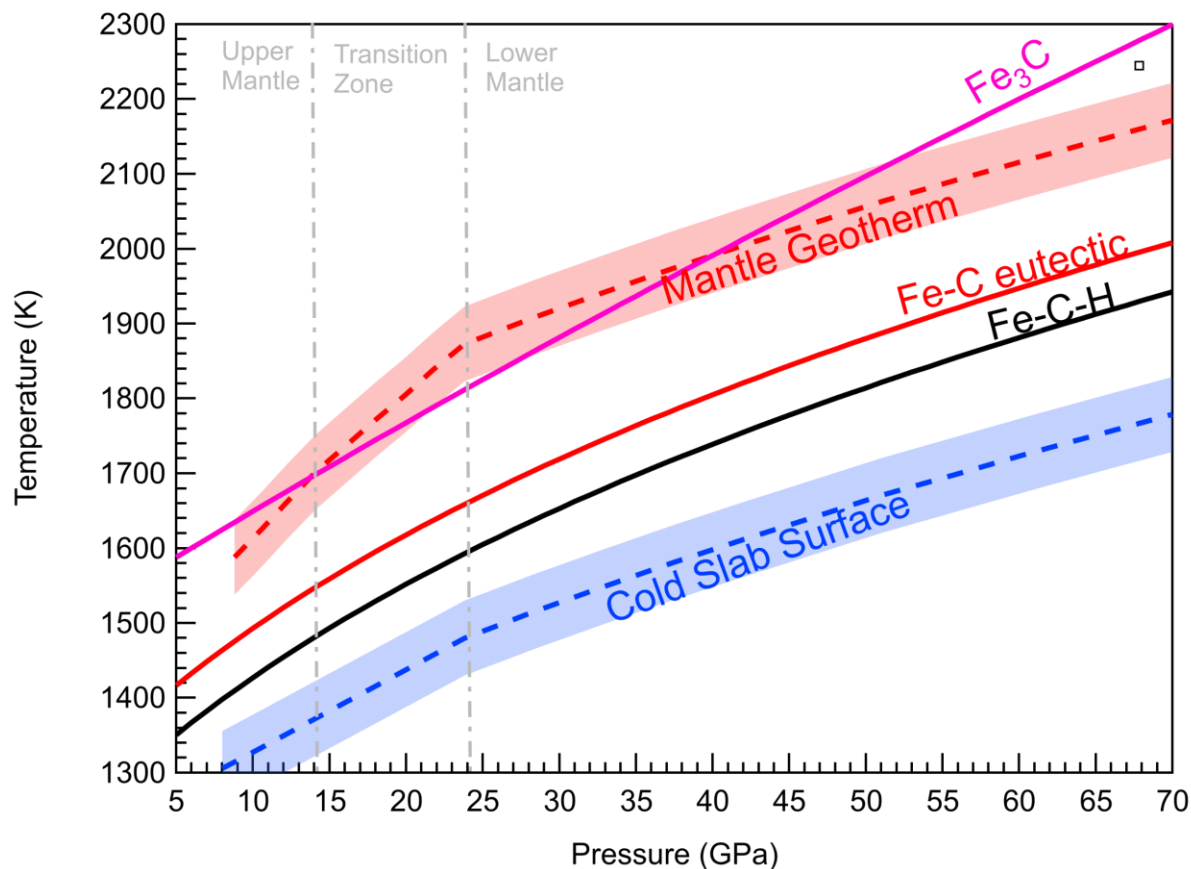


Figure 5.13. Melting curves of Fe-C, Fe-C-H and Fe<sub>3</sub>C in this study compared with mantle geotherm and cold slab surface temperature. The upper mantle, transition zone and lower mantle are separated by the grey dashed lines.

## 5.5 Implications

Melting temperatures were extended up to 63 GPa for the Fe-C-H system and were determined up to 65.6 GPa for the Fe<sub>3</sub>C system by the laser heating experiments. The melting temperature of Fe<sub>3</sub>C are higher than or very close to the mantle geotherm, so it will be ‘redox frozen’ near the cold slab surface and stay as solid in the mantle. By contrast, the eutectic melting temperatures of Fe-C and Fe-C-H are below the mantle geotherm (Figure 5.12 and 5.13); therefore, in the iron-rich area in the mantle, Fe-C and Fe-C-H eutectic melts may exist in both upper mantle and lower mantle conditions. The presence of hydrogen can further facilitate melt formation because it lowers the eutectic melting temperature of the Fe-C system.

Recently, metallic Fe-S-C melts associated with H and CH<sub>4</sub> fluids have been found in a large group of superdeep diamond inclusions (Smith et al., 2016). Particularly, hydrogen will be

driven out from metallic iron due to decreased solubility during decompression and cooling (Badding et al., 1991; Smith and Wang, 2016); hence the reduced hydrogen fluids were inferred to be also dissolved in metallic melts in the deep mantle (Smith et al., 2016). These diamonds may be evidence for the existence of Fe-C and Fe-C-H melts in the mantle. The metallic melts were proposed to serve as the solvent to grow large gem diamonds (Smith et al., 2016). Since the carbon concentration reflected by the quenched Fe-Ni + (Fe,Ni)<sub>3</sub>C assembly in these diamond inclusions is not high enough to crystallize diamond, additional hydrogen sources may be key to the exsolution of diamond. Our experiments showed that with an excess C and H source in metallic iron, hydrogen can drive carbon from the metallic phase to form diamond at high temperature. If it is the same for melt, hydrogen may decrease the solubility of carbon in an Fe-C-H melt and hence facilitate the formation of large gem diamonds in relatively carbon-poor environment.

Dense Fe-C and Fe-C-H melts may be transported to deeper part of the Earth's mantle or even into the core if their dihedral angles are small; this may account for numerous low velocity zones in the mantle and provide a pathway for modern Earth's core growth after early differentiation (Figure 5.14). If the dihedral angles are large, those melts would stay in the mantle as melt pockets. The melt pockets would be a reservoir for both carbon and hydrogen in the mantle (Figure 5.14).

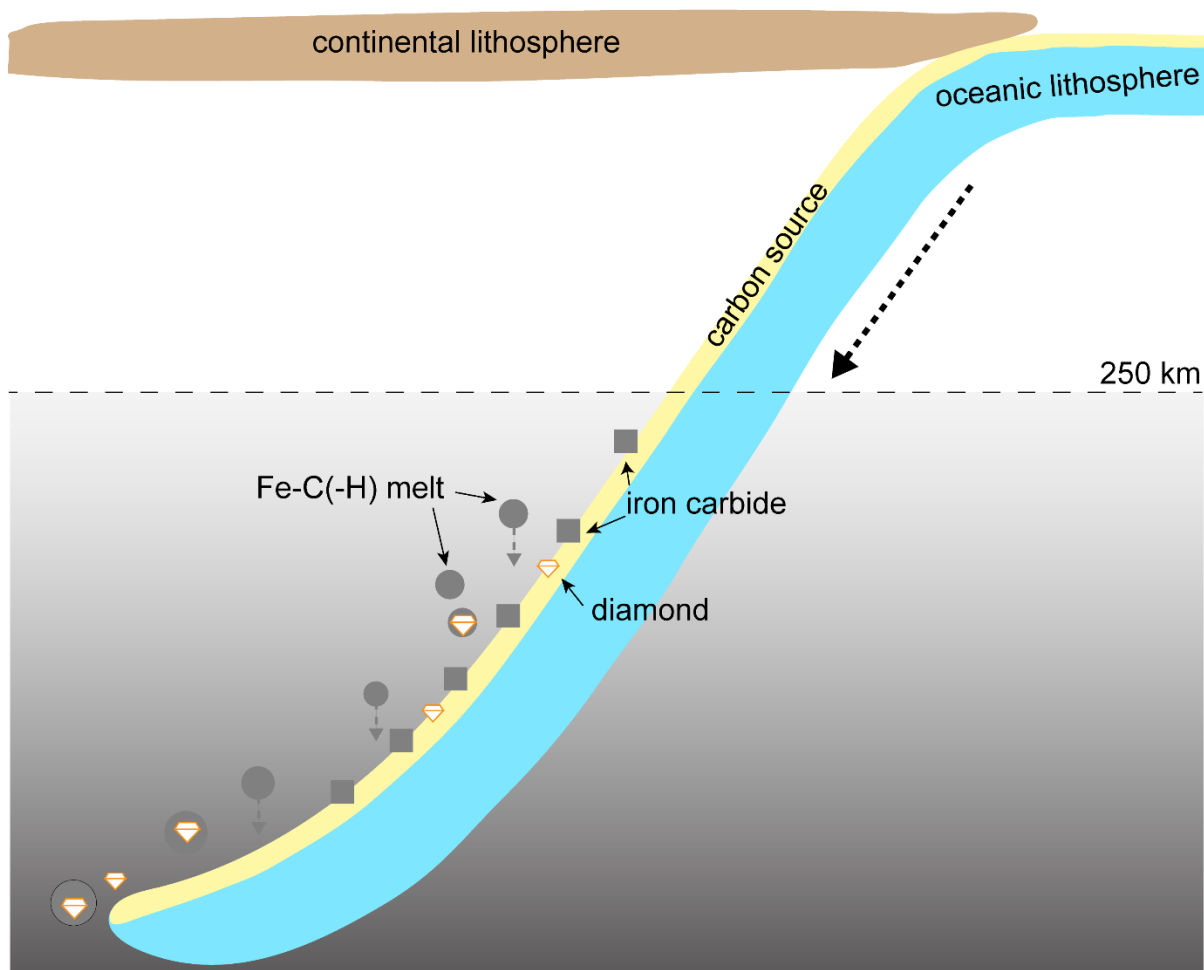


Figure 5.14. Cartoon illustrating the proposed reaction and melting under mantle conditions.

## 5.6 Acknowledgments

Authors would like to thank Eric Hellebrand and Yihang Fang for their help to do the SEM and EPMA data collection. This work was performed at HPCAT (Sector 16), Advanced Photon Source (APS), Argonne National Laboratory. HPCAT operation is supported by DOE-NNSA under Award No. DE-NA0001974, with partial instrumentation funding by NSF. We acknowledge the support of GeoSoilEnviroCARS (Sector 13), which is supported by the National Science Foundation - Earth Sciences (EAR-1128799), and the Department of Energy,

Geosciences (DE-FG02-94ER14466). The Advanced Photon Source is a U.S. Department of Energy (DOE) Office of Science User Facility operated for the DOE Office of Science by Argonne National Laboratory under Contract No. DE-AC02-06CH11357. This work was supported by NSF grants (EAR-1555388 and EAR-1565708) to BC.

## Chapter 6

### Conclusions and Future Work

This dissertation investigated carbon in deep Earth by mineral physics research on the physical properties of carbon-bearing phases, mainly focusing on the Fe-C system, at simulated high-pressure and high-temperature conditions of deep Earth.

During formation of the Earth's core, metallic liquid was equilibrated with and segregated from molten silicate in the deep magma ocean. As a siderophile element, carbon could be incorporated into iron liquids during the core-mantle differentiation process. This dissertation (Chapter 3) combined experiments and computations to provide critical information on the structural evolution of Fe-Ni-C liquids with pressure to understand the chemical evolution of terrestrial planets and moons. The notable changes of the rich features of the second NNs peaks in the derived PDFs of Fe-Ni-C liquids were found and used as primary indicators of a polyamorphic liquid structural transition at  $\sim 5$  GPa. The liquid structural transition is found to be due to the notable favoring of 3-atom polyhedra connections of Fe-Ni atomic motifs in high-pressure liquids at  $>5$  GPa by first-principles MD calculations. The structural evolution of Fe-Ni-C liquids alloys upon compression may significantly affect liquid properties such as viscosity, sound velocity, and density. The liquid structural transition may also influence the partitioning behaviors of major or trace elements and isotopic fractionation between metal and silicates during planetary core formations. As such, our findings may provide unique insights into the core formation processes that set the Earth apart from other planets or planet-forming bodies.

The inner core has crystallized from the liquid core due to the secular cooling of Earth. Seismological data suggest that the Earth's inner core exhibits strong elastic anisotropy, an anomalously high Poisson's ratio and low shear-wave velocity (Deuss (2014) and the papers cited within). These seismic features are possibly linked to crystallographic anisotropy of the inner-core crystals.  $\text{Fe}_7\text{C}_3$  would crystallize first to form an iron carbide inner core, if the carbon concentration of the preliminary liquid is  $>2\text{wt.}\%$  carbon (Fei and Brosh, 2014). In Chapter 4, we investigated the thermal equation of state, axial compressibilities and thermal expansions of  $\text{Fe}_7\text{C}_3$  at high pressures and high temperatures. The obtained thermal equation of state parameters of  $\text{Fe}_7\text{C}_3$  at high pressure are crucial for modeling Fe-C phase relations at extreme conditions

(Fei and Brosh, 2014), which may inform our understanding of the mineralogy of the inner core and the role of carbon during inner core crystallization. The anisotropic compressibility and thermal expansion of the different crystallographic axes of  $\text{Fe}_7\text{C}_3$  may provide an explanation for seismic anisotropy of the inner core, due to the preferred mineral orientation. Our study suggests that the effect of temperature on the elastic properties and anisotropy of  $\text{Fe}_7\text{C}_3$  should be taken into account when constructing a seismologically consistent core compositional model.

The deep carbon cycle between the surface and the Earth's interior has been another focus of deep carbon research. Subducted slabs carry a significant amount of carbon and hydrogen into the deep mantle. Through slab-mantle interactions, subducted carbon and hydrogen may react with metallic iron in the metal-saturated regions of the mantle to form various reduced species. In this dissertation (Chapter 5), melting behavior and reactions in the Fe-C and Fe-C-H systems were investigated to elucidate the states of carbon and hydrogen in the mantle and the environment for growing large gem diamonds. In the reaction between Fe and excess C-H, iron carbide and molecular hydrogen formed first and then, at higher temperature, iron hydride and diamond started to form. When Fe was excess, the eutectic melting temperatures of the Fe-C and Fe-C-H systems were lower than the mantle geotherm. Hydrogen can depress the melting temperature of the Fe-C system, facilitating the formation of Fe-rich melt. I concluded from experiment that Fe-C or Fe-C-H melt can form at mantle  $P$ - $T$  conditions. In addition, the Fe-C-(H) melt may be mobile in the mantle and transport C and H to the deeper part of the Earth and provide a pathway for modern Earth's core growth after early differentiation. The Fe-C-(H) melt pockets can also serve as a solvent for the growth of large gem diamonds.

To investigate further the effect of the observed liquid structure transition in Chapter 3, we will design experiments and perform calculations to study element partitioning and isotopic fractionation between liquid Fe-Ni-C and silicate at the  $P$ - $T$  conditions of a deep magma ocean. Experiments and theoretical calculations of the density and sound velocities of  $\text{Fe}_7\text{C}_3$  are still needed to extend the  $P$ - $T$  conditions in Chapter 4 to the range in the inner core, to compare with the seismic model. For Chapter 5, future work can focus on the mechanism of diamond formation in iron alloy melts, possibly including more light elements such as S to reproduce the growth environment of super-deep diamonds from the deep mantle.

## References

- Agee, C.B., 1998. Phase transformations and seismic structure in the upper mantle and transition zone. *Reviews in Mineralogy and Geochemistry* 37, 165-203.
- Akahama, Y., Kawamura, H., 2006. Pressure calibration of diamond anvil Raman gauge to 310 GPa. *Journal of Applied Physics* 100, 043516.
- Alder, B.J., Wainwright, T.E., 1959. Studies in molecular dynamics. I. General method. *The Journal of Chemical Physics* 31, 459-466.
- Alfè, D., Gillan, M., Price, G., 2002. Composition and temperature of the Earth's core constrained by combining ab initio calculations and seismic data. *Earth and Planetary Science Letters* 195, 91-98.
- Anders, E., 1977. Chemical compositions of the Moon, Earth, and eucrite parent body. *Philosophical Transactions of the Royal Society of London. Series A, Mathematical and Physical Sciences* 285, 23-40.
- Anderson, W.W., Ahrens, T.J., 1994. An equation of state for liquid iron and implications for the Earth's core. *Journal of Geophysical Research: Solid Earth* 99, 4273-4284.
- Angel, R.J., 2000. Equations of state. *Reviews in mineralogy and geochemistry* 41, 35-59.
- Angel, R.J., Alvaro, M., Gonzalez-Platas, J., 2014. EosFit7c and a Fortran module (library) for equation of state calculations. *Zeitschrift für Kristallographie-Crystalline Materials* 229, 405-419.
- Anzellini, S., Dewaele, A., Mezouar, M., Loubeyre, P., Morard, G., 2013. Melting of iron at Earth's inner core boundary based on fast X-ray diffraction. *Science* 340, 464-466.
- Aquilanti, G., Trapananti, A., Karandikar, A., Kantor, I., Marini, C., Mathon, O., Pascarelli, S., Boehler, R., 2015. Melting of iron determined by X-ray absorption spectroscopy to 100 GPa. *Proceedings of the National Academy of Sciences* 112, 12042-12045.
- Badding, J., Hemley, R., Mao, H., 1991. High-pressure chemistry of hydrogen in metals: In situ study of iron hydride. *Science* 253, 421-424.
- Barinov, V., Tsurin, V., Surikov, V., 2010. Study of mechanically synthesized carbide Fe<sub>7</sub>C<sub>3</sub>. *The Physics of Metals and Metallography* 110, 474-484.
- Berman, R.G., 1988. Internally-consistent thermodynamic data for minerals in the system Na<sub>2</sub>O-K<sub>2</sub>O-CaO-MgO-FeO-Fe<sub>2</sub>O<sub>3</sub>-Al<sub>2</sub>O<sub>3</sub>-SiO<sub>2</sub>-TiO<sub>2</sub>-H<sub>2</sub>O-CO<sub>2</sub>. *Journal of Petrology* 29, 445-522.
- Birch, F., 1952. Elasticity and constitution of the Earth's interior. *Journal of Geophysical Research* 57, 227-286.
- Birch, F., 1964. Density and composition of mantle and core. *Journal of Geophysical Research* 69, 4377-4388.
- Blöchl, P.E., 1994. Projector augmented-wave method. *Physical Review B* 50, 17953.
- Bouchard, J., 1967. Etude structurale des carbures de manganese. *Annales de Chimie* 2, 353-366.
- Chen, B., Gao, L., Lavina, B., Dera, P., Alp, E.E., Zhao, J., Li, J., 2012. Magneto-elastic coupling in compressed Fe<sub>7</sub>C<sub>3</sub> supports carbon in Earth's inner core. *Geophysical Research Letters* 39, L18301.
- Chen, B., Li, J., 2016. Carbon in the Core, in: Terasaki, H., Fischer, R.A. (Eds.), *Physics and Chemistry of the Lower Mantle and Core*, Geophysical Monograph 217, 1st ed. John Wiley & Sons, Inc.
- Chen, B., Li, J., Hauck, S.A., 2008. Non-ideal liquidus curve in the Fe-S system and Mercury's snowing core. *Geophysical Research Letters* 35, L07201.
- Chen, B., Li, Z., Zhang, D., Liu, J., Hu, M.Y., Zhao, J., Bi, W., Alp, E.E., Xiao, Y., Chow, P., 2014. Hidden carbon in Earth's inner core revealed by shear softening in dense Fe<sub>7</sub>C<sub>3</sub>. *Proceedings of the National Academy of Sciences* 111, 17755-17758.
- Cohen, A.J., Mori-Sánchez, P., Yang, W., 2011. Challenges for density functional theory. *Chemical Reviews* 112, 289-320.
- Dasgupta, R., 2013. Ingassing, storage, and outgassing of terrestrial carbon through geologic time. *Reviews in Mineralogy and Geochemistry* 75, 183-229.

- Dasgupta, R., Buono, A., Whelan, G., Walker, D., 2009. High-pressure melting relations in Fe-C-S systems: implications for formation, evolution, and structure of metallic cores in planetary bodies. *Geochimica et Cosmochimica Acta* 73, 6678-6691.
- Dasgupta, R., Hirschmann, M.M., 2010. The deep carbon cycle and melting in Earth's interior. *Earth and Planetary Science Letters* 298, 1-13.
- Dasgupta, R., Walker, D., 2008. Carbon solubility in core melts in a shallow magma ocean environment and distribution of carbon between the Earth's core and the mantle. *Geochimica et Cosmochimica Acta* 72, 4627-4641.
- Decker, D.L., Bassett, W., Merrill, L., Hall, H., Barnett, J., 1972. High-pressure calibration: A critical review. *Journal of Physical and Chemical Reference Data* 1, 773-836.
- Dera, P., Zhuravlev, K., Prakapenka, V., Rivers, M.L., Finkelstein, G.J., Grubor-Urosevic, O., Tschauer, O., Clark, S.M., Downs, R.T., 2013. High pressure single-crystal micro X-ray diffraction analysis with GSE\_ADA/RSV software. *High Pressure Research* 33, 466-484.
- Deuss, A., 2014. Heterogeneity and anisotropy of Earth's inner core. *Annual Review of Earth and Planetary Sciences* 42, 103-126.
- Ding, J., Ma, E., Asta, M., Ritchie, R.O., 2015. Second-Nearest-Neighbor Correlations from Connection of Atomic Packing Motifs in Metallic Glasses and Liquids. *Scientific Report* 5, 17429.
- Dubrovinsky, L., Dubrovinskaia, N., Bykova, E., Bykov, M., Prakapenka, V., Prescher, C., Glazyrin, K., Liermann, H.-P., Hanfland, M., Ekholm, M., 2015. The most incompressible metal osmium at static pressures above 750 gigapascals. *Nature* 525, 226-229.
- Dziewonski, A.M., Anderson, D.L., 1981. Preliminary reference Earth model. *Physics of the Earth and Planetary interiors* 25, 297-356.
- Fei, Y., Bertka, C., 2005. Planetary science. The interior of Mars. *Science* 308, 1120-1121.
- Fei, Y., Brosh, E., 2014. Experimental study and thermodynamic calculations of phase relations in the Fe-C system at high pressure. *Earth and Planetary Science Letters* 408, 155-162.
- Fei, Y., Ricolleau, A., Frank, M., Mibe, K., Shen, G., Prakapenka, V., 2007. Toward an internally consistent pressure scale. *Proceedings of the National Academy of Sciences* 104, 9182-9186.
- Finkelstein, G.J., Jackson, J.M., Sturhahn, W., Zhang, D., Alp, E.E., Toellner, T.S., 2017. Single-crystal equations of state of magnesiowüstite at high pressures. *American Mineralogist: Journal of Earth and Planetary Materials* 102, 1709-1717.
- Fischer, R.A., 2016. Melting of Fe-alloys and the thermal structure of the core. *Deep Earth: Physics and Chemistry of the Lower Mantle and Core* 217, 1.
- Fischer, R.A., Campbell, A.J., 2015. The axial ratio of hcp Fe and Fe-Ni-Si alloys to the conditions of Earth's inner core. *American Mineralogist* 100, 2718-2724.
- Friesner, R.A., 2005. Ab initio quantum chemistry: Methodology and applications. *Proceedings of the National Academy of Sciences* 102, 6648-6653.
- Frost, D.J., Liebske, C., Langenhorst, F., McCammon, C.A., Trønnes, R.G., Rubie, D.C., 2004. Experimental evidence for the existence of iron-rich metal in the Earth's lower mantle. *Nature* 428, 409-412.
- Fruchart, R., Senateur, J., Bouchaud, J., Michel, A., 1965. A propos de la structure exacte du carbure de fer Fe<sub>7</sub>C<sub>3</sub>. *Bulletin de la Societe Chimique de France*, 392.
- Gao, L., Chen, B., Wang, J., Alp, E.E., Zhao, J., Lerche, M., Sturhahn, W., Scott, H.P., Huang, F., Ding, Y., 2008. Pressure-induced magnetic transition and sound velocities of Fe<sub>3</sub>C: Implications for carbon in the Earth's inner core. *Geophysical Research Letters* 35, L17306.
- Garcia, R.F., Gagnepain-Beyneix, J., Chevrot, S., Lognonné, P., 2011. Very preliminary reference Moon model. *Physics of the Earth and Planetary Interiors* 188, 96-113.
- Gonzalez-Platas, J., Alvaro, M., Nestola, F., Angel, R., 2016. EosFit7-GUI: a new graphical user interface for equation of state calculations, analyses and teaching. *Journal of Applied Crystallography* 49, 1377-1382.
- Gütlich, P., Hauser, A., Spiering, H., 1994. Thermal and optical switching of iron (II) complexes. *Angewandte Chemie International Edition in English* 33, 2024-2054.

- Hauck, S.A., Aurnou, J.M., Dombard, A.J., 2006. Sulfur's impact on core evolution and magnetic field generation on Ganymede. *Journal of Geophysical Research: Planets* 111, E09008.
- Hauck, S.A., Margot, J.L., Solomon, S.C., Phillips, R.J., Johnson, C.L., Lemoine, F.G., Mazarico, E., McCoy, T.J., Padovan, S., Peale, S.J., 2013. The curious case of Mercury's internal structure. *Journal of Geophysical Research: Planets* 118, 1204-1220.
- Herbstein, F., Snyman, J., 1964. Identification of Eckstrom-Adcock iron carbide as Fe<sub>7</sub>C<sub>3</sub>. *Inorganic Chemistry* 3, 894-896.
- Hirayama, Y., Fujii, T., Kurita, K., 1993. The melting relation of the system, iron and carbon at high pressure and its bearing on the early stage of the Earth. *Geophysical research letters* 20, 2095-2098.
- Hirose, K., Labrosse, S., Hernlund, J., 2013. Composition and state of the core. *Annual Review of Earth and Planetary Sciences* 41, 657-691.
- Holzappel, W.B., Isaacs, N.S., 1997. High Pressure Techniques in Chemistry and Physics-A Practical Approach. *High Pressure Techniques in Chemistry and Physics-A Practical Approach*, by Edited by Wilfried B Holzappel and Neil S Isaacs, pp. 398. Oxford University Press, Jul 1997. ISBN-10: 0198558112. ISBN-13: 9780198558118, 398.
- Jing, Z., Wang, Y., Kono, Y., Yu, T., Sakamaki, T., Park, C., Rivers, M.L., Sutton, S.R., Shen, G., 2014. Sound velocity of Fe-S liquids at high pressure: Implications for the Moon's molten outer core. *Earth and Planetary Science Letters* 396, 78-87.
- Kamada, S., Ohtani, E., Terasaki, H., Sakai, T., Miyahara, M., Ohishi, Y., Hirao, N., 2012. Melting relationships in the Fe-Fe<sub>3</sub>S system up to the outer core conditions. *Earth and Planetary Science Letters* 359, 26-33.
- Kantor, I., Prakapenka, V., Kantor, A., Dera, P., Kurnosov, A., Sinogeikin, S., Dubrovinskaia, N., Dubrovinsky, L., 2012. BX90: A new diamond anvil cell design for X-ray diffraction and optical measurements. *Review of Scientific Instruments* 83, 125102.
- Kennett, B., Engdahl, E., Buland, R., 1995. Constraints on seismic velocities in the Earth from traveltimes. *Geophysical Journal International* 122, 108-124.
- Knibbe, J., Luginbühl, S., Stoevelaar, R., van der Plas, W., van Harlingen, D., Rai, N., Steenstra, E., van de Geer, R., van Westrenen, W., 2018. Calibration of a multi-anvil high-pressure apparatus to simulate planetary interior conditions. *EPJ Techniques and Instrumentation* 5, 5.
- Kono, Y., Kenney-Benson, C., Ikuta, D., Shibazaki, Y., Wang, Y., Shen, G., 2016. Ultrahigh-pressure polymorphism in GeO<sub>2</sub> glass with coordination number > 6. *Proceedings of the National Academy of Sciences* 113, 3436-3441.
- Kono, Y., Kenney-Benson, C., Shibazaki, Y., Park, C., Shen, G., Wang, Y., 2015. High-pressure viscosity of liquid Fe and FeS revisited by falling sphere viscometry using ultrafast X-ray imaging. *Physics of the Earth and Planetary Interiors* 241, 57-64.
- Kono, Y., Park, C., Kenney-Benson, C., Shen, G., Wang, Y., 2014. Toward comprehensive studies of liquids at high pressures and high temperatures: Combined structure, elastic wave velocity, and viscosity measurements in the Paris-Edinburgh cell. *Physics of the Earth and Planetary Interiors* 228, 269-280.
- Kresse, G., Furthmüller, J., 1996. Efficient iterative schemes for ab initio total-energy calculations using a plane-wave basis set. *Physical Review B* 54, 11169.
- Kubaschewski, O., 2013. *Iron-Binary phase diagrams*. Springer Science & Business Media.
- Kusaba, K., Galoisy, L., Wang, Y., Vaughan, M.T., Weidner, D.J., 1993. Determination of phase transition pressures of ZnTe under quasihydrostatic conditions, *Experimental Techniques in Mineral and Rock Physics*. Springer, pp. 643-652.
- Kuwabara, S., Terasaki, H., Nishida, K., Shimoyama, Y., Takubo, Y., Higo, Y., Shibazaki, Y., Urakawa, S., Uesugi, K., Takeuchi, A., 2016. Sound velocity and elastic properties of Fe-Ni and Fe-Ni-C liquids at high pressure. *Phys. Chem. Miner.* 43, 229-236.

- Lai, X., Zhu, F., Liu, J., Zhang, D., Hu, Y., Finkelstein, G.J., Dera, P., Chen, B., 2018. The high-pressure anisotropic thermoelastic properties of a potential inner core carbon-bearing phase, Fe<sub>7</sub>C<sub>3</sub>, by single-crystal X-ray diffraction. *American Mineralogist* 103, 1568-1574.
- Leinenweber, K.D., Tyburczy, J.A., Sharp, T.G., Soignard, E., Diedrich, T., Petuskey, W.B., Wang, Y., Mosenfelder, J.L., 2012. Cell assemblies for reproducible multi-anvil experiments (the COMPRES assemblies). *American Mineralogist* 97, 353-368.
- Li, J., Fei, Y., 2014. *Experimental constraints on core composition*, 2 ed. Elsevier Ltd.
- Li, Y., Vočadlo, L., Brodholt, J., Wood, I., 2016. Thermoelasticity of Fe<sub>7</sub>C<sub>3</sub> under inner core conditions. *Journal of Geophysical Research: Solid Earth* 121, 5828-5837.
- Litasov, K., Shatskiy, A., 2016. Composition of the Earth's core: A review. *Russian Geology and Geophysics* 57, 22-46.
- Litasov, K.D., Rashchenko, S.V., Shmakov, A.N., Palyanov, Y.N., Sokol, A.G., 2015. Thermal expansion of iron carbides, Fe<sub>7</sub>C<sub>3</sub> and Fe<sub>3</sub>C, at 297–911K determined by in situ X-ray diffraction. *Journal of Alloys and Compounds* 628, 102-106.
- Liu, J., Li, J., Hrubiak, R., Smith, J.S., 2016a. Origins of ultralow velocity zones through slab-derived metallic melt. *Proceedings of the National Academy of Sciences* 113, 5547-5551.
- Liu, J., Li, J., Ikuta, D., 2016b. Elastic softening in Fe<sub>7</sub>C<sub>3</sub> with implications for Earth's deep carbon reservoirs. *Journal of Geophysical Research: Solid Earth* 121, 1514-1524.
- Liu, J., Lin, J.F., Prakapenka, V., Prescher, C., Yoshino, T., 2016c. Phase relations of Fe<sub>3</sub>C and Fe<sub>7</sub>C<sub>3</sub> up to 185 GPa and 5200 K: Implication for the stability of iron carbide in the Earth's core. *Geophysical Research Letters* 43, 12,415-12,422.
- Lord, O., Walter, M., Dasgupta, R., Walker, D., Clark, S., 2009. Melting in the Fe–C system to 70 GPa. *Earth and Planetary Science Letters* 284, 157-167.
- Mao, H.-K., Hu, Q., Yang, L., Liu, J., Kim, D.Y., Meng, Y., Zhang, L., Prakapenka, V.B., Yang, W., Mao, W.L., 2017. When water meets iron at Earth's core–mantle boundary. *National Science Review* 4, 870-878.
- Mao, H., Wu, Y., Chen, L., Shu, J., Jephcoat, A.P., 1990. Static compression of iron to 300 GPa and Fe<sub>0.8</sub>Ni<sub>0.2</sub> alloy to 260 GPa: Implications for composition of the core. *Journal of Geophysical Research: Solid Earth* 95, 21737-21742.
- Mao, H., Xu, J.-A., Bell, P., 1986. Calibration of the ruby pressure gauge to 800 kbar under quasi-hydrostatic conditions. *Journal of Geophysical Research: Solid Earth* 91, 4673-4676.
- Mao, H., Xu, J., Struzhkin, V., Shu, J., Hemley, R., Sturhahn, W., Hu, M., Alp, E., Vocadlo, L., Alfè, D., 2001. Phonon density of states of iron up to 153 gigapascals. *Science* 292, 914-916.
- McDonough, W., 2003. Compositional model for the Earth's core. *Treatise on Geochemistry* 2, 568.
- McDonough, W.F., Sun, S.-S., 1995. The composition of the Earth. *Chemical Geology* 120, 223-253.
- Mookherjee, M., Nakajima, Y., Steinle-Neumann, G., Glazyrin, K., Wu, X., Dubrovinsky, L., McCammon, C., Chumakov, A., 2011. High-pressure behavior of iron carbide (Fe<sub>7</sub>C<sub>3</sub>) at inner core conditions. *Journal of Geophysical Research: Solid Earth* 116, B04201.
- Morard, G., Andrault, D., Antonangeli, D., Nakajima, Y., Auzende, A., Boulard, E., Cervera, S., Clark, A., Lord, O., Siebert, J., 2017. Fe–FeO and Fe–Fe<sub>3</sub>C melting relations at Earth's core–mantle boundary conditions: Implications for a volatile-rich or oxygen-rich core. *Earth and Planetary Science Letters* 473, 94-103.
- Morard, G., Katsura, T., 2010. Pressure–temperature cartography of Fe-S-Si immiscible system. *Geochimica et Cosmochimica Acta* 74, 3659-3667.
- Murphy, C.A., 2016. Hydrogen in the Earth's Core: Review of the Structural, Elastic, and Thermodynamic Properties of Iron-Hydrogen Alloys. *Deep Earth: Physics and Chemistry of the Lower Mantle and Core* 217, 255.
- Nakajima, Y., Takahashi, E., Sata, N., Nishihara, Y., Hirose, K., Funakoshi, K., Ohishi, Y., 2011. Thermoelastic property and high-pressure stability of Fe<sub>7</sub>C<sub>3</sub>: Implication for iron-carbide in the Earth's core. *American Mineralogist* 96, 1158-1165.

- Nakajima, Y., Takahashi, E., Suzuki, T., Funakoshi, K.-i., 2009. "Carbon in the core" revisited. *Physics of the Earth and Planetary Interiors* 174, 202-211.
- Narygina, O., Dubrovinsky, L.S., McCammon, C.A., Kurnosov, A., Kantor, I.Y., Prakapenka, V.B., Dubrovinskaya, N.A., 2011. X-ray diffraction and Mössbauer spectroscopy study of fcc iron hydride FeH at high pressures and implications for the composition of the Earth's core. *Earth and Planetary Science Letters* 307, 409-414.
- Okuchi, T., 1997. Hydrogen partitioning into molten iron at high pressure: implications for Earth's core. *Science* 278, 1781-1784.
- Palyanov, Y.N., Bataleva, Y.V., Sokol, A.G., Borzdov, Y.M., Kupriyanov, I.N., Reutsky, V.N., Sobolev, N.V., 2013. Mantle–slab interaction and redox mechanism of diamond formation. *Proceedings of the National Academy of Sciences* 110, 20408-20413.
- Peacock, S.A., 1990. Fluid processes in subduction zones. *Science* 248, 329-337.
- Perdew, J.P., Chevary, J.A., Vosko, S.H., Jackson, K.A., Pederson, M.R., Singh, D.J., Fiolhais, C., 1992. Atoms, molecules, solids, and surfaces: Applications of the generalized gradient approximation for exchange and correlation. *Physical Review B: Condensed Matter* 46, 6671-6687.
- Platten, J.K., 2006. The Soret effect: a review of recent experimental results. *Journal of Applied Mechanics* 73, 5-15.
- Poirier, J.-P., 1994. Light elements in the Earth's outer core: a critical review. *Physics of the Earth and Planetary Interiors* 85, 319-337.
- Poitrasson, F., Halliday, A.N., Lee, D.-C., Levasseur, S., Teutsch, N., 2004. Iron isotope differences between Earth, Moon, Mars and Vesta as possible records of contrasted accretion mechanisms. *Earth and Planetary Science Letters* 223, 253-266.
- Polyakov, V.B., 2009. Equilibrium iron isotope fractionation at core-mantle boundary conditions. *Science* 323, 912-914.
- Prakapenka, V., Kubo, A., Kuznetsov, A., Laskin, A., Shkurikhin, O., Dera, P., Rivers, M., Sutton, S., 2008. Advanced flat top laser heating system for high pressure research at GSECARS: application to the melting behavior of germanium. *High Pressure Research* 28, 225-235.
- Prescher, C., Dubrovinsky, L., Bykova, E., Kuppenko, I., Glazyrin, K., Kantor, A., McCammon, C., Mookherjee, M., Nakajima, Y., Miyajima, N., 2015. High Poisson's ratio of Earth's inner core explained by carbon alloying. *Nature Geoscience* 8, 220-223.
- Prescher, C., Prakapenka, V.B., 2015. DIOPTAS: a program for reduction of two-dimensional X-ray diffraction data and data exploration. *High Pressure Research* 35, 223-230.
- Raza, Z., Shulumba, N., Caffrey, N.M., Dubrovinsky, L., Abrikosov, I.A., 2015. First-principles calculations of properties of orthorhombic iron carbide Fe<sub>7</sub>C<sub>3</sub> at the Earth's core conditions. *Physical Review B* 91, 214112.
- Rohrbach, A., Ballhaus, C., Golla–Schindler, U., Ulmer, P., Kamenetsky, V.S., Kuzmin, D.V., 2007. Metal saturation in the upper mantle. *Nature* 449, 456-458.
- Rohrbach, A., Ghosh, S., Schmidt, M.W., Wijbrans, C.H., Klemme, S., 2014. The stability of Fe-Ni carbides in the Earth's mantle: evidence for a low Fe-Ni-C melt fraction in the deep mantle. *Earth and Planetary Science Letters* 388, 211-221.
- Rohrbach, A., Schmidt, M.W., 2011. Redox freezing and melting in the Earth's deep mantle resulting from carbon-iron redox coupling. *Nature* 472, 209-212.
- Rubie, D., Nimmo, F., Melosh, H., 2007. Formation of Earth's core. *Earth Evolution Sciences* 9, 43-79.
- Salamat, A., Fischer, R.A., Briggs, R., McMahon, M.I., Petitgirard, S., 2014. In situ synchrotron X-ray diffraction in the laser-heated diamond anvil cell: Melting phenomena and synthesis of new materials. *Coordination Chemistry Reviews* 277, 15-30.
- Sanloup, C., Guyot, F., Gillet, P., Fiquet, G., Hemley, R., Mezouar, M., Martinez, I., 2000. Structural changes in liquid Fe at high pressures and high temperatures from synchrotron X-ray diffraction. *EPL (Europhysics Letters)* 52, 151.

- Sanloup, C., Van Westrenen, W., Dasgupta, R., Maynard-Casely, H., Perrillat, J.-P., 2011. Compressibility change in iron-rich melt and implications for core formation models. *Earth and Planetary Science Letters* 306, 118-122.
- Schauble, E.A., 2004. Applying stable isotope fractionation theory to new systems. *Reviews in Mineralogy and Geochemistry* 55, 65-111.
- Seto, Y., 2010. Development of a software suite on X-ray diffraction experiments. *The Review of High Pressure Science and Technology* 20, 269-276.
- Sheldrick, G.M., 2008. A short history of SHELX. *Acta Crystallographica Section A: Foundations of Crystallography* 64, 112-122.
- Shen, G., Prakapenka, V.B., Rivers, M.L., Sutton, S.R., 2004. Structure of liquid iron at pressures up to 58 GPa. *Physical Review Letters* 92, 185701.
- Shen, G., Rivers, M.L., Wang, Y., Sutton, S.R., 2001. Laser heated diamond cell system at the Advanced Photon Source for in situ X-ray measurements at high pressure and temperature. *Review of Scientific Instruments* 72, 1273-1282.
- Shibazaki, Y., Kono, Y., Fei, Y., 2015. Microscopic structural change in a liquid Fe-C alloy of ~5 GPa. *Geophysical Research Letters* 42, 5236-5242.
- Shimoyama, Y., Terasaki, H., Ohtani, E., Urakawa, S., Takubo, Y., Nishida, K., Suzuki, A., Katayama, Y., 2013. Density of Fe-3.5 wt% C liquid at high pressure and temperature and the effect of carbon on the density of the molten iron. *Physics of the Earth and Planetary Interiors* 224, 77-82.
- Shimoyama, Y., Terasaki, H., Urakawa, S., Takubo, Y., Kuwabara, S., Kishimoto, S., Watanuki, T., Machida, A., Katayama, Y., Kondo, T., 2016. Thermoelastic properties of liquid Fe-C revealed by sound velocity and density measurements at high pressure. *Journal of Geophysical Research: Solid Earth* 121, 7984-7995.
- Sinmyo, R., Hirose, K., Ohishi, Y., 2019. Melting curve of iron to 290 GPa determined in a resistance-heated diamond-anvil cell. *Earth and Planetary Science Letters* 510, 45-52.
- Smith, E.M., Shirey, S.B., Nestola, F., Bullock, E.S., Wang, J., Richardson, S.H., Wang, W., 2016. Large gem diamonds from metallic liquid in Earth's deep mantle. *Science* 354, 1403-1405.
- Smith, E.M., Wang, W., 2016. Fluid CH<sub>4</sub> and H<sub>2</sub> trapped around metallic inclusions in HPHT synthetic diamond. *Diamond and Related Materials* 68, 10-12.
- Sobolev, A., Mirzoev, A., 2013. Ab initio studies of the short-range atomic structure of liquid iron-carbon alloys. *Journal of Molecular Liquids* 179, 12-17.
- Steinle-Neumann, G., Stixrude, L., Cohen, R., Gülseren, O., 2001. Elasticity of iron at the temperature of the Earth's inner core. *Nature* 413, 57.
- Stevenson, D.J., 1981. Models of the Earth's Core. *Science* 214, 611-619.
- Stevenson, D.J., 2003. Planetary magnetic fields. *Earth and Planetary Science Letters* 208, 1-11.
- Stewart, A.J., Schmidt, M.W., van Westrenen, W., Liebske, C., 2007. Mars: a new core-crystallization regime. *Science* 316, 1323-1325.
- Tateno, S., Kuwayama, Y., Hirose, K., Ohishi, Y., 2015. The structure of Fe-Si alloy in Earth's inner core. *Earth and Planetary Science Letters* 418, 11-19.
- Terasaki, H., Nishida, K., Shibazaki, Y., Sakamaki, T., Suzuki, A., Ohtani, E., Kikegawa, T., 2010. Density measurement of Fe<sub>3</sub>C liquid using X-ray absorption image up to 10 GPa and effect of light elements on compressibility of liquid iron. *Journal of Geophysical Research: Solid Earth* 115, B06207.
- Terasaki, H., Suzuki, A., Ohtani, E., Nishida, K., Sakamaki, T., Funakoshi, K., 2006. Effect of pressure on the viscosity of Fe-S and Fe-C liquids up to 16 GPa. *Geophysical Research Letters* 33, L22307.
- Thompson, E., Davis, A., Bi, W., Zhao, J., Alp, E., Zhang, D., Greenberg, E., Prakapenka, V., Campbell, A., 2018. High-Pressure Geophysical Properties of Fcc Phase FeH<sub>x</sub>. *Geochemistry, Geophysics, Geosystems* 19, 305-314.
- Walker, D., 1991. Lubrication, gasketing, and precision in multianvil experiments. *American Mineralogist* 76, 1092-1100.

- Wasson, J.T., 2012. Meteorites: Classification and properties. Springer Science & Business Media.
- Weber, R.C., Lin, P.-Y., Garnero, E.J., Williams, Q., Lognonné, P., 2011a. Seismic detection of the lunar core. *Science* 331, 309-312.
- Wenk, H., Takeshita, T., Jeanloz, R., Johnson, G., 1988. Development of texture and elastic anisotropy during deformation of hcp metals. *Geophysical Research Letters* 15, 76-79.
- Wood, B.J., 1993. Carbon in the core. *Earth and Planetary Science Letters* 117, 593-607.
- Wood, B.J., Li, J., Shahar, A., 2013. Carbon in the core: its influence on the properties of core and mantle. *Rev Mineral Geochem* 75, 231-250.
- Yamazaki, D., Ito, E., Yoshino, T., Tsujino, N., Yoneda, A., Guo, X., Xu, F., Higo, Y., Funakoshi, K., 2014. Over 1 Mbar generation in the Kawai-type multianvil apparatus and its application to compression of (Mg<sub>0.92</sub>Fe<sub>0.08</sub>) SiO<sub>3</sub> perovskite and stishovite. *Physics of the Earth and Planetary Interiors* 228, 262-267.
- Zhang, D., Jackson, J.M., Zhao, J., Sturhahn, W., Alp, E.E., Hu, M.Y., Toellner, T.S., Murphy, C.A., Prakapenka, V.B., 2016. Temperature of Earth's core constrained from melting of Fe and Fe<sub>0.9</sub>Ni<sub>0.1</sub> at high pressures. *Earth and Planetary Science Letters* 447, 72-83.
- Zhu, F., Li, J., Liu, J., Lai, X., Chen, B., Meng, Y., 2018. Kinetic control on the depth distribution of superdeep diamonds. *Geophysical Research Letters* 46, 1984-1992.